THEORETICAL STUDY OF OXYGEN REDUCTION REACTION CATALYTIC PROPERTIES OF DEFECTIVE GRAPHENE IN FUEL CELLS

A Dissertation

Presented to

The Graduate Facaulty of The University of Akron

In Partial Fulfillment

of the Requirement for the Degree

Doctor of Philosophy

Lipeng Zhang

August, 2013

THEORETICAL STUDY OF OXYGEN REDUCTION REACTION CATALYTIC PROPERTIES OF DEFECTIVE GRAPHENE IN FUEL CELLS

Lipeng Zhang

Dissertation

Approved	Accepted
Advisor Dr.Zhenhai Xia	Department Chair Dr.Celal Batur
Co-advisor Dr.Xiaosheng Gao	Dean of the College George Dr.George K.Haritos
Committee Member Dr.Gregory Morscher	Dean of the Graduate School Dr.George R. Newkome
Committee Member Dr.Jie Zheng	Date
Committee Member Dr.David Perry	

ABSTRACT

In this dissertation density functional theory (DFT) was applied to study the electronic structure and catalytic properties of graphene containing different types of defects. These defects includes hetero-atoms such as nitrogen, sulfur doped graphene, point defects such as Stone-Wales defects, single vacancy, double vacancies and substituting pentagon ring at zigzag edge, line defects such as pentagon-heptagon carbon ring chains, pentagon-pentagon-octagon carbon ring chains locating at the middle of graphene. The mechanisms of oxygen reduction reaction (ORR) were studied on these defective graphene, and electron transfer processes were simulated. Using DFT methods, we also explored the effect of strains to ORR electronic catalytic properties on pure and nitrogen doped graphene.

Our simulaltion results show that nitrogen, sulfur doped graphene, graphene containing point defects, substituting pentagon ring at zigzag edge, graphene containing line defects, pentagon-heptagon chain or pentagon-pentagon-octagon chains which have odd number of heptagon or octagon carbon ring perform high catalytic properties for ORR. Four electron transfer reactions could occur, and there are also two electrons transfer occuring on these defective graphene. The Stone-Wales defect itself cannot generate the catalytic activity on the graphene, but can facilitate the formation of hetero atom doping on graphene, which could show high catalytic activities to ORR. The catalytic active sites on defective graphene are atoms possessing high spin or charge density, where the spin density plays more important effect on the catalytic properties. For the N-doped graphene, the identified active sites are closely related to doping cluster size and dopant-defect interactions. Generally speaking, a large doping cluster size (number of N atoms >2) reduces the number of catalytic active sites per N atom. In combination with N clustering, Stone-Wales defects can strongly promote ORR. For four-electron transfer, the effective reversible potential ranges from 1.04 to 1.15 V/SHE, depending on the defects and cluster size. The catalytic properties of graphene could be optimized by introducing small N clusters in combination with material defects. For S-doped graphene, sulfur atoms could be adsorbed on the graphene surface, substitute carbon atoms at the graphene edges in the form of sulfur/sulfur oxide, or connect two graphene sheets by forming a sulfur cluster ring. Catalytic active sites distribute at the zigzag edge or the neighboring carbon atoms of doped sulfur oxide atoms, which possess large spin or charge density. For those being the active catalytic sites, sulfur atoms with the highest charge density take two-electron transfer pathway while the carbon atoms with high spin or charge density follow four-electron transfer pathway. Stone-Wales defects not only promote the formation of sulfur-doped graphenes, but also facilitate the catalytic activity of these graphenes. The ORR catalytic capabilities of the graphene containing point or line defects denpend on whether the defects could introduce spin density into the system or not. The axial strain field applied on the graphene could change its electronic properties. Neither the compressive nor the tensile strain along the zigzag or armchair direction could facinitate the catalytic activities of perfect graphene without any

defects. Tensile strain along zigzag direction could change the electronic properties of nitrogen doped graphene, which are favorable to its ORR catalytic property.

Our simulation results explored the ORR on defective graphene in essence and provide the theoretical base for searching and fabricating new high efficient catalysts using the carbon based materials for fuel cells.

ACKNOWLEDGEMENTS

April is always the lovely season, not just because of the coming spring but also because I am almost there at this moment. Experiencing forty-four months in University of Akron, I almost finish my Ph. D program. There are a lot of things worthy memory, novel, bitter or sweet, whatever they are all my precious fortunes. The most important thing is that I knew a lot of people and made some good friends, they are giving me a lot of supports and help. Here I would like to give my sincerely appreciation to them.

First I should thank my advisor Dr. Zhenhai Xia. Through the beginning of my application for this position to arriving at University of Akron, choosing my program, doing the proposal until finishing my dissertation, he has been poured a lot of works along all my journeys. His perspectiveness and sharp intuition in academic not only make my work novelty, but also make me feel that it is interesting and accessible. I always know where I should go with his guide. I am benefited not just from his academic capability which extending to his great personalities. His hard working, tolerance and understanding always make my work easier and more important is that he has been setting a great example for us. Even though he transferred to Texas since 2011, he always takes care of everything going well for me as he still here. In addition to, he offered a lot of opportunities to improve myself. I appreciate all of these from him.

I am very grateful to Dr. Xiaosheng Gao. Since Dr. Xia left to Texas, he is my co-advisor. He takes care of my business in University of Akron. I feel lucky and pride under his supervisal. He is a so nice and considerate person I know, during prepareation of my proposal and defense processes, he gave me a lot of help and pertinent suggestion. I give my thanks to him.

Here I should give my special gratitude to Dr. David Perry. His profound knowledge, generous help and genial manner impressed me very much. I cannot remember how many times I ask help from him and give him troubles about the technical problems of my research work. He always satisfied me with great patience and gentle manner. I still remember one time, he led me to mechanical engineering library and showed me how to search and check spectrum personally. He make me not just feel the power of knowledge but also the charm of personality.

I should also give my thanks to Dr. Gregory N Morscher and Dr. Jie Zheng to being my committee member. Thanks for their precious time spent on my proposal, dissertation review and defence.

Our collaborators Dr. Liming Dai and Dr. Jong-Beom Baek gave us a lot of inspiration and help during my research work. We have a wonderful cooperation. I am very grateful to them.

Thanks to my group members Shihao Hu, Quan Xu, Zhijun Ma, Jianbing Niu, Thanyawalai Sujidkul, Jie Wen, and Lili Li they not only give me lots of help in study and life making them easier but also teach me a lot. Specially, I am thankful to my friend

Yanfeng Lu, Guang Ji, Kamil Nizamiev and Tatyanna Kotjak. They give me many touching moments in my life.

Of course, I should thank to my family, my parents, sister, brother-in-law. They always stand behind me, support me. They are the love in my heart forever.

TABLE OF CONTENTS

Page

LIST OF FIGURES xiii

LIST OF TABLES xviii

CHAPTER

I. INTRODUCTION 1

- 1.1 Background 1
- 1.2 Objective and significance 2
- 1.3 Dissertation outline 5

II. LITERATURE REVIEW 7

- 2.1 Graphene structure and fabrication methods 7
- 2.2 Electronic structure characteristics of graphene 9
- 2.3 Structural defects in graphene 11
- 2.4 Heteroatom doped graphene 18
  - 2.4.1 Nitrogen doped graphene 19
  - 2.4.2 Boron doped graphene 28
  - 2.4.3 Boron-nitrogen co-doped graphene as efficient catalyst of fuel cells 33

2.4.4 Sulfur doped graphene 34

2.4.5 Halogen element doped graphene 39

2.5 Summary and Outlook 42

III. SIMULATION METHOD 44

3.1 Schrödinger equation 44

3.2 Solution methods of Schrödinger equation 47

3.2.1 Born-Oppenheimer Approximation 47

3.2.2 Hartree-Fock method 47

3.2.3 Density functional theory method 50

3.3 Gaussian package and calculation method 52

3.3.1 Gaussian package 52

3.3.2 Calculation method and basis set 53

IV. OXYGEN REDUCTION REACTION MECHANISMS ON HETERO-ATOM DOPED GRAPHENE AS CATALYST OF FUEL CELL 55

4.1 ORR mechanisms on nitrogen doped graphene as catalyst of fuel cells 56

4.1.1 Models and method 56

4.1.2 Results and discussion 60

4.2 Effect of microstructure of nitrogen-doped graphene on oxygen reduction acticity 74

4.2.1 Methods 75

4.2.2 Results and discussion 79

4.3 Sulfur-doped graphene as efficient oxygen reduction reaction catalysts for fuel cells 98

4.3.1 Mehods 99

4.3.2 Results and discussion 103

4.4 Conclusions 116

V. ROLE OF POINT AND LINE DEFECTS IN CATALYTIC PROPERTY OF GRAPHENE FOR FUEL CELLS 119

5.1 Models and methods 119

5.2 Results and discussion 122

5.2.1 Spin and charge distribution on graphene containing defects 122

5.2.2 ORR paths on defective graphene 127

5.3 Conclusions 136

VI. STRAIN EFFECT ON ORR CATALYTIC PROPERTY OF GRAPHENE IN FUEL CELLS 138

6.1 Introduction 138

6.2 Models and method 140

6.3 Results and discussion 142

6.3.1 HOMO-LUMO energy gap and HOMO energy level 142

6.3.2 Spin and Charge density 145

6.4 Conclustions 148

VII. CONLUSIONS AND FUTURE WORK 149

7.1 Conclusions 149

7.1.1 ORR catalytic properties of doped graphene in fuel cells 149

7.1.2 Role of point and line defects on graphene for ORR catalytic properties in fuel cells 150

7.1.3 Role of strains applied on graphene in ORR catalytic properties in fuel cells 151

7.2 Recommended future works 152

REFERENCES 153

PUBLICATIONS 167

HONOURS AND AWARDS 169

LIST OF FIGURES

Figure Page

2-1 Graphene: the parent of all graphitic forms [5] 8

2-2 a) Graphene lattice. a_1 and a_2 are the unit vectors. b) Reciprocal lattice of graphene. The shaded hexagon is the first Brillouin zone, b1 and b2 are reciprocal lattice vectors [42] 11

2-3 Experimental TEM images and atomic structures obtained from DFT of point defects on graphene. (a) Experimental TEM image of the SW-5577 defect[50] (b) its atomic structure as obtained from DFT calculations [64]; (c) Experimental TEM image of Single vacancy SV-59 [50], (d) its atomic structure obtained from our DFT calculations; (e) Experimental TEM images of Double vacancy DV-585 [50], (f) its atomic structures obtained from DFT calculations [64].. 12

2-4 (a) Arrangement of the carbon atoms around the line defect [80]; (b) Grain boundary defect structure consisting of pentagon-pairs and octagon in graphene grown on a Ni substrate [73]; (c) Two grains (bottom left, top right) relative rotation. An aperiodic line of defects stitches the two grains together; (d) The image from c with the pentagons (blue), heptagons (red) and distorted hexagons (green) of the grain boundary outlined [81].. 16

2-5 Dislocations in graphene [74]. (a-c) Atomic structures of (1,0) and (1,1) dislocations, and a (1,0) + (0,1) dislocation pair, respectively; (d, e) Atomic structures of the $\theta = 21.8°$ large-angle grain boundary and the $\theta = 32.2°$ symmetric large-angle grain boundaries; (f) buckling of the graphene layer due the presence of a (1,0) dislocation.. 17

2-6 TEM [91] and Raman analyses of the N-graphene films. (a) Low-magnifivation TEM image showing a few layers of the CVD-grown N-graphene film on a grid. Inset shows the corresponding electron diffraction pattern; (b-c) High magnification TEM images showing edges of the N-graphene film regions consisting of (b) 2, (c) 4 graphene layers; (d) The Raman spectra of the N-graphene films of different graphene layers [103]................... 20

2-7 XPS spectra of N-doped graphene and the high-resolution of (a) C1s and (b) N1s XPS spectra, (d) Schematic representation of the N-doped graphene [103] 23

2-8 (a) RRDE voltammograms for the ORR in air-saturated 0.1 M KOH; (b) Current density (j) - time (t) chromoamperometric responses; (c) Current-time chromoamperometric response of electrodes to CO; (d) Cyclic voltammograms of N-graphene before and after a continuous potentiodynamic swept [91]. 25

2-9 Oxygen reduction reaction paths in alkaline solution on nitrogen doped graphene [132]. 28

2-10 Raman spectra of Boron doped graphene and pristine graphene [136] 29

2-11 XPS of boron doped graphene [136]. 30

2-12 Boron doped graphene as efficient metal-free cathode of fuel cell [136] 32

2-13 Schematic illustration of S-graphene preparation and its catalytic property to ORR [147] 35

2-14 (a) Typical TEM image of sulfur doped graphene; (b) XPS of sulfur doped graphene; (c) Raman spectroscopy of sulfur doped graphene [151]; (d) High resolution C1s XPS spectra of GO and SG with C1 and C2; (e) High resolution S2p XPS spectra of SG. The peaks are fitted to three energy components centered at around 163.9, 165.1 and 168.5 eV,corresponding to Sp3/2 (S1), Sp1/2 (S2), and S-O (S3), respectively; (f) The content of sulfur species (S1,S2, and S3) in SG sheets [147] 37

2-15 (a) Cyclic voltammograms for graphene-900 and S-graphene-900; (b) Linear sweep voltammograms (LSV) curves for various S-doped graphenes [147] and a Pt/C catalyst on a glass carbon rotating disk electrode saturated in O_2 at a rotation rate of 1600 rpm; (c) Rotating ring disk electrode linear sweep voltammograms of S-doped graphenes [148] at a rotation rate of 1600 rpm. 38

2-16 (a) Raman spectra evolution for single-layer graphene reacted with chlorine under xenon lamp irradiation. (b), (c) High-resolution XPS spectra of Cl 2p and C 1s in the photochlorinated graphene [153]; (d-f) TEM images of in-plane regions for Graphene nanoribbon treated for 0, 1 min. and 3min. in Cl_2 plasma [152] 40

2-17 Chlorine on graphene surface with different states: Covalent-bonding, charge-trasfer complex, non-bonding[156] 42

4-1 Nitrogen-containing graphene and corresponding no nitrogen-containing graphene sheets of (a) $C_{45}NH_{20}$, and $C_{45}NH_{18}$, (c) $C_{46}H_{20}$, and (d) $C_{46}H_{18}$, the larger gray circles are carbon atoms, the larger blue circle is nitrogen atom, and the smaller light white circles are hydrogen atoms, all the atoms are numbered showing on circles. 58

4- I l ( ), ( ), ( ), (g), (’), (’), d (g’) d f l op m z o u u (b), (d), (f), ( ), (d’), (f’), d (’) of y m fo o p, o g o l y p of the graphene, with the larger gray circles for carbon atoms, the larger blue circles for nitrogen atoms, the larger red circles for oxygen atoms, and the smaller light gray circles for hydrogen atoms. 63

4-3 The relative energy of two different reaction pathways of the ORR on N-graphene ($C_{45}NH_{20}$). For the first step, the reference energy state is the total energy of optimized N-graphene ($C_{45}NH_{20}$) and OOH molecules, and for the other reaction steps, the reference energy states are the total energy of the product of previous reaction and $H^+ + e^-$ 67

4-4 (a), (c) Charge distribution, and (b), (d) spin density distribution on the N-graphene with pyridinic structure ($C_{45}NH_{20}$) and pyrrolic structure ($C_{45}NH_{18}$), respectively. The number on the circle is the number of atom. The fractions on the side of these atoms in (a), (c) are atomic charge value and spin density value on the atoms. The denominator is charge value and the numerator is spin density number. In (b), (d) spin density distributes on the electron density isovalue plane; the most negative value is red while the most positive value is blue. 73

4-5 Optimized structure of each electron transformation in oxygen reduction reaction: (a) Initial position of OOH from nitrogen doped graphene, (b) OOH adsorbs on the graphene, (c) O-O bond is broken, (d) One water molecule is generated, and (e) C-O bond is broken, the second water molecule is generated. Grey, blue, red and small white balls represent carbon, nitrogen, oxygen and hydrogen atoms, respectively. 81

4-6 (a) Atomic charge density and (b) Spin density distribution on the nitrogen-doped graphene with Stone-Wales defects. 85

4-7 The adsorption energy of OOH on graphene as a function of (a) Spin density for atomic charge e= -0.087 ~ +0.085, and e = +0.205 ~ +0.263, and (b) Atomic charge density for s= -0.036 ~ +0.0072. The adsorption energy is calculated from Reaction (4-23) in the absence of charge.
.... 88

4-8 The graphene structures with a number of dopants and defects. N= the number of nitrogen dopants. Grey, blue, and small white balls represent carbon, nitrogen, and hydrogen atoms, respectively. The structures in the first row contain no defects while the structures in the second row have. 91

4-9 The reversible potentials of ORR versus N cluster size for the graphene (a) without defects, and (b) with defects. Dot lines represent standard reversible potential (1.228 V). 93

4-10 Reaction scheme of ORR on N-graphene in acidic solution, where ❶ presents an intermediate OOH adsorption mechanism and ❷ a direst O_2 adsorption mechanism, and ① ~ ⑤ represents 5 reaction pathways after OOH adsorption. 93

4-11 HOMO-LUMO energy gap as a function of the number of nitrogen doped atoms in cluster with and without Stone-Wales defects. 97

4-12 Several possible sulfur-doped graphene structures: (a) Sulfur atoms adsorbed on the surface of the graphene; Substituting sulfur atoms at (b) zigzag and (c) armchair edges; SO_2 substituted at (d) zigzag and (e) armchair edges and (f) sulfur ring cluster connecting two pieces of graphene. The structures of the graphene are shown only partially to highlight the doping structures. Small white, grey, yellow, and red balls represent hydrogen, carbon, sulfur, and oxygen atoms, respectively. 102

4-13 Atomic charge density and spin density distributions on the S-doped graphene. Atomic charge density distribution on S-adsorbed graphenes with (a) perfect structure and (b) one Stone-Wales defect; (c) Atomic charge density, and (d) spin density distributions on substituting S at zigzag edge of perfect graphene; (e) Atomic charge density, and (f) spin density on SO_2-doped graphene with a Stone-Wales defect; (g) Atomic charge density on sulfur ring cluster connecting two pieces of graphenes. The colors of the balls stand for relative values of charge and spin density. The density decreases linearly from positive to negative values in the color order of red, orange, yellow, green and blue. Sulfur and oxygen atoms are labeled with S and O, respectively. The unlabeled small and large balls represent H and C, respectively. 107

4-14 ORR process on the sulfur doped graphene when the catalytic active site is sulfur atom: (a) two OOH molecules adsorbed on the sulfur atom, and (b) two H_2O_2 molecules formed and departed from the sulfur atom after the introduction of two more H atoms............ 108

4-15 ORR processes on the sulfur-doped graphene where a carbon atom at the zigzag edge acts as the catalytic active site because of the highest spin density on it: (a) OOH adsorbed on the carbon atom, (b) rupture of O-O bond and formation of water molecule after an H atom was introduced into the system, (c) formation of an OH after the second H was introduced, and (d) formation of another water molecule after third H was introduced into the system. 110

4-16 HOMO and LUMO distribution on graphene and sulfur doped graphene (GN) 116

5-1 Perfect and defective graphenes. (a) Perfect graphene, (b) Stone-Wales defect (SW), (c) Single vacancy (SV), (d) Double vacancies (DV), (e) Edge defect with pentagon ring at zigzag edge (PZ), Octagon and fused pentagon carbon rings line defect with (f) odd number of octagon rings (GLD-558-01) and (g) even number of octagon rings (GLD-558-02), and Pentagon-heptagon pairs line defects with (h) even number of heptagon ring (GLD-57-01) and (i) odd number of heptagon ring (GLD-57-02). 122

5-2 Charge and spin density distribution on perfect graphene and defective graphenes. (a), (b), (d), (f) and (h) are charge density distribution on perfect, SV, PZ, GLD-558-01 and GLD-57-02 graphenes, respectively. While (c), (e) and (g) show spin density distribution on PZ, GLD-558-01 and GLD-57-02 graphenes, respectively. The color on the circle stands for different value, which is decrease in the color order red, orange, yellow, green, and blue. 127

5-3 ORR processes on graphene with pentagon carbon ring at zigzag edge: (a) OOH adsorbed on carbon atom, (b) O-O bond breakage, and a water molecule formed, (c) OH molecule formed, and (d) two water molecules departing from graphene surface..................... 130

5-4 Two electron transfer processes of ORR on graphene with pentagon-pentagon-octagon chains (GLD-558-01): (a) OOH adsorbed on carbon atom #65, and (b) H_2O_2 molecule formed and departing from the graphene surface... 130

5-5 HOMO and LUMO distribution on perfect graphene and the graphene with point and line defects: (a) HOMO and (b) LUMO of perfect graphene, (c) HOMO and (d) LUMO of PZ, (e) HOMO and (f) LUMO of GLD-558-01, (g) HOMO and (h) LUMO of GLD-57-02. 136

6-1 Graphene models and the way of applying strains: (a) graphene cluster $C_{100}H_{26}$, (b) nitrogen doped graphene $C_{99}NH_{26}$, (c) compress strain along armchair direction (CA-strain), (d) tesile strain along armchair direction (TA-strain), (e) compress strain along zigzag direction (CZ-strain), (f) tensile strain along zigzag direction (TZ-strain). 141

6-2 HOMO-LUMO energy gap correspond to strains along uniaxial zigzag and armchair direction on (a) $C_{100}H_{26}$, and (b) $C_{99}NH_{26}$; HOMO energy level versus strains along uniaxial zigzag and armchair directions on (c) $C_{100}H_{26}$, and (d) $C_{99}NH_{26}$........ 145

6-3 Maximum values of charge and spin densities on $C_{99}NH_{26}$ correspond to strains applied and the percent of atoms with higher charge or spin density; (a) maximum charge density on $C_{99}NH_{26}$ versus strains, (b) maximum spin density on $C_{99}NH_{26}$ versus strains, and (c) percent of atom with spin density more than 0.150 and 0.100 on $C_{99}NH_{26}$ correspond to strains. 148

LIST OF TABLES

Table Page

2-1 Fabrication methods of nitrogen doped graphene and its applications in energy transfer and storage devices 19

3-1 R o f gy ΔG (V) of $O_2 + 2H_2 \rightarrow H_2O$ using different calculation methods and basis sets in standard states 54

4-1 Variation of distance between different atoms during each reaction step for two different reaction paths (Unit/Å) 63

4-2 HOMO, LUMO and HOMO-LUMO gy g p of α l o d β l o fo $C_{45}NH_{20}$, $C_{45}NH_{18}$, $C_{46}H_{20}$ and $C_{46}H_{20}$ (Unit/eV) 69

4-3 Adsorption energy difference and reversible potentials of each ORR step on the graphene with two doped nitrogen atoms and two Stone-Wales defects 83

4-4 The number of active sites and effective reversible potential for nitrogen-doped graphene. 96

4-5 Formation energy (eV) of S doped graphene 104

4-6 R o f gy ΔG (V) of o l o d fou l o f o processes on sulfur doped graphene with and without Stone-Wales defects 113

5-1 R o f gy ΔG (V) of fou d o l o transfer pathways of ORR on graphenes with point and line defects. 133

CHAPTER I

INTRODUCTION

1.1 Background

Fuel cell is a device that converts chemical energy from a fuel into electricity through a chemical reaction with oxygen or another oxidizing agent. Hydrogen is the most common fuel, and hydrocarbons such as natural gas and alcohols like methanol can also be used. Fuel cells are used for primary and backup power for commercial, industrial and residential buildings. They are used to power fuel cell vehicles, including automobiles, buses, airplanes, boats and submarines et al. There are many types of fuel cells, but they all consist of an anode (negative side), a cathode (positive side) and an electrolyte that allows charges to move between the two electrodes. Electrons are drawn from the anode to the cathode through an external circuit, producing direct current electricity. Due to the different electrolyte, fuel cells are classified into proton exchange membrane fuel cells (PEMFC), solid oxide fuel cells (SOFC), and molten carbonate fuel cells (MCFC) et al. The first one is usually used in lower temperature environment (-35-40 ˚C), d l o g mp u (600-1 00 ˚C) fuel cells. Fuel cells powered by hydrogen from secure and renewable sources are the ideal solution for non-polluting devices. It has several advantages as follows: high efficiency conversion. Fuel cells convert chemical energy directly into electricity without the combustion process. The energy efficiency of a fuel cell is generally between 40-60%, or 85% if waste heat is capture for use. The second advantage is high power density, which allows fuel cells to be relatively compact source of electric power. The third advantage is quiet operation. Due to their nature of operation, fuel cells are extremely quiet in operation. This allows fuel cells to be used in residential or build-up areas where the noise pollution is undesirable. However, the most disadvantage of fuel cell is high cost. Fuel cell must meet three criteria: cost, performance and durability. The cathode oxygen reduction reaction (ORR) is six or more orders of magnitude slower than the anode hydrogen oxidation reaction and thus limits performance, so many of research and development focuses on improving the cathode catalysts and electrode. Most of the catalysts used today are based on Pt, with high price of this scarce precious metal having a decisive impact on costs. It is a long work for researchers to reduce the cost of the catalyst and meantime make sure the catalyst with high property. There are several method used to decrease the cost of the electrode catalyst. These methods include extending surface area of catalysts, discreting low-aspect-ratio nanoparticles dispersed on low or high-aspect-ratio supports, using unsupported nanoparticles and exploring new Pt-free electrocatalysts. The last one catches more attention of scientists and engineers. Explored carbon based materials are one of the efficient electrocatalysts for fuel cells.

1.2 Objective and significance

Gong et al. [1] synthesized a vertically aligned nitrogen containing carbon nanotubes (VA-NCNTs) in 2009, which act as a metal free electrode with a much better electrocatalytic activity, long-term operation stability, and tolerance to crossover effect than platinum for oxygen reduction reaction (ORR) in alkaline environment. Qu et al. [2] synthesized nitrogen doped graphene (NG) in 2010, which also shows high electrocatalytic activitiesproperty for ORR. These new discoveries opened a new page for nano-carbon based materials as electrocatalyst for fuel cell. Targeted catalyst development benefits from a detailed understanding of the electrochemical reduction of oxygen to water, $O_2 + 4H^+ + 4e^- \rightarrow H_2O$, which is mechanistically complicated. It is usually thought to involve different reaction pathways such as direct 4e$^-$ reduction of oxygen to water; or a 2e$^-$ reduction to H_2O_2. The kinetic current density i reflects the l y ' v y, o m l z d by u f of l od d g d potential E, given to be a function of the Gibbs ene gy of d o p o ΔG_{ad} [3, 4]

$$i = nFKc_{O_2}(1 - \quad_{\mathrm{ad}})^x \exp\left(-\frac{\beta FE}{RT}\right)\exp\left(-\frac{\gamma \Delta G_{ad}}{RT}\right) \tag{1-1}$$

Where n, F, K, x, β, γ d R o , c_{O2} oxyg o o , $_{\mathrm{ad}}$ the fraction of electrode surface sites covered with adsorbates. This suggests that anything done to the atomic or electronic structure of electrode surface that delays hydroxyls adsorbing and blocking O_2 adsorption sites will have a positive impact on the kinetic current density. Since now, we know finding the O_2 adsorption sites, we call them catalytic active sites, and determining adsorption energy or adsorption Gibbs free energy variation are important to improve the electrocatalytic property of the electrodes for fuel cells. Although the VA-NCNTs and NG show high catalytic property to ORR, its mechanisms on these electrodes are not clear, and how the catalytic property going for other similar metal free carbon based nano materials is also worth to study. So the present work dealt with the following objectives:

Firstly, theoretically study the ORR mechanism on hetero-atom doped graphene. Hetero atoms include nitrogen, sulfur. Based on experimental results, different hetero-atom doped graphene models were built. The electron transmission processes were simulated on these doped graphene, and also the effect of hetero atom bonding structures to catalytic property was analyzed. The catalytic property of electrode directly relate to its electronic property, so the charge density, spin density, molecular orbital and energy gap were studied on these doped graphene.

The second projective is to study the effect of defects and strain field on the ORR catalytic property of graphene. These defects include point defect like Stone-Wales defects, vacancies and line defect like pentagon-pentagon-octagon (558) and pentagon-heptagon (57) pair chains on graphene. Strains were applied as axial stretch and compression along zigzag or armchair directions on the graphene. Similarly the ORR catalytic property and electronic structures were calculated for the graphene.

The study of ORR mechanisms on the graphene supported the experimental conclusions and showed the electron transmission process during the ORR. It revealed the reason why these new metal-free electrodes showhigh catalytic property. The most important is based on these theoretical results the fabrication methods of these doped graphene could be further improved and optimized to get more efficient catalyst electrodes for fuel cells. It offers the basic principle to design new efficient metal-free catalyst or search for new catalyst for fuel cells.

1.3 Dissertation outline

This dissertation is divided into seven chapters. Chapter II provides a comprehensive literature review regarding the theoretical study of the electronic property of hetero-atom doped graphene. And also the ORR mechanisms on doped graphene in theory are summarized.

Chapter III introduces the theoretical principle of simulation used in our project. For our simulate calculation, we compared several different basis set methods, and confirmed the basis set we applied in our calculation show higher accurate and reliability.

Chapter IV deliberates the mechanism of ORR on hetero-atom (nitrogen, sulfur) doped graphene. And also the electronic properties of these doped graphene are explored. The catalytic property of electrode relates to the catalytic active sites and their quantity, position and distribution on the electrode surface. The effects of doped graphene structure on the ORR catalytic property are discussed. We obtain the characters of active sites and their distribution. The electron transformation processes are revealed. The electronic property, such as charge, spin density distribution, characteristic molecular orbital and energy gap are explored using simulation method on these doped graphene.

Chapter V presents the effect of defects (include point and line defects) on the ORR catalytic properties on the graphene. The zero dimentional defects include Stone-Wales and single vacancy, double vacancy, substituting pentagon carbon ring at zigzag edge. The one dimentional defects include 588 and 57 carbon ring chains which separate graphene into different crystal domains. The catalytic property and electronic property of these graphene containing defects are elaborated.

Chapter VI explores the effect of strain field on the graphene for the electrocatalytic property of ORR. Axial stretch and compress strain are applied gradually along the zigzag and armchair direction on the graphene. Catalytic and electronic properties of these graphenes with strain are studied.

Chapter VII summarizes the findings in this present dissertation, and the future works are recommended.

CHAPTER II

LITERATURE REVIEW

2.1 Graphene structure and fabrication methods

Graphene is a two dimentional (2D) atomic crystal which consists of carbon atoms arranged in a hexagonal lattice. It is basic building block for graphitic materials of all other dimentionalities [5] (Figure 1-1). It can be wrapped up into 0 D fullerenes, rolled into 1 D nanotubes or stacked into 3D graphite. It is distinctly different from fullerenes, carbon naotubes (CNT), and typically important properties of graphene are the thinnest object ever obtained, o ld' o g m ls [6], quantum Hall effect at room temperature with massless Dirac fermions charge carriers [7-9], tunable band gap [10], extremely electrically [11], thermally [12] and high elasticity [6] et al. Owing to its superb properties, large surface area, which is available for chemical modification [13, 14]. Graphene is promising for applications ranging from electronics like sensors, solar cells, field-emission devices, filed-effect transistors, supercapacitors, and batteries [15-23] to composite materials [24-25]. Ideally graphene is a single-layer material, but graphene samples with two or more layers are being investigated with equal interest. Three different types of graphenes can be defined: single-layer (SG), bilayer graphene (BG), and few-layer graphene (FG, umb of l y ≤1 0). Al oug gl -layer graphene and bilayer graphene were first obtained by called “Scotch tape method” [6,], several strategies have been developed for the synthesis of graphenes [28].

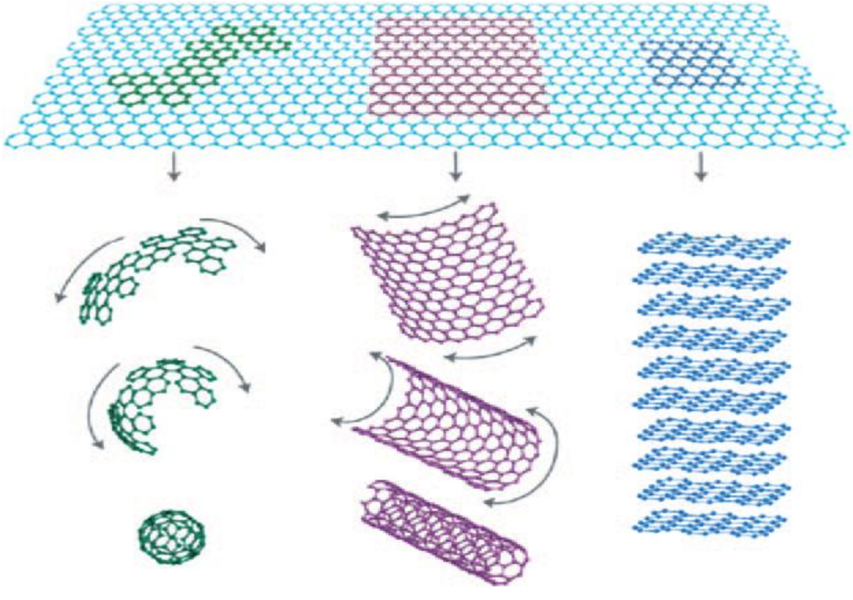

Figure 2-1 Graphene: the parent of all graphitic forms (from reference [5]).

Apart from the “Scotch tape method”, there are four other approaches to fabricating graphene. Thermal approaches grow graphene. Epitaxial growth of graphene on silicon carbide (SiC) has been reported by heating SiC to high temperatures (>1000˚C) to reduce it into graphene [29]. Another method of obtaining graphene is by CVD of hydrocarbons on a metal or metal-coated substrate [30, 31]. High quality sheets of few layer graphene have been synthesized via CVD on Ni films [2, 32, 33]. By replacing the Ni substrate with a Cu foil, with different pressure, a single layer and multilayer graphenes were formed [32-35]. Recently, CVD methods have also been used to turn sucrose quickly and easily into graphene onto a Cu or Ni substrate [36]. The third pp o of “m k g” g p m y. More recently, a gram quantity of graphene was produced through the reduction of ethanol by sodium metal, followed by pyrolysis of the ethoxide product and washing with water to remove sodium salts. Large-scale production of graphene sheets has also been achieved by exfoliation of graphite via acid oxidation into dispersible graphite oxide (GO), followed by reduction of GO and annealing in argon/hydrogen to yield graphene sheets [37, 38]. The final method to fabrication graphene is chemical synthesis, a process in which precursor compounds are combined by organic reactions to form molecular fragments of graphene. Full details of the typical reactions used can be found there [39-41]. Each of the four classes of graphene production methods has its limitations, and none have yet reached the point needed for commercial manufacture of graphene. It is apparent that variety of different forms of graphene-like materials can be produced by these different methods.

2.2 Electronic structure characteristics of graphene

What really make graphene special are its electronic properties. The graphene honeycomb lattice is composed of two equivalent carbon sublattices A and B, shown in Figure 2-2 a) [42]. Figure 2-2 b) shows the first Brillouin zone of graphene, with the high symmetry points M, K, K', d Γ m rked. Note that K and K' are the two inequivalent points in Brillouin zone. The s, p_x and p_y o b l of bo om fo m σ bo d g bo g bo om . T π l o p_z orbital, one from each carbon, form the bonding π d bo d g π* b d of g p . T d p o l o of π electrons is described by the tight-binding model incorporating only the first nearest g bo o . T π d π^* b d ouch at the K and K' points. The electronic states near the K-point are composed of states belonging to different sublattices A and B; And their relative contributions is taken into account using two component wave functions (spinors). The wave functions at K and K' are related by time-reversal symmetry, and also valence and conduction bands touching at two points (K and K') of the Brillouine zone [43-45]. T o q u of x go l ymm y of g p ’ lattice (which is not one of the Bravais lattices): it has two atoms per unit cell and can be co p u l z d o p g gul l . T π d π^* b d o K and K' points guarantees a gapless spectrum with linear dispersion relation. Thus, the absence of a gap between the valence and the conduction bands in graphene makes for a very robust phenomenon and is a consequence of the symmetry between the sublattices [45]. (In boron nitride, where they symmetry between the sublattices is broken, a large gap is opened in the electronic spectrum [46]). The linear dispersion relation already makes graphene special, but there is more to it than that. States in the valence spinor wave function, so electrons and holes are linked via charged conjugation. This link implies that quasiparticles in graphene obey chiral symmetry, similar to that which exists between particles and antiparticles in quantum electrodynamics (QED). This analogy between relativistic particles and quasiparticles in graphene is extremely useful and often leads to interesting interpretations of many phenomena observed in experiment [47].

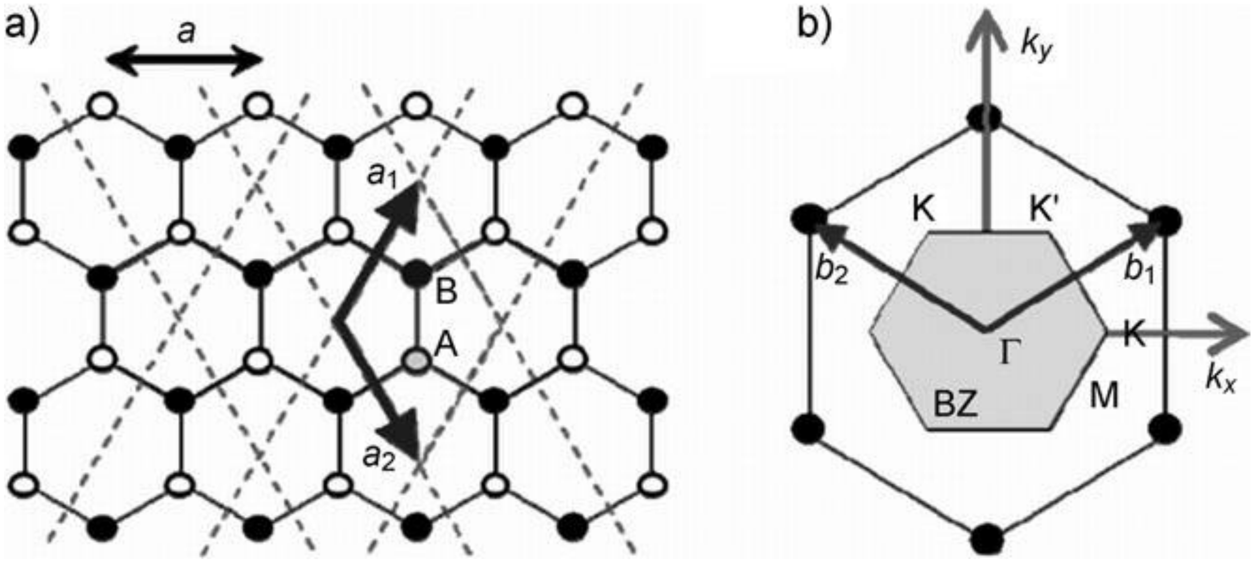

Figure 2-2 a) Graphene lattice: a_1 and a_2 are the unit vectors. b) Reciprocal lattice of graphene. The shaded hexagon is the first Brillouin zone, b1 and b2 are reciprocal lattice vectors (from reference [42]).

2.3 Structural defects in graphene

Structural defects may appear during graphene growth or fabrication process. They exist in graphene and can dramatically alter its properties. Defects can also be deliberately introduced into this material, for example, by irradiation or chemical treatments. Several experimental studies have shown the occurrence of either native or physically introduced defects in graphene. Transmission electron microscopy (TEM) [48-52] and scanning tunneling microscopy (STM) [53, 54] have been used to obtain images of defective graphene with atomic resolution. The interpretation of the experimental results was simplified by the fact that the theory of defects in graphene had already been developed to some extent in the context of carbon nanotubes [55-59] and graphite [60-62].

There are two types defect in graphene. One is point defects, typically vacancies or interstitial atoms, are zero-dimentional. Foreign atoms may exist as zero-dimentional defects when they substitute individual atoms of the crystal or are located on interstitial sites. Another is line defect, here it plays a different role comparing with that in three dimentional materials. The simplest point defect is the Stone-Wales (SW) defect [63], which does not involve any removed or added atoms. Four hexagons are transformed into two pentagon and two heptagons (SW-5577 defect) by rotating one of the C-C bonds by 90˚, o f gu -3 [64]. Formation energy of it is $E_f \approx 5$ V [65, 66].

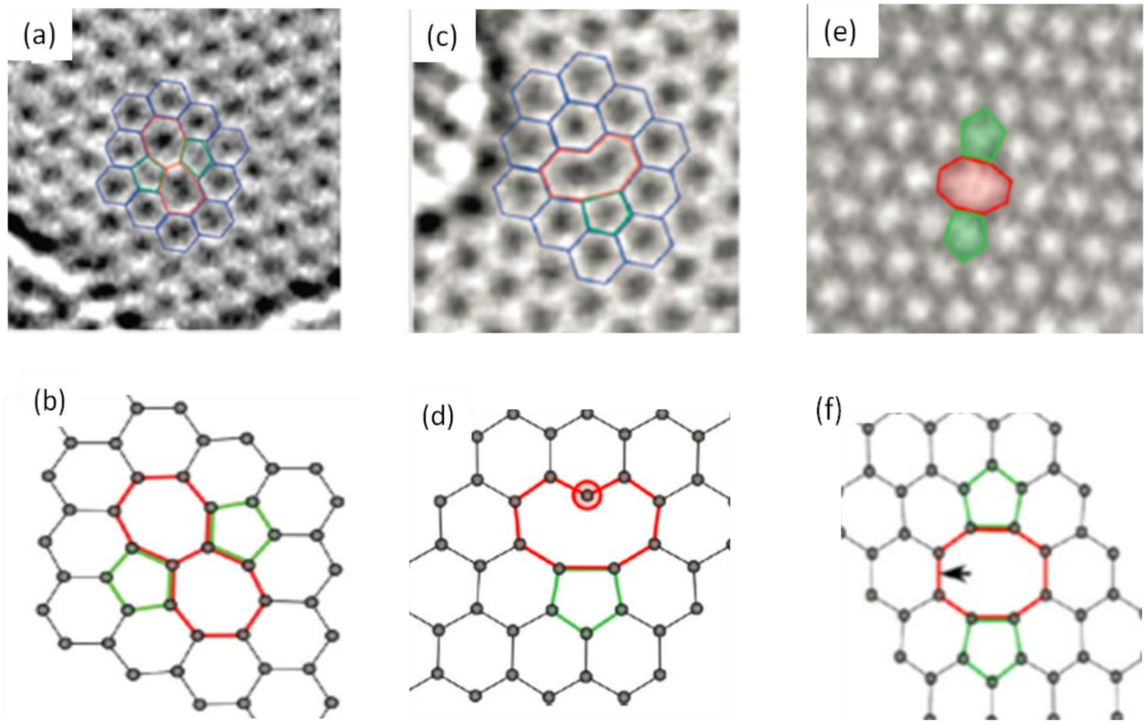

Figure 2-3 Experimental TEM images and atomic structures obtained from DFT of point defects on graphene. (a) Experimental TEM image of the SW-5577 defect(from reference [50]) (b) its atomic structure as obtained from DFT calculations (from reference [64]); (c) Experimental TEM image of Single vacancy SV-59 (from referece [50]), (d) its atomic structure obtained from our DFT calculations; (e) Experimental TEM images of Double vacancy DV-585 (from reference [50]), (f) its atomic structures obtained from DFT calculations (from reference [64]).

Another simple point defect on graphene is single vacancy, shown in Figure 2-3 (c) and (d). Single vacancies (SV) in graphene have been experimentally observed by TEM [49, 50] and STM [53]. One dangling bond always remains owing to geometrical reasons in SV defect. This leads to the formation of a five-membered and a nine-membered ring (SV-59 defect). Calculations have given formation energy a value $E_f \approx$ 7.5 eV [58, 60].

Double vacancies (DV) can be created either by the coalescence of two SVs or by removing two neighboring atoms. As shown in figure 2-3 (e) and (f), no dangline bond is present in a fully reconstructed DV so that two pentagons and one octagon (DV-585 defect) appear instead of four hexagons in perfect graphene. Simulations [58, 60] indicate that the formation energy E_f of a DV is about 8 eV. As two atoms are missing, the energy per missing atom (4 eV per atom) is much lower than for a SV. Hence, DVs are thermodynamically favored over SVs. The DVs can transform to other defects [64] by re-arranging the carbon atom bonding structure.

Straining the local structure in two dimentions, additional atoms use the third dimension. The energetically favored position is the bridge configuration (on top of a carbon-carbon bond). When particular additional atom interacts with a perfect graphene layer, it changes the hybridization of the carbon atoms in the layer. Some degree of sp^3-hybridization can appear locally so that two new covalent bonds can be formed between the adatom and the underlying atoms in the graphene plane. In addition to the bridge position, other metastable configurations are possible [67]. The small energy difference of about 0.3 eV between the local and global minima indicates that adatoms migrate easily over the graphene surface. When two migrating adatoms meet each other and form a dimer, they can be incorporated into the network of sp^2-hybridized carbon atoms at the expense of local curvature of the network [68]. The effect of a foreign atom on the properties of graphene depends on the bonding between the atom and graphene [69]. If the bond is weak, only physisorption due to van der Waals interaction occurs. If the interaction is stronger, covalent bonding between the foreign atom and the nearest carbon atoms leads to chemisorption. Various bonding configurations, normally corresponding to high symmetry positions such as on top of a carbon atom, on top of the center of a hexagon, or the bridge position are possible. Foreign atoms can also be incorporated into graphene as substitutional impurities. Boron or nitrogen serves as the natural dopants in carbon structures since they have one electron less or more, respectively, but roughly the same atomic radius. Much larger atoms such as transition metal impurities have also received particular attention due to their ability to inject charge into the electron system of graphene [70]. Replacing carbon by boron or nitrogen atoms is of considerable interest because impurities not only move the position of the Fermi level but also change the electronic structure of graphene [71, 72]. As nitrogen doping has been shown to be an efficient way of introducing reactive sites into other carbon sp^2 structures and thus to functionalize these materials [73].

For line defects on graphene, they are also named one-dimentional defects. They have been observed in several experimental studies of graphene [48, 74-76]. These line defects are tilt boundaries separating two domains of different lattice orientations with the tilt axis normal to the plane. Such defects can be thought of as a line of reconstructed point defects with or without dangling bonds [77-79]. Some one-dimentional defects in graphene resemble the projection of a dislocation in a conventional crystal, as figure 2-4.

Line defects in graphene frequently separate domains of different crystal orientation. Several examples have been shown in the growth of graphene on metal surfaces [74, 76]. The arise because simultaneous nucleation of graphene at different points may lead to independent two-dimentional domains, corresponding to grains in three-dimensional crystals. Normally, metal surfaces are used to grow graphene by chemical vapor deposition. The misfit between metal and graphene may lead to differing lattice orientations for different grains. Therefore, a line defect appears when two graphene grains with differing orientations coalesce, as figure 2-5. The linear defect corresponding to grain boundaries in graphene should be of paramount important. It is well-known that the properties of polycrystalline materials are often dominated by the size of their grains and by the atomic structure of the grain boundaries, but the role of such structures should be pronounced in two-dimentional materials such as graphene where even a line defect can divide and disrupt a crystal. In particular, grain boundaries may govern the electronic transport in such samples [78].

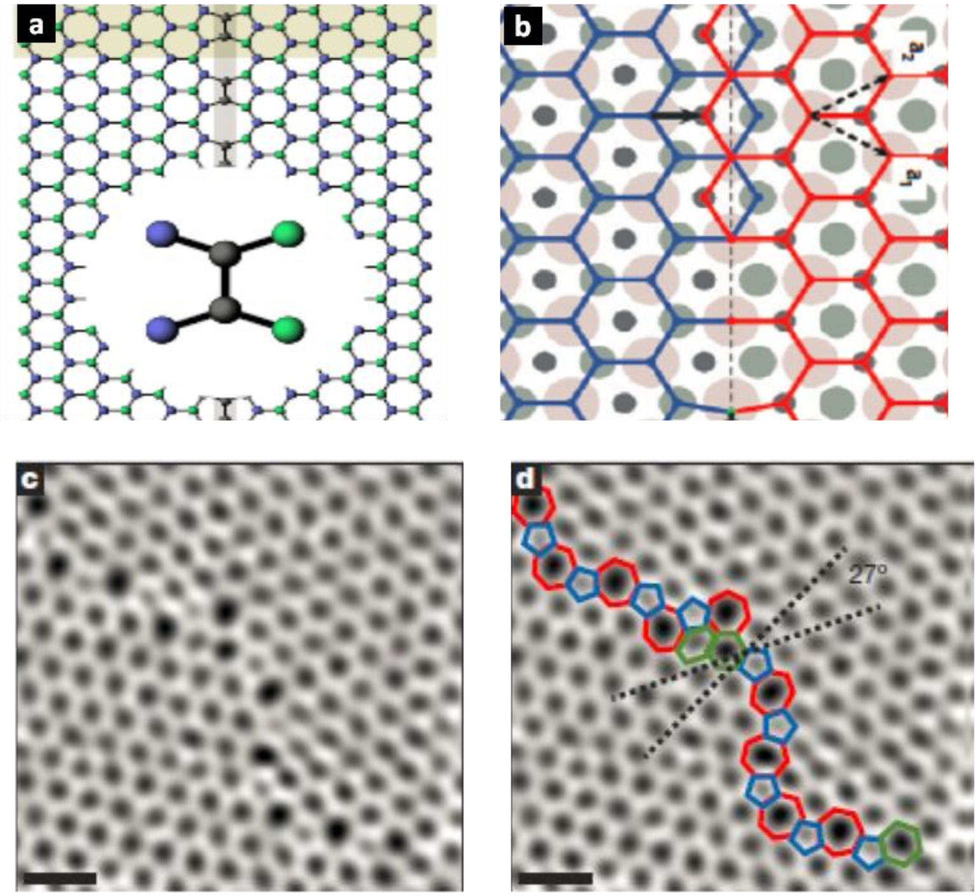

Figure 2-4 (a) Arrangement of the carbon atoms around the line defect (from reference [80]); (b) Grain boundary defect structure consisting of pentagon-pairs and octagon in graphene grown on a Ni substrate (from reference [73]) ( ) T o g (bo om l f , op g) relative rotation. An aperiodic line of defects stitches the two grains together; (d) The image from c with the pentagons (blue), heptagons (red) and distorted hexagons (green) of the grain boundary outlined (from reference [81]).

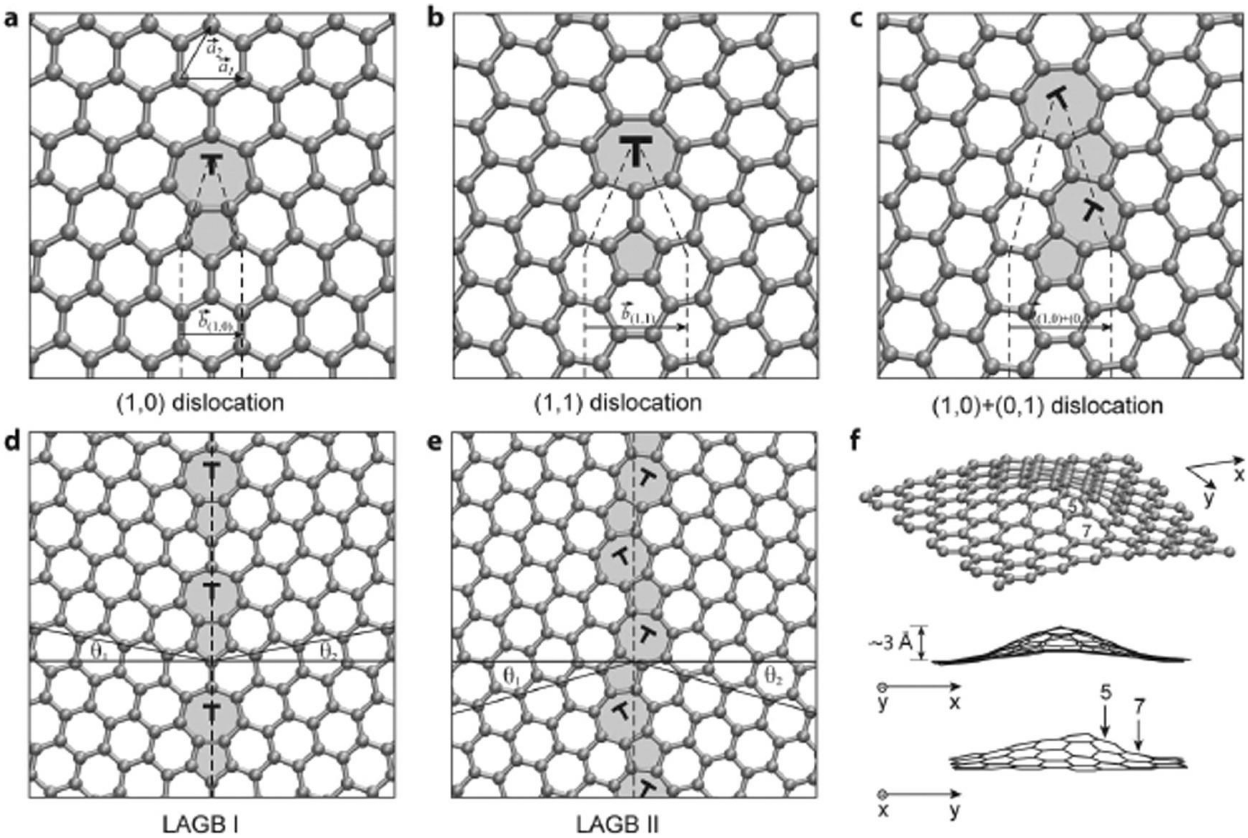

(1,0) dislocation

(1,1) dislocation

(1,0)+(0,1) dislocation

LAGB I

LAGB II

Figure 2-5 Dislocations in graphene (from reference [74]). (a-c) Atomic structures of (1,0) and (1,1) dislocations, and a (1,0) + (0,1) dislocation pair, respectively; (d, e) Atomic u u of θ = 1.8° l g - gl g bou d y d θ = 3 . ° ymm l g - angle grain boundaries; (f) buckling of the graphene layer due the presence of a (1,0) dislocation.

Each graphene layer is terminated by edges with the edge atom being either free or passivated with hydrogen atoms. The simplest edge structures are the armchair and the zigzag orientation. They can reconstruct to form any other direction in between these two. A simple example of an edge defect is the removal of one carbon atoms from a zigzag edge. This leads to one pentagon in the middle of a row of hexagons at the edge. Other edge reconstructions result in different combinations of pentagons and heptagons at the edge also can be obtained.

2.4 Heteroatom doped graphene

Doping constitutes is a powerful route to tailor the electronic properties of graphene. It is noteworthy by doping to alter the electronic and quantum transport properties. These modifications strongly depend on the type of dopants, concentrations and their location within the graphene. The doping of graphenes could be classified into two categories. One is electrical doping, such as gate-controlled doping [82, 83], metallic cluster-induced doping [84] or substrate-induced doping [85]. The other is chemical doping, occurring when changing the lattice structures of graphene via chemical routes, such as substitutional doping with heteroatoms [86], or molecular doping [87]. In this review we just focus on the chemical doping, especially on substitution or adsorption heteroatoms, such as Nitrogen [86], Boron [88], Sulfur [89], and Chlorine [90]. In particular, substitutional doping in graphene implies that carbon atoms in the hexagonal lattice are replaced by heteroatoms, thus resulting in the disruption of the sp^2 hybridization of the carbon atoms, changing of the equilibrium lattice parameters. Except for the substitutional doping of heteroatoms within the graphene lattice, the physical adsorption of atom or molecules on graphene surface could also induce significant changes in the electronic transport of sp^2 hybridized graphene. This surface adsorption can cause charge transfer between graphene and the adsorbed molecules, thus modifying the carrier density in graphene while retaining its high intrinsic mobility.

2.4.1 Nitrogen doped graphene

Nitrogen doped graphene has been fabricated by many different methods. They exhibit excellent properties in energy storage and transfer fields, like fuel cells, solar cells, Lithium ion batteries. The electronic properties of nitrogen doped graphene were studied by theoretical methods. The effect mechanisms of nitrogen-doped graphene on these fields were also explored. Here we mainly present theoretical study of ORR mechanisms on nitrogen doped graphene for fuel cells. Table 2-1 shown the nitrogen doped graphene synthesized by different methods and their application in energy transformation and storage fields, especially in fuel cells, solar cells and Lithium ion batteries.

Table 2-1 Fabrication methods of nitrogen doped graphene and its applications in energy transfer and storage devices

Fabrication method	Nitrogen content/at.%	Apllication
CVD	~4 (N/C)	Fuel Cell Cathode [91]
Detonation Reaction	12.5 (N/C)	Fuel Cell Cathode [92]
CVD	~16	Fuel Cell Cathode [93]
Mild Reaction	4.5-16.7	Fuel Cell Cathode [94]
Plasma Reaction	8.5	Fuel Cell Cathode [95]
Heatt-treatment	~2.8	Fuel Cell Cathode [96]
Hydrothermal Method	---	Dye-sensitized solar cells cathode [97]
Hydrothermal reaction	2.5	Dye-sensitized solar cells cathode [98]
Heating Reaction	2.8	Li-ion battery [99]
Heating Reaction	3.06	Li-ion battery anode [100]

CVD	~9	Li-ion battery [101]
Heat treatment	2	Li-ion battery[102]

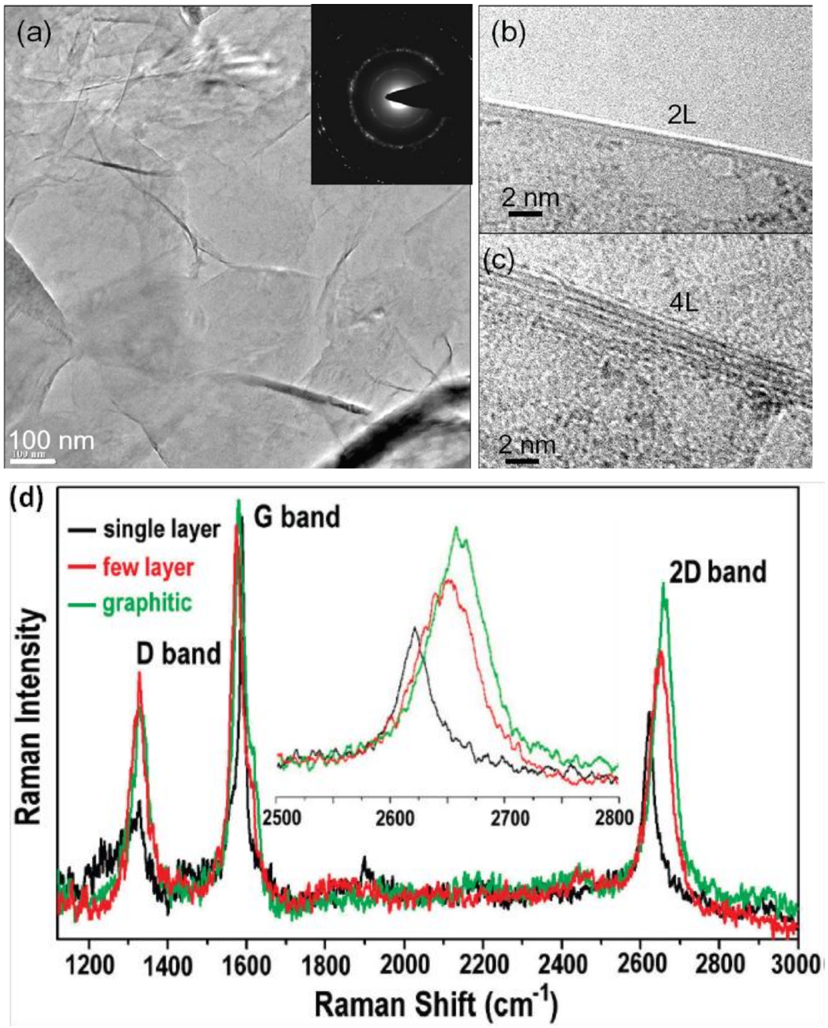

Figure 2-6 TEM (from reference [91]) and Raman analyses of the N-graphene films. (a) Low-magnifivation TEM image showing a few layers of the CVD-grown N-graphene film on a grid. Inset shows the corresponding electron diffraction pattern; (b-c) High magnification TEM images showing edges of the N-graphene film regions consisting of (b) 2, (c) 4 graphene layers; (d) The Raman spectra of the N-graphene films of different graphene layers (from reference [103]).

Figure 2-6 is TEM [91] and Raman spectrum analyses [103] of Nitrogen doped graphene. When nitrogen atoms substitute carbon atoms, there are three different bonding configurations within carbon lattice, including graphitic N, pyridinic N, and pyrrolic N. Graphitic N and pyridinic N are sp^2 hybridized. The former contributes one *p* electron to the π system. Pyrrolic N is sp^3 hybridized which contributes two *p* electrons to the π system. Apart from these three bonding structure, N oxides of pyridinic of N are also observed in N-graphen. Raman spectroscopy is a powerful tool for indentifying carbon materials. All of the Raman spectra have a high intensity of D band (1328 cm^{-1}), which indicates the doping of the graphitic sheets [104], as the D band only occurs in the sp^2 C with defects [105], and N doping introduces large amount of topological defects [106]. The G band is located at 1576-1582 cm^{-1}, while the pristine graphene, produced here, is located at 1583-1588 cm^{-1}. There are many factors, which can affect the position of the G band, such as doping [107], layer number [108, 109], defects [110], strain [111], substrate [112], et al. The 2D band is the most prominent feature in the Raman spectrum of graphene, and its shape is sensitive to the number of layers of graphene [108, 113-115]. It was observed three types of 2D band of the N-doped graphene. In most cases, the shape of 2D band is a broad peak at 2650 cm^{-1}, corresponding to the few layer graphene, as bilayer and few-layer has a much broader and up-shifted 2D band compared with single-layer graphene [108]. The other two types can only be occasionally detected. One is a sharp peak at 2620 cm^{-1}. This part of graphene should be single layer, as the 2D band of single layer graphene is located at lower frequency with a shape of a single sharp peak [113, 116] and this shape is highly sensitive to identify the single-layer graphene [108]. The other type is a broad peak at 2661cm^{-1}, corresponding to the graphitic graphene. The higher frequency component of the 2D band increases, compared with few-layer graphene, as the further increase in graphitic layers will lead to a significant decrease of the relative intensity of the lower frequency component [108, 113]. Therefore, based on the Raman characterization, the layer of graphenes containing could be identified.

The XPS spectra confirm the doping structure of graphene. Figure 2-7 shows the XPS of nitrogen doped graphene and its bonding structure. In the XPS spectra, the peaks at 284.8, 401.6, and 531.9 eV correspond to C 1s of sp^2 C, N 1s of the doped N, and O1s of the adsorbed oxygen, respectively, and the atomic percentage of N in the sample could also be identified. There are three components in the C1s spectrum of the N-doped graphene. The main peak at 284.8 eV corresponds to the graphite-like sp^2 C, indicating most of the C atoms in the N-doped graphene are arranged in a conjugated honeycomb lattice. The small peaks at 285.8 and 287.5 eV reflect different bonding structure of C-N bonds, corresponding to the N-sp^2 C and N-sp^3 C bonds, respectively, and would originate from substitution of the N atoms, defects or the edge of the graphene sheets [116]. In the pristine graphene, the N 1s peak is absent, while in the N-doped graphene, the N 1s peak has three components, indicating that N atoms are in three different bonding characters inserted into the graphene network. The small peak at 398.2, 400.1 eV co po d o “py d ”, “py ol ” N, p v ly. T y f o N om lo d π y m o or two p-electrons, respectively [117, 118]. The peak 401. V o po d o “g p ” N, f o N om pl g he C atoms inside of the graphene layer [118]. The peak for “graphitic” N is much higher, thus the N atoms are substitutionally doped into the graphene lattice and mainly in the form of “graphitic” N. The O1s peak arises from the oxygen or water absorbed on the surface of the N-doped graphene [117, 119, 120], as this peak obviously decreases after heating in vacuum. The work of reference [121 synthesized N-graphene, XPS of C 1s are 284.9, 285.5, and 286.5 eV respectively; for N 1s are 399.1, 401.2 and 402.7 eV respectively. In other reference [122, 123], even the C 1s and N 1s components showed a little difference from referred above, they stand for the same corresponding bonding structures.

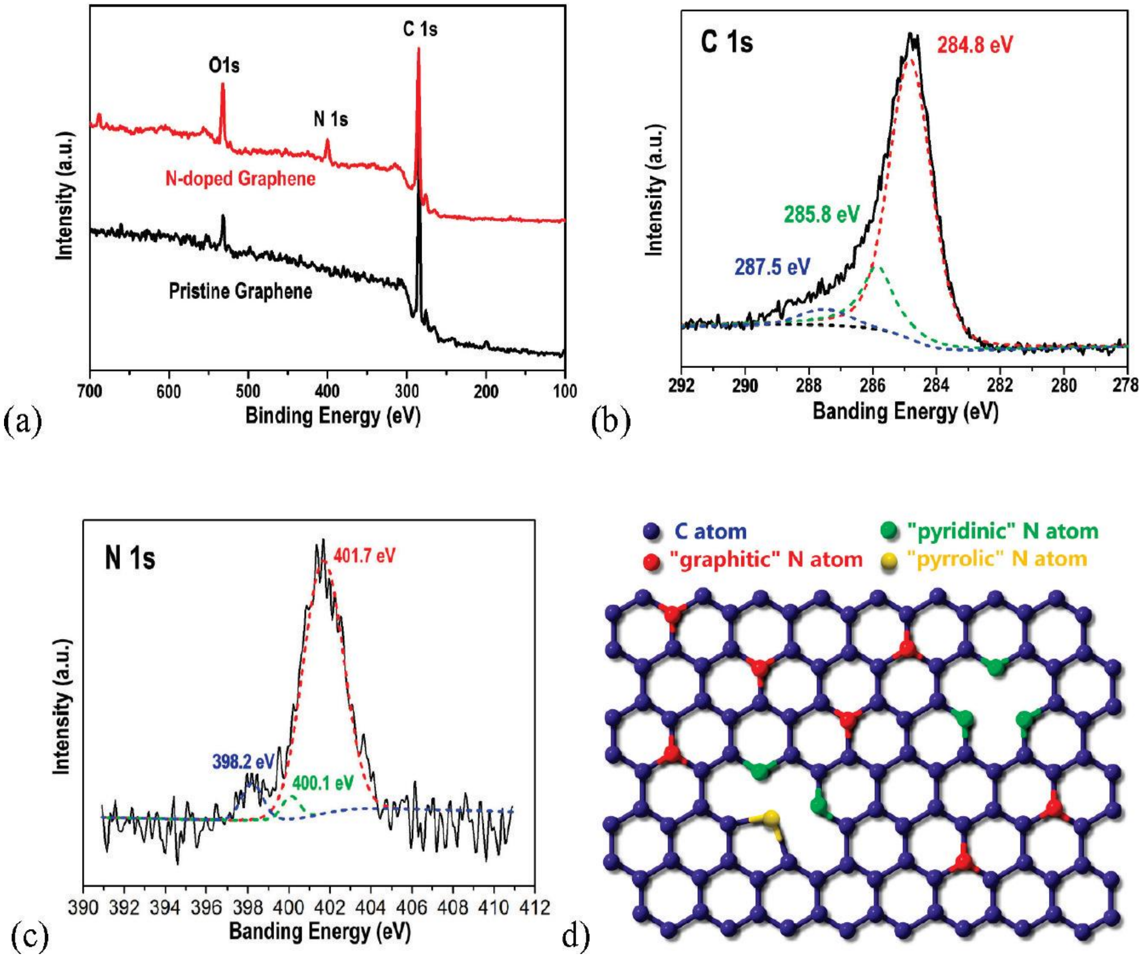

Figure 2-7 (a) XPS spectra of N-doped graphene and the high-resolution of (b) C1s and (c) N1s XPS spectra, (d) Schematic representation of the N-doped graphene (from reference [103]).

Nitrogen-doped graphene as efficient metal-free electrocatalyst for oxygen reduction reaction, which was demonstrated with a much better electrocatalytic activity, long-term operation stability, and tolerance to crossover effect than platinum[91]. The steady-state catalytic current at the N-graphene electrode was found to be 3 times higher than that at the Pt/C electrode over a large potential range. N-graphene electrode was confirmed that could show high electrocatalytic selectivity against the electro-oxidation of various commonly used fuel molecules, including hydrogen gas, glucose, and methanol. And it also was insensitive to CO, whereas the Pt/C electrode was rapidly poisoned under the same conditions. The stability of the N-graphene electrode toward ORR was also tested. There was no obvious decrease in current observed after 200000 continuous cycles between -1.0 and 0 V in air-saturated 0.1 M KOH. Nitrogen doped g p l od ’ x ll l y p op y o d ORR b d o u qu electronic property. Experimental results are shown as figure 2-8.

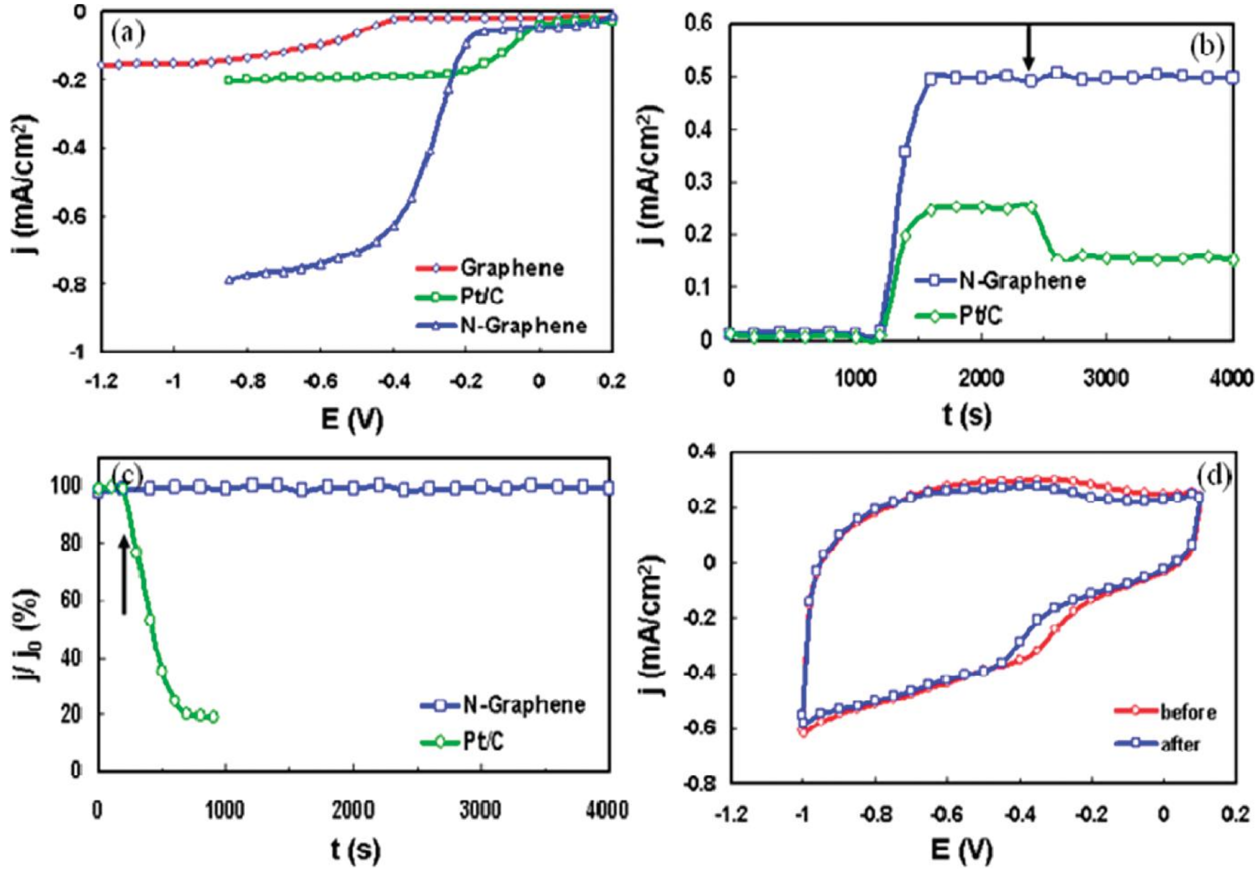

Figure 2-8 (a) RRDE voltammograms for the ORR in air-saturated 0.1 M KOH; (b) Current density (j) - time (t) chromoamperometric responses; (c) Current-time chromoamperometric response of electrodes to CO; (d) Cyclic voltammograms of N-graphene before and after a continuous potentiodynamic swept(from reference [91]).

Because of the amazing results of [91] works, there are many researchers fabricating nitrogen doped graphene using different methods [92-96], these nitrogen doped graphenes show high electrocatalytic activities to ORR.

ORR on cathode is the pivot reaction on fuel cell. This reaction is a kinetically slow process [124], which dominates the overall performance of a fuel cell. As reviewed by Yeager, [125] two oxygen reduction mechanisms are considered to lead to water product: the direct four-electron pathway where the oxygen is reduced to water at the standard electrode potential U^0 = 1.229 V:

$O^2 + 4H^+ + 4e^- \rightarrow H_2O$ (2-1)

And a pathway where oxygen is first reduced to hydrogen peroxide (U^0 =0.695 V) by a two-electron reduction, followed by a second two-electron reduction to form water (U^0 = 1.763 V):

$O_2 + 2H^+ + 2e^- \rightarrow H_2O_2$ (2-2)

$H_2O_2 + 2H^+ + 2e^- \rightarrow H_2O$ (2-3)

The four-electron reduction to water is the desired reaction and the two-electron reduction to hydrogen peroxide is to be avoided. There have been some theoretical studies about the mechanisms of ORR on electrode materials from traditional Pt, Pt alloys to nitrogen doped graphene [126]. Zhang and Anderson [127, 128] employed the hybrid density functional B3LYP theory in Gaussian 03 exploring the oxygen reduction reaction on platinum. Four electron transfer steps were presented in alkaline environment. It was shown that O_2^- (ads) is the first reduction product and that on an open unrestrained surface site it dissociated into O (ads) + O^- (ads), which were subsequently reduced to two water molecules and four OH^- (aq). Before this work there was theoretical [127, 128] evidence that on platinum electrodes in acid electrolyte the first reduction step forms adsorbed peroxyl radical, OOH (ads). It might form H_2O_2, or dissociate and then three electron and proton transfers reduce the O (ads) + OH (ads) to two water molecules. For non-platinum metal catalyst such as carbon-supported Fe-Phthalocyanine (FePc) and Co-Phthalocyanine (CoPc) as electrode catalysts for fuel cell, the ORR mechanisms in alkaline environment on them were explored using density functional theory (DFT) method by Chen and Wang. [129] Their calculations indicated that the ORR pathways, $2e^-$ or $4e^-$, were mostly determined by the structure of H_2O_2 adsorption on FePc and CoPc catalysts. Anderson et al. [130] studied the oxygen reduction on nitrogen doped graphene with nitrogen located on the basal plane of graphene using DFT method. They exposed two electron transfer reaction pathway. Vayner and Anderson [131] presented the ORR mechanisms on nitride graphite edge and a cobalt center bonded to nitrogen atoms by DFT method in the Gaussian 03 package. They obtained that isolated N substituting for CH at graphite edges was inactive toward the $2e^-$ and $4e^-$ reduction of oxygen. Over the Co site bridging two N substituting for CH on the edge structure, it showed favorable reversible potentials for the intermediate steps of ORR. However it was likely to be poisoned by a strongly held water molecule and not stable due to cobalt dissolution as soluble Co^{2+}. Yu et al. [132] using DFT method studied the ORR mechanisms on the nitrogen doped graphene electrode under the condition of electropotential of ~0.04 V (vs. NHE) and pH of 14. The calculations were carried on under experimental conditions taking the solvent, surface adsorbates, and coverages into consideration. They considered the carbon atom neighboring the substituting nitrogen atom as the electro-catalytic active site. They tested the ORR pathway on the cathode in alkaline solutions. They confirmed that O_2 could be reduced following two different mechanisms: associative and dissociative mechanisms. Their reaction pathways were summarized as following:

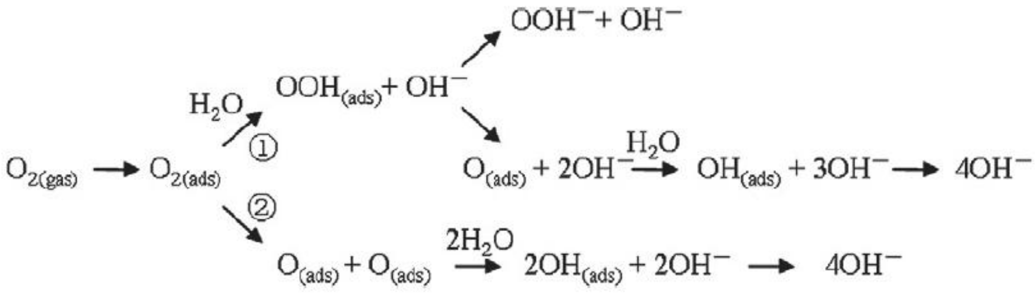

Figure 2-9 Oxygen reduction reaction paths in alkaline solution on nitrogen doped graphene (from reference [132]).

They confirmed that O_2 m l y du d v “4 - du o p y” d f vo d associative mechanism.

2.4.2 Boron doped graphene

Boron atom as “p” yp dop d om m o du o m l, ould l o substitute carbon atom on graphene forming boron doped graphene. It is of fundamental interest because theoretical study showed a sufficiently high boron concentration gave rise to quantum interference effects without affecting the outstanding transport properties of graphene [133]. Furthermore, it has been shown that, in nanoribbons, the bonding of boron at the edges can induce a transition from metallic to semiconducting behaviors [134]. Based on these fantastic electronic, photonic properties of boron doped graphene, it has been usedin transistor [135], energy storage and transforming devices [136-140].

The excellent electronic and photonic properties of boron doped graphene relate to its intrinsic structure. Raman spectroscopy, X-ray photoelectronic spectroscopy, SEM, TEM and AFM et al. are efficient methods to character the structure of boron doped graphene. Raman spectroscopy is the most effective and no-destructive technique to characterize the structure and quality of carbon materials, in particular to determine the defects, disordered structures, and the layers of graphene. Figure 2-10 [136] is a Raman spectra of boron-doped graphene (BG) on a micro-Raman spectrometer at an excitation wavelength of 514 nm. For compared, the Raman spectra of pure graphene and BG were shown in the same picture.

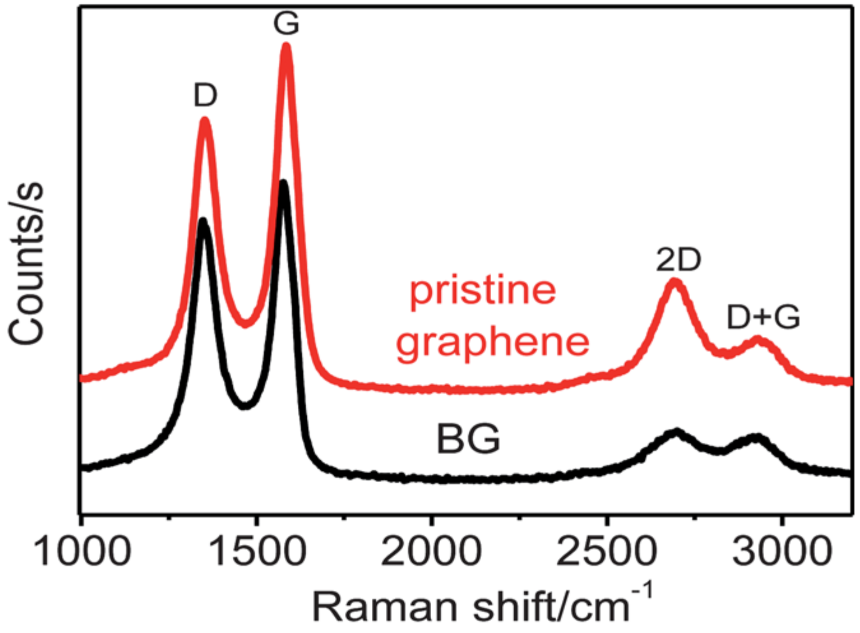

Figure 2-10 Raman spectra of Boron doped graphene and pristine graphene (from reference [136]).

The Raman spectrum of BG exhibits an intense G band at 1576 cm^{-1}, a highly intense D band at 1347 cm^{-1} and a wide 2D band at 2696 cm^{-1}. Whereas for the pristine graphene the G and 2D band are located at 1579 cm^{-1} and 2694 cm^{-1}, respectively. The intensity of the D band is strongly associated with the disorder degree of graphene, while the G band corresponds to the first-order scattering of the stretching vibration mode observed for sp^2 carbon domains. 2D band is associated with the second order two-phonon process, activated by double resonance processes. There are no significant shifts or line broadening, which clearly suggests that the graphene structure is retained after boron doping. The slightly larger I_D/I_G value (0.87) for BG compared with pristine graphene (0.8) indicates that the BG possesses many more defects than the pristine graphene prepared under similar conditions. The Raman spectra of boron-doped graphene fabricated with different methods [110, 141, 142] show the similar characters as narrated above.

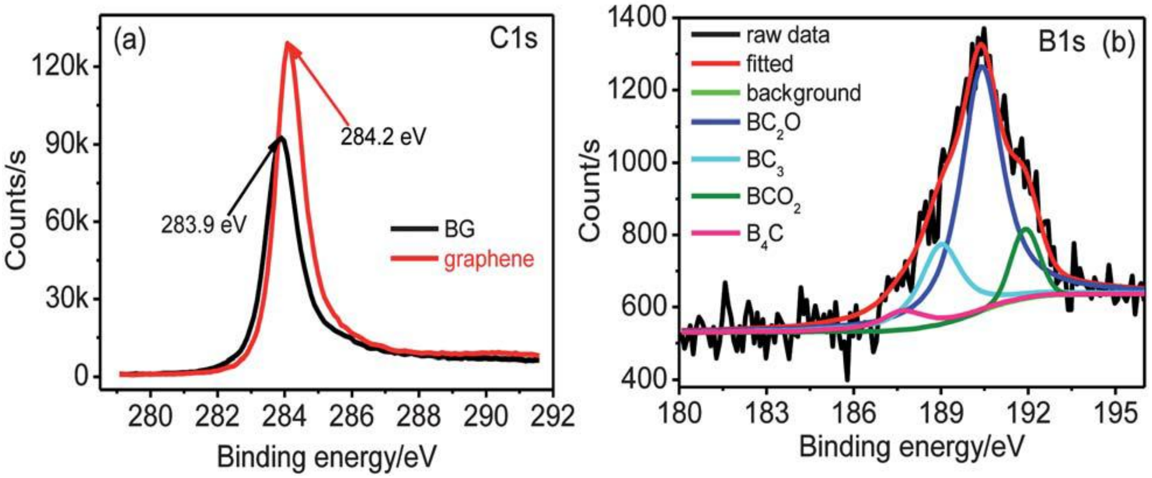

Figure 2-11 XPS of boron doped graphene (from reference [136]).

X-ray photoelectron spectroscopy (XPS) characterization could be used to explore the content and configuration of doped boron in the graphene structure. The full range XPS analysis of BG sample usually shows three peaks centered at B1s 190.4 eV, C1s 283.9eV and O1s 531.6 eV[136], corresponding to the presence of boron, carbon and oxygen atoms. Only the core levels of C1s (284.2 eV) and O1s (531.6 eV) could be observed from the survey scan for the pristine graphene. In the high resolution spectra, the intense C1s peak for BG with an asymmetric shape shifts to a lower binding energy compared to the pristine graphene, as shown in figure 2-11 (a). The decreased binding energy of the C1s peak might be due to the formation of B-C bonding, which reduces the Fermi l v l v d bu o of π-electron within the graphene structure. Moreover, the peak intensity of BG at ~284 eV is lower than that of pristine graphene, indicating that, due to boron doping, the graphene structure is broken to some extent and the number of sp^2-bonded carbon atoms decrease. In the high revolution B1s spectrum, the observed up-shift of the B1s signal indicates boron has been incorporated into the sp^2 carbon networks. After curve fitting for the B1s spectrum, the peaks centered at 187.7eV and 189.0eV may be assigned to B_4C and BC_3 structures, respectively. The peak at 190.4eV corresponds to the structure of boron atoms bonding to carbon and oxygen atoms (BC_2O). The signal 191.9 eV reveals that boron atoms are surrounded by carbon and oxygen atoms (BCO_2). All these results indicate the formation of B-C bonds in the annealing process. For others Boron doped graphene, their X-ray photoelectronic spectra show the similar characters with description. It is just these bonding structure and tiny change to the pristine graphene structure making its applications broadly, especially in energy storage and transformation.

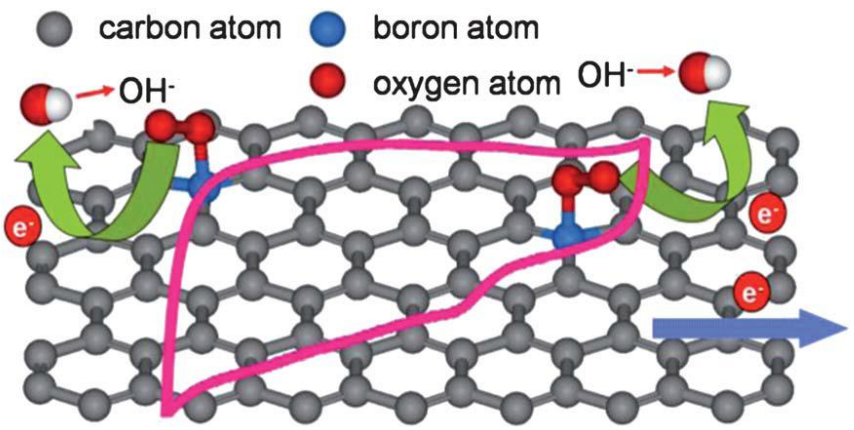

Figure 2-12 Boron doped graphene as efficient metal-free cathode of fuel cell (from reference [136])

The doped Boron atom can modify the electronic band structure of graphene, and consequently tune the mechanical properties and electrocatalytic activity. Recently boron doped graphene was fabricated and confirmed that it could be the efficient metal-free cathode in fuel cells. Zhen-Huan Sheng et al. [136] synthesized boron doped graphene (BG) with atomic percentage of 3.2% via a catalyst-free thermal annealing approach in the presence of boron oxide. It exhibits excellent electrocatalytic activity towards (ORR) in alkaline electrolytes, similar to the performance of Pt catalysts. And also it shows long-term stability and good CO tolerance superior to that of Pt-based catalysts. The transferred electron number (n) per oxygen molecule in the ORR process at the BG was calculated as 3.5 over the potential range from -0.4 to -0.9 V, which reveals that the electrocatalytic process is a one-step four-electron pathway for ORR with a much higher peak current. BG is an excellent metal-free catalyst towards ORR, free of poisoning effects from fuel molecules such as methanol and CO, which is much better than the platinum-based catalysts. In addition, the BG catalyst shows considerable stability during

ORR. The electron deficient boron atoms doped in graphene may function as active sites for oxygen adsorption and activating the O-O bond cleavage.

2.4.3 Boron-nitrogen co-doped graphene as efficient catalyst of fuel cells

In addition to nitrogen, boron sole-doped graphene, nitrogen-boron co-doped graphenes were also fabricated by different methods [143-145]. Nitrogen and boron atoms tuned the electronic and photonic properties of graphene together, made it show fantastic properties and resulted in broad application of doped graphene in different fields. Wang et al. [143] and Choi et al. [144] synthesized boron-nitrogen co-doped graphene by different methods separately. The boron-nitrogen co-doped graphene showed superior electrocatalytic activities on ORR of fuel cell compared with commercial Pt/C electrocatalyst. Wu et al. [145] obtained nitrogen-boron co-doped monolithic graphene aerogels, which had high performance on all-solid-state supercapacitors. Zheng et al. obtained the B, N-graphene, which showed excellent activity in the ORR and perfect selectivity for the four-electron ORR pathway in an alkaline medium. Its activity and four-electron pathway selectivity in the ORR is much higher than that observed for singly B- or N- doped graphene. They applied DFT calculation, and revealed the origin of the synergistic effect in a B-C-N structure for ORR. In a B-C-N bonding structure, the 2p orbital of the C atom that is located between the N and B dopants was first polarized by N, which is then able to donate extra electrons to an adjacent B atom. Consequently, the el o o up y of p o b l of “ v d” B om d o f l its adsorption and bonding with H_2O. This charge-transfer process induces a synergistic coupling effect between N and B dopants, in which N has the role of an electron-withdrawing group to indirectly activate B and thus make the latter an active site to enhance the ORR activity. Among various B-C-N functional configurations in a heteroring, a B atom meta to a pyridinic N atom show the highest E_{ad} value, whereas an ortho B atom directly bonded to N (both pyridinic and graphitic forms) as BN has the lowest activity owing to the lack of the C bridge. However Lyalin et al. [146] using DFT method simulated the ORR process on hexagonal boron nitride (h-BN) monolayer graphene, they considered that h-BN did not likely possess catalytic activity for ORR only if there were defects on the h-BN.

2.4.4 Sulfur doped graphene

Sulfur doped graphene were also synthesized by different methods [147-150]. They exhibit good electrocatalytic activity for oxygen reduction reaction and influence the discharge product formation in lithium-oxygen batteries. Zhi Yang etc. [147] successfully fabricated sulfur-doped graphene (S-doped graphene) by directly annealing graphene oxide (GO) and benzyl disulfide (BDS) in argon. The annealed temperatures were 600-1050 ˚C. T o of dop d ul fu om ~0.6 om %.

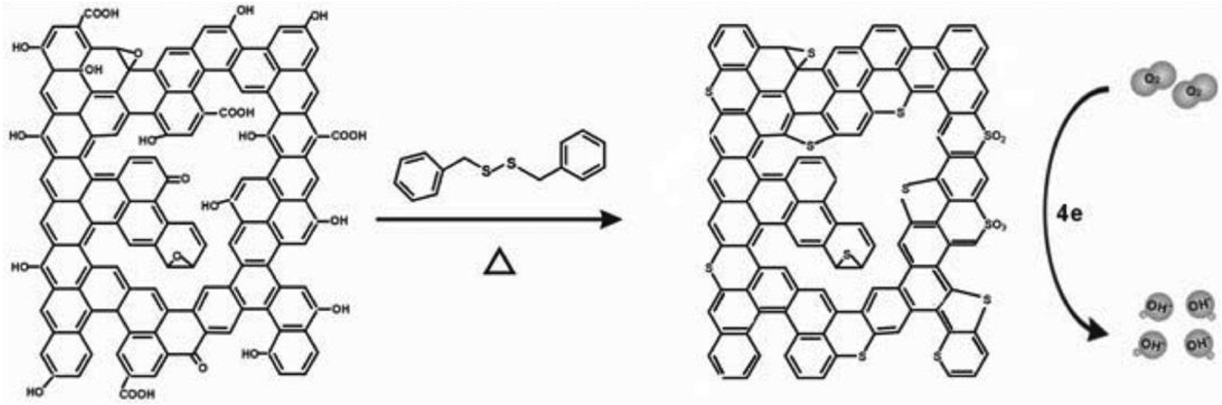

Figure 2-13 Schematic illustration of S-graphene preparation and its catalytic property to ORR (from reference [147]).

Yang etc. [148] also successfully synthesized Sulfur doped graphene vi thermal reaction between graphene oxide and guest gas H_2S on the basis of ultrathin graphene oxide-po ou l mp u f om 500 o 900 ˚C. T ov ll o of sulfur in the SG prepared at 500-900 ˚C o ly g of 1. -1.7 atom%. It is g SG of Y g ' , bu ll mu lo itrogen content (X%) in NG [149]. Figure 2-14 (a) shows the TEM imagine of sulfur doped graphene with a thickness about 1nm, confirming the single-layer feature. Figure 2-14 (b) was XPS survey spectra and (c) Raman spectra of GO, SG. The typical ramman spectra of SG exhibit two remarkable peaks at about 1330 and 1600 cm^{-1}, corresponding to the D and G band, respectively [151]. The intensity of D band of SG was lower than that of GO, indicating that the graphitic degree of SG improved. Furthermore, with the increase of the annealing temperature, the I_D/I_G value of sulfur doped graphene decrease. Yang has the similar results of that they even fabricated the SG with different methods. With increase the annealing temperature, the SGs show higher graphitic degree. They also got the high resolution C1s XPS spectra of GO and SG with C1 and C2 figure 2-14 (d) and S2p XPS spectra of SG, as figure 2-14(e). The S2p peaks of SG can be again resolved into three different peaks at the binding energies of ~ 163.9, 165.1 and 168.5 eV, respectively. The former two peaks stand for the 2p3/2 (S1) and 2p1/2 (S2) positions of thiophene-S. The third peak should arise from some oxidized sulfur (S3). Other sulfur components such as thiol (SH) can not be detected in the XPS spectra. Thereby, it can be inferred that the sulfur is mainly doped at the edges and defects of graphene in the form of thiophene-like structures. They analysed the content of sulfur species (S1, S2, and S3) in SG showing as figure 2-14 (f). The thiophene-S structures dominate the most ratio of S-doped graphene.

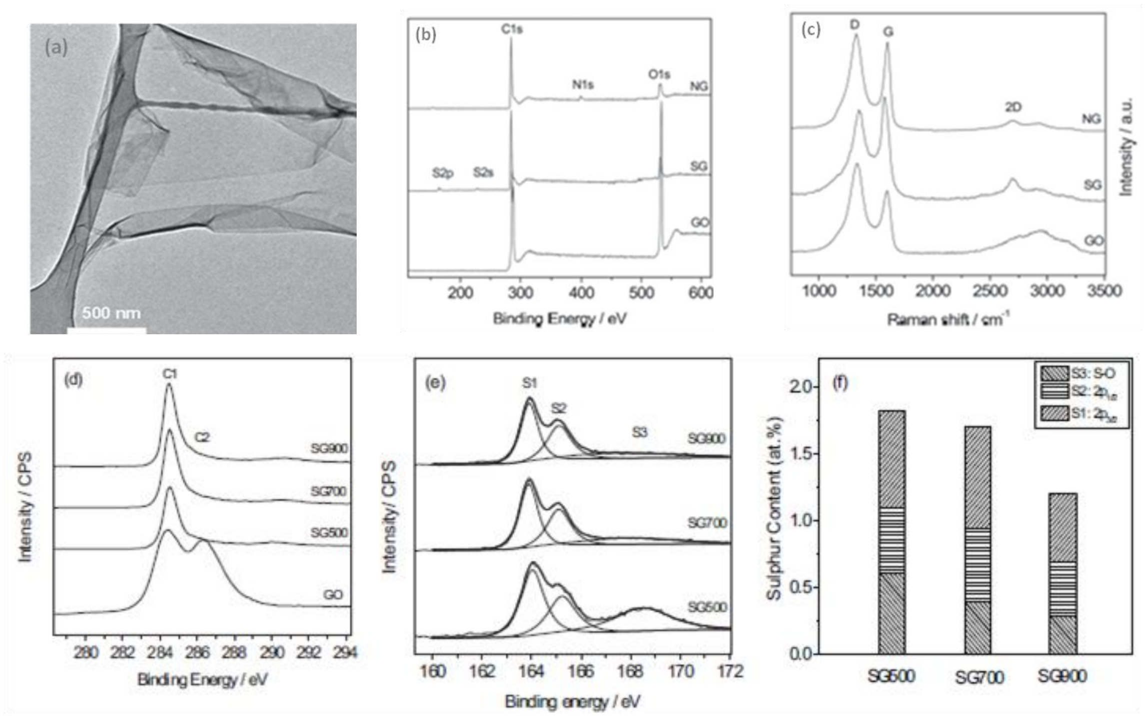

Figure 2-14 (a)Typical TEM image of sulfur doped graphene; (b) XPS of sulfur doped graphene; (c) Raman spectroscopy of sulfur doped graphene (from reference[151]); (d) High resolution C1s XPS spectra of GO and SG with C1 and C2; (e) High resolution S2p XPS spectra of SG. The peaks are fitted to three energy components centered at around 163.9, 165.1 and 168.5 eV,corresponding to Sp3/2 (S1), Sp1/2 (S2), and S-O (S3), respectively; (f) The content of sulfur species (S1,S2, and S3) in SG sheets (from reference [147]).

Sulfur doped graphene synthesized by Yang et al. and Yang et al. both exhibit excellent catalytic activity for ORR. Figure 2-15 (a) shows the cyclic voltammograms for graphene-900 and S-graphene 900 which was synthesized by the former. Figure 2-15 (b) shows the linear sweep voltammetry (LSV) curves for their S-graphene and a Pt/C catalyst on a glass carbon rotating disk electrode saturated in O_2 at a rotation rate of 1600 rpm. Figure 2-15 (c) shows the rotating ring disk electrode (RRDE) linear sweep voltammograms of 1600 rpm of S-doped graphenes in reference [148]. These experimental results all shown that the S-doped graphene exhibiting good catalytic properties.

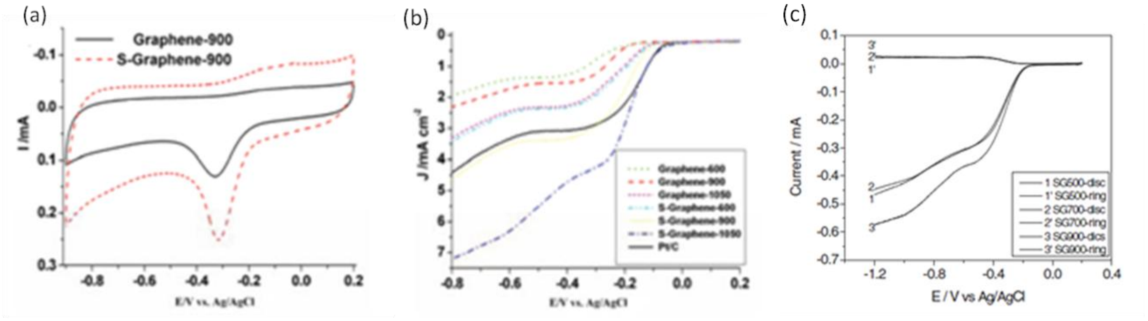

Figure 2-15 (a) Cyclic voltammograms for graphene-900 and S-graphene-900; (b) Linear sweep voltammograms (LSV) curves for various S-doped graphenes (from reference [147]) and a Pt/C catalyst on a glass carbon rotating disk electrode saturated in O_2 at a rotation rate of 1600 rpm; (c) Rotating ring disk electrode linear sweep voltammograms of S-doped graphenes (from reference [148]) at a rotation rate of 1600 rpm.

One critical challenge for the practical application of lithium-oxgen batteries is to develop an optimal porous cathode since the insoluble product, lithium peroxide (Li_2O_2), deposits in and eventually will clog the electrode pores which limits the discharge capacity. Another challenge is the poor rate capability and significant polarization of cell voltage which is also due to the formation of Li_2O_2.)

Li et al. fabricated the sulfur-doped graphene with graphene dispersed into acetone with p- olu ulfo d, d d lu y, d d 100 ˚C d f lly l d 900 ˚C A fo l ou . Sulfur atom has the similar bonding structures on the graphene with other peopl ’ S-doped graphene [147, 148]. They found that S-GNSs could be the cathode materials for lithium-oxygen batteries. Sulfur on the graphene could be favorable to a nanorod-shape of Li_2O_2 formation during the discharge. So the charge properties were considered to be due to sulphur-doping.

For the electronic properties of S-doped graphene, there is no report on it, and ORR mechanisms on S-doped graphene are not studied yet. So the theoretical study of S-doped graphene properties would pave the road for the wide application of this kind of hetero-doped graphene, especially for energy conversion and storage.

2.4.5 Halogen element doped graphene

Chlorination is one of an effective chemical modification for band gap engineering of graphene, which is appealing for electronics applications since it facilitates the scalable fabrication of graphene-based devices without breaking their resilient C-C bonds. Li etc. [152] demonstrated a photochemical chlorination of graphene through the covalent attachment of chlorine radicals to the basal carbon atoms of graphene. In their research, X-ray photoelectron spectroscopy revealed that chlorine is grafted to the basal plane of graphene, with about 8 at.% chlorine coverage. Figure 2-16 (a) shows the time evolution of Raman spectra for a single-layer graphene sample after a series of photochlorination reactions. The characteristic disorder-induced D band at 1330 cm^{-1} emerges as the photochlorination time increases. In addition, the double resonance 2D band around 2654 cm^{-1} significantly getting weaker, the G band around 1587 cm^{-1} broadens due to the presence of a defect-induced D' should peak at 1620 cm^{-1}[153]. These observations strongly suggest that the covalent C-Cl bonds were formed and thus a high degree of structural disorder was generated by the transformation from sp^2 to sp^3 configuration. XPS was also performed to determine the composition and bonding type of the photochlorinated graphene (Figure 2-16 (b) and (c)). The prominent Cl 2p peaks at 200.6 eV ($2p_{3/2}$) and 202.2 eV ($2p_{1/2}$) are assigned to C-Cl bonds, unequivocally indicating the covalent bond formation between Cl and graphene. C1s peak can be fitted with three different bonding energy at 284.8, 286.6 and 289.0 eV, assigned to C-C, C-Cl, and O-C=O bonds, respectively [154]. Wu etc. [155] applied chemical modification to graphene using chlorine plasma reaction. TEM images of pure GNRs, GNR treated for 1 min in Cl_2 plasma, and GNR treated for 180s in Cl_2 plasma are shown in figure 2-16 (d-f), which shows obvious disorder and defects within the plane of the GNRs (Figure 2-16(f)). The Raman spectra and XPS spectrum of graphene after chlorine plasma treatment showed the similar characters with the results from Li et al. The (XPS) X-ray photoelectron spectroscopy spectrum revealed a coverage of 8.5 atom % Cl.

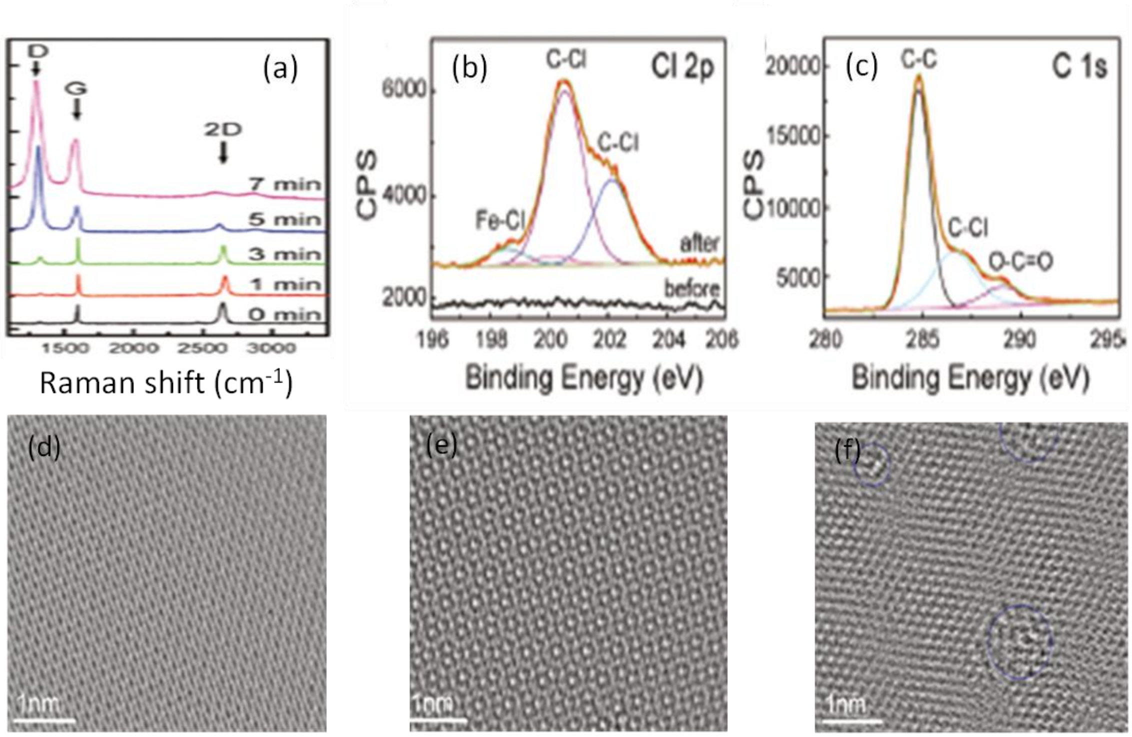

Figure 2-16 (a) Raman spectra evolution for single-layer graphene reacted with chlorine under xenon lamp irradiation. (b), (c) High-resolution XPS spectra of Cl 2p and C 1s in the photochlorinated graphene (from reference [153]); (d-f) TEM images of in-plane regions for Graphene nanoribbon treated for 0, 1 min. and 3min. in Cl_2 plasma (from reference [152]).

Simulation methods were performed to study the chlorine bonding structure and electronic property of these chlorination graphene. Wu et al. applied ab initio simulations to calculate the bond length of chlorination graphene, as shown in figure 2-17. Yang et al performed density of functional theory (DFT) to investigate the chlorination of graphene. They obtained that Cl atoms could generate various states on graphene surface. Cl-graphene charge transfer complex, where the C orbitals keep sp^2 hybridization and the graphene is p-type doped. Covalent bonding Cl pairs, where the structure of the C atom is close to sp^3 hybridization. The other is chlorine atoms formed cluster on graphene as the Cl coverage increased. These three different structures are shown in figure 2-17. There is still no definite relationship of chlorine coverage percent vs. chlorine bonding structure. The electronic properties of chlorine doped graphene were also studied from experimental to theoretical methods. Wu obtained the results with increasing the Cl plasma treatment time, the resistance of graphene decreased at first then increased. The maximum conductance (measured at Vg = -40 V) of 1 min Cl plasma-treated GNR was found to increase by 1.3-2.2 times the initial conductance in the ambient air. They explained the increase in conductance due to doping of graphene sheet instead of a purely contact effect. However what coverage percent could make the chlorination graphene o lo u l . Fo L' poo m l lo o g p , room temperature resistance increased significantly with prolonged reaction time. Meanwhile, the carrier mobility decreased. The significant reduction of conductivity was interpreted as the scenario where photochlorination may interrupt the conjugated system, du g o du g π-orbital, introduce scattering centers, or open up the band gap. The conductivity of doped graphene is an important determinant factor for its applications in energy storage and transformation fields. So there are still further work to do in study the conductivity of different coverage percent chlorine doped graphene.

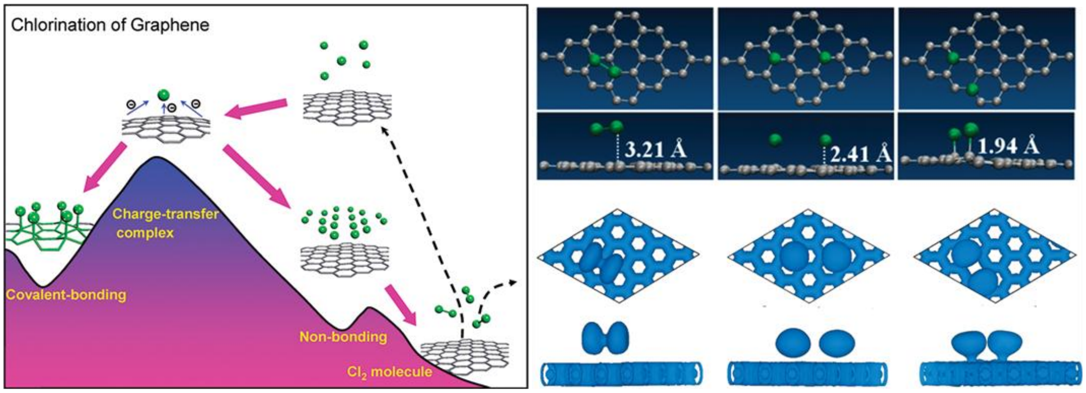

Figure 2-17 Chlorine on graphene surface with different states: Covalent-bonding, charge-trasfer complex, non-bonding (from reference [156]).

Because of the special characters of chlorine doped graphene in electronics and photonics, it would show good potential applications on fuel cell, solar cell and transistor etc.. Our collaborator already synthesized chlorine doped graphene using ball milling of graphite in presence of chlorine gas, which showed remarkable electrocatalytic activity for oxygen reduction reaction [157]. The ORR electrocatalytic mechanisms on the Cl doped graphene are still not clear.

There are other hetero-atom doped graphene applying as electrocatalyst of fuel cells, such as Se [158], P [159]. Phosphorus and Nitrogen co-doped vertically aligned carbon nanotube [160], sulfur and nitrogen co-doped graphene [161] were fabricated and confirmed showing high electrocatalytic property for ORR.

2.5 Summary and Outlook

Since 2004, Novoselov and Geim [162] obtained graphene for the first time using a technique called micromechanical cleavage. It has extracted extensive attentions due to its fantastic properties. Scientists and engineers are trying to explore all kinds of simple, efficient, and low-cost fabrication methods to get high quality graphene. During the fabrication process, defects are inevitably induced on the graphene. These defects can alter properties of graphene. In order to get graphene with particular properties corresponding defects are introduced on graphene intentionally, such as hetero-atom doping structures; which can be used as ORR electrocatalyst materials for fuel cells. Recently, nitrogen, boron, sulfur, chlorine, and nitrogen-boron doped graphene were confirmed showing as good even better electrocatalytic property to ORR, which would advance fuel cells for broad application in commercial. The study of ORR mechanisms on these hetero-atom doped graphene is very important for improving the catalytic property of these materials. For the nitrogen doped graphene, much work has been done. The nitrogen doping structure, the catalytic active sites on the doped graphene, the electron transfer processed of ORR, all these aspects have been exploring. But for other hetero-atom doped graphene, such as boron, sulfur, chlorine, phosphors doped graphene, little is know about ORR mechanisms, and more work is needed in this field. First, it is of importance to figure out what relationship between the doped structure and catalytic properties, especially what kind of physical, chemical and electronic properties determine the catalytic property. The results could provide guidelines for the fabrication of these catalytic materials. Second, it is essential to unerstand how to control the fabricating process in order to get optimal structures, which facilitate the ORR catalytic activities. This could dramatically decrease the manufacturing cost and improve efficiency of catalysts. Third, it is needed to search for more efficienct catalysts for fuel cells based on the theoretical work.

CHAPTER III

SIMULATION METHOD

Density functional theory (DFT) was applied calculating the electronic properties of doped graphene and simulating the electron transfer processes of ORR based on the Gaussian 03, 09 packages. The principle of this method is quantum mechanics.

3.1 SchrÖdinger equation

Density functional theory-based methods derived from quantum mechanics f om 19 0 ’, p ll y T om -Fermi-Dirac model, and from Sl ’ fu d m l o k qu um m y 1950’. Qu um m x pl o entities like electrons have both particle-like and wave-like characteristics. The SchrÖdinger equation describes the wave function of a particle:

$$\left\{\frac{-h^2}{8\pi^2 m}\nabla^2 + V\right\}\Psi(\vec{r},t) = \frac{ih}{2\pi}\frac{\partial\Psi(\vec{r},t)}{\partial t} \qquad 3\text{-}1$$

where Ψ v fu o, m m of p l, Pl k’ o , d V po l f ld p l mov g. T p odu of Ψ ompl x o jug (Ψ*Ψ, of $|\Psi|^2$) is interpreted as the probability distribution of the particle. The SchrÖdinger equation for a collection of particles like a molecule is very m l . I , Ψ ould b fu o of oo d of ll p l system as well as t. The energy and any other properties of the particle can be obtained by olv g S Öd g qu o fo Ψ, ubj o pp op bou d y o d o . If V is not a function of time, the SchrÖdinger equation can be simplified using the mathematical technique known as separation of variables. If we write the wavefunction as the product of a spatial function and a time function:

$$\Psi(\vec{r},t) = \psi(\vec{r})\,\tau(t) \qquad 3\text{-}2$$

and then substitute these new function into Equation 3-1, we will obtain two equations, one of which depends on the position of the particle independent of time and the other of which is a function of time alone. For the problems in which we are interested, this separation is valid, and we focus entirely on the familiar time-independent SchrÖdinger equation:

$$H\psi(\vec{r}) = E\psi(\vec{r}) \qquad 3\text{-}3$$

Where E is the energy of the particle, and H is the Hamiltonian operator, equal to:

$$H = \frac{-h^2}{8\pi^2 m}\nabla^2 + V \qquad 3\text{-}4$$

The various solutions to Equation 3-3 correspond to different stationary states of the particle (molecule). The one with the lowest energy is called the ground state. Equation 3-3 is a non-relativistic description of the system which is not valid when the velocities of particles approach the speed of light. Thus, it does not give an accurate description of the core electrons in large nuclei.

Fo mol ul y m, Ψ fu o of po o of l o d nuclei within the molecule, which we will designate as $\vec{r}$ and $\vec{R}$, respectively. These symbols are shorthand for the set of component vectors describing the position of each particle. We will use subscripted versions of them to denote the vector corresponding to a particular electron or nucleus: $\overrightarrow{r_i}$ and $\overrightarrow{R_I}$. Note that electrons are treated individually, while each nucleus is treated as an aggregate; the component nucleons are not treated individually. The Hamiltonian is made up of kinetic and potential energy terms:

$$H = T + V \qquad 3\text{-}5$$

The kinetic energy is a summation of ∇^2 over all the particles in the molecule:

$$T = -\frac{h^2}{8\pi^2}\sum_k \frac{1}{m_k}\left(\frac{\partial^2}{\partial x_k^2} + \frac{\partial^2}{\partial y_k^2} + \frac{\partial^2}{\partial z_k^2}\right) \qquad 3\text{-}6$$

The potential energy component is the Coulomb repulsion between each pair of charged entities (treating each atomic nucleus as a single charged mass):

$$V = \frac{1}{4\pi\varepsilon_0}\sum_j \sum_{k<j} \frac{e_j e_k}{\Delta r_{jk}} \qquad 3\text{-}7$$

where Δr_{jk} is the distance between the two particles, and e_j and e_k are the charges on particle *j* and *k*. for an electron, the charge is *–e*, while for a nucleus, the charge is *Ze*, where Z is the atomic number for that atom. Thus,

$$V = \frac{1}{4\pi\varepsilon_0}\left(-\sum_i \sum_I \left(\frac{Z_{Ie^2}}{\Delta r_{iI}}\right) + \sum_i \sum_{j<i} \left(\frac{e^2}{\Delta r_{ij}}\right) + \sum_I \sum_{J<I} \left(\frac{Z_I Z_J e^2}{\Delta R_{IJ}}\right)\right) \qquad 3\text{-}8$$

The first term corresponds to electron-nuclear attraction, the second to electron-electron repulsion, and the third to nuclear-nuclear repulsion.

3.2 Solution methods of SchrÖdinger equation

3.2.1 Born-Oppenheimer Approximation

Many different methods are used to simplify the solution of SchrÖdinger equation. The Born-Oppenheimer approximation is the first of several approximations used. It simplifies the general molecular problem by separating nuclear and electronic motions. The electron distribution within a molecular system depends on the positions of the nuclei, and not on their velocities. The Born-Oppenheimer approximation allows the two parts of the problem to be solved independently, so we can construct an electronic Hamiltonian which neglects the kinetic energy term for the nuclei. From this point on we will focus entirely on the electronic problem.

3.2.2 Hartree-Fock method

Hartree-Fock method finds its typical application in the solution of the electronic SchrÖdinger equation of atoms, molecules, and solids. It is also called self-consistent field method (SCF), which makes five major simplifications in order to deal with this task:

(1) The Born-Oppenheimer approximation is inherently assumed. The full molecular wave function is actually a function of the coordinates of each of the nuclei, in addition to those of the electrons.

(2) Typically, relativistic effects are completely neglected. The momentum operator is assumed to be completely non-relativistic.

(3) The variational solution is assumed the molecular orbital to be a linear combination of a finite number of one-electron functions known as basis functions, which are usually chosen to be orthogonal and normalized. The finite basis set is assumed to be approximately complete. Individual molecular orbital is defined as:

$$\phi_i = \sum_{\mu=1}^{N} c_{\mu i} \chi_\mu \qquad 3\text{-}9$$

where the coefficient $c_{\mu i}$ are known as the molecular orbital expansion coefficients. The b fu o χ_μ is in the same way that ϕ_i refers to an arbitrary molecular orbital.

Gaussian and other *ab* initio electronic structure programs use Gaussian-type atomic function as basis functions. Gaussian functions have the general form:

$$g(\alpha, \vec{r}) = c x^n y^m z^l e^{-\alpha r^2} \qquad 3\text{-}10$$

where $\vec{r}$ ompo d of x, y, z. α o d m g z (d l x) of the function. Linear combinations of primitive Gaussians are used to form the actual basis functions, which are called contracted Gaussians and have the form:

$$\chi_\mu = \sum_p d_{\mu p} g_p \qquad 3\text{-}11$$

where $d_{\mu p}$is fixed constant within a given basis set. So for molecular orbitals, they have

the following espansion:

$$\phi_i = \sum_{\mu=1}^{N} c_{\mu i}\chi_\mu = \sum_\mu c_{\mu i}\left(\sum_p d_{\mu p} g_p\right) \quad \text{3-12}$$

(4) Each energy eigenfunction is assumed to be describable by a single Slater determinant, an antisymmetrized product of one-electron wave functions. A Slater determinant is an expression that describes the wavefunction of a multi-fermionic system that satisfies anti-symmetry requirements and consequently the Pauli exclusion principle by changing sign upon exchange of fermions. The Slater determinant arises from the consideration of a wave function for a collection of electrons, each with a wave function known as the spin-orbital, a function of both the elect o ’ lo o d p [163].

(5) The mean field approximation is implied. Effects arising from deviations from this assumption, known as electron correlation, are completely neglected for the electrons of opposite spin, but are taken into account for electrons of parallel spin [164, 165]. (Electron correlation should not be confused with electron exchange, which is fully accounted for in the Hartree-Fock method.)

So the problem has now become how to solve for the set of molecular orbital expansion coefficients, $c_{\mu i}$. There are different methods to solve the expansion coefficients. Hartree-Fock theory takes advantage of the variational principle. For the solution of molecular orbital expansion coefficients, which are not linear in the equation [163] and must be solved iteratively. The procedure which does so is called the self-consistent field (SCF) method. At convergence, the energy is at a minimum, and the orbitals generate a field which produces the same orbitals.

3.2.3 Density functional theory method

Hartree-Fock theory provides an inadequate treatment of the correlation between the motions of the electrons within a molecular system, especially that arising between electrons of opposite spin. Including configuration interaction methods and Mϕller-Plesset perturbation theory, density functional theory (DFT) is an approach considering electron correlation method. DFT has its conceptual roots in the Thomas-Fermi model, and was put on a firm theoretical footing by the two Hohenberg-Kohn theorems. Within the framework of Kohn-Sham DFT, many-body problem of interacting electrons in a static external potential is reduced to a problem of non-interacting electrons moving in a effective potential. The effective potential includes the external potential and the effects of the Coulomb interactions between the electrons, e. g., the exchange and correlation interactions. The simplest approximation of exchange and correlation interaction DFT method is the local-density approximation (LDA).

Following on the work of Kohn and Sham, the approximate functional employed by current DFT methods partition the electronic energy into several terms:

$$E = E^T + E^V + E^J + E^{XC} \qquad 3\text{-}13$$

Where E^T is the kinetic energy term (arising from the motion of the electrons), E^V includes terms describing the potential energy of the nuclear-electron attraction and of the repulsion between pairs of nuclei, E^J is the electron-electron repulsion term (it is also described as the Coulomb self-interaction of the electron density), and E^{XC} is the exchange-correlation term and includes the remaining part of the electron-electron interactions. All terms except the nuclear-nuclear repulsion are functions of $\rho(\vec{r})$, the l o d y, fo o m l z d ψ g v b y

$$\rho(\vec{r}) = \int \psi * (\vec{r})\psi(\vec{r})\, d\vec{r} \qquad 3\text{-}14$$

$E^T + E^V + E^J$ o po d o l l gy of g d bu o ρ. T E^{XC} term arises from the antisymmetry of quantum mechanical wavefunction and dynamic correlation in the motions of the individual electrons. It is usually divided into separate parts, referred to as the exchange and correlation parts, but actually corresponding to same-spin and mixed-spin interactions, respectively:

$$E^{XC}(\rho) = E^X(\rho) + E^C(\rho) \qquad 3\text{-}15$$

Both components can be of two distinct types: local functional depend on only the l o d y ρ, l g d - o d fu o l d p d o bo ρ d g d , $\nabla\rho$.

There are still some difficulties in using density functional theory to properly describe intermolecular interactions, especially van der Waals forces (dispersion); charge transfer excitations; transition states, global potential energy surfaces and some other strongly correlated systems; and in calculations of the band gap in semiconductors. Its incomplete treatment of dispersion can adversely affect the accuracy of DFT (at least when used alone and uncorrected) in the treatment of systems which are dominated by dispersion (e.g. interacting noble gas atoms) or where dispersion competes significantly with other effects.

Recently, Becke has formulated functional which include a mixture of Hartree-Fock and DFT exchange along with DFT correlation, conceptually defining E^{XC} as:

$$E_{hybrid}^{XC} = c_{HF} E_{HF}^{X} + c_{DFT} E_{DFT}^{XC} \qquad 3\text{-}16$$

W ’ o . F o xample, a Becke-style three-parameter functional may be defined via the following expression:

$$E_{B3LYP}^{XC} = E_{LDA}^{X} + c_0 (E_{HF}^{X} - E_{LDA}^{X}) + c_X \Delta E_{B88}^{X} + E_{VWN3}^{C} + c_C (E_{LYP}^{C} - E_{VWN3}^{C}) \qquad 3\text{-}17$$

Here, the parameter $c_0$allows any admixture of Hartree-Fock and LDA local exchange to b u d. I dd o , B k ’ g d o o o LDA x g l o lud d, scaled by the parameter c_X. Similarly, the VWN3 local correction functional is used, and it may be optionally corrected by the LYP correlation correction via the parameter c_C. In the B3LYP functional, the parameters values are those specified by Becke, which he determined by fitting to the atomization energies, ionization potentials, proton affinities and first-row atomic energies in the G1 molecule set: $c_0 = 0.20$, $c_X = 0.72$ and $c_C = 0.81$.

3.3 Gaussian package and calculation method

3.3.1 Gaussian package

All the calculations in this dissertation are carried on by Gaussian 03 and 09 packages. Gaussian package can do molecular mechanics, semi-empirical calculations, SCF methods, Mϕller-Plesset perturbation theory, build-in DFT methods, ONIOM et al.

calculations. It can produce accurate, reliable and complete models, and also it is applicable to the full range of chemical conditions and problem sizes and across entire periodic table. Besides these, Gaussian provides state-of-the-art performance in single CPU, multiprocessor and cluster computing environment with very simple setting up. It is used to predict the energies, molecular structures, vibrational frequencies and molecular properties of molecules and reactions in a wide variety of chemical environments. We calculated the optimization structures, electronic properties of doped graphene and ORR processes on the doped graphenes. We chose the B3LYP DFT method with basis set of 6-31G (d, p).

3.3.2 Calculation method and basis set

We compared the reaction free energies of $O_2 + 2H_2 \rightarrow H_2O$ using different methods and basis set. Values of them are listed in the Table 3-1. Comparing the reaction f gy ΔG , y obv ou ly o B3LYP/6-31G (d, p), B3LYP/6-311G (d, p), MP2/6-31G (d, p) and MP2/6-311G (d, p) have the higher accurate. Considering the calculation expense, we chose B3LYP/6-31G (d, p) set, which show high accuracy and with the low calculation expense. Other researchers [166-168] also used the same method and basis set conducting the similar calculation, with credible results.

Table 3-1 R o f gy ΔG (V) of $O_2 + 2H_2 \rightarrow 2H_2O$ using different calculation methods and basis sets in standard states

Method	STO-3G	3-21G(d, p)	6-31G(d, p)	6-311G (d, p)
Hartree-Fock	-2.57	-5.12	-5.37	-5.43
DFT(B3LYP)	-1.52	-3.87	-4.74	-4.96
MP2	-0.72	-2.54	-4.79	-4.88
Experimental result	-4.92			

CHAPTER IV

OXYGEN REDUCTION REACTION MECHANISMS ON HETERO-ATOM DOPED GRAPHENE AS CATALYST OF FUEL CELL

In this chapter, the DFT method will be used to explore the oxygen reduction reaction (ORR) mechanisms on nitrogen and sulfur doped graphene as catalysts of fuel cells. Effects of doped structure, such as dopant atom concentration, position, bonding structure to the catalytic activity of these doped graphene are also carried on. First we build a graphene cluster which contains one nitrogen dopant atom, and explore the ORR process. Then we increase the number of nitrogen dopant atoms from one to four, and introduce the Stone-Wale defects on the doped graphene. Reversible potentials of ORR sub-reactions on these doped graphene are calculated and compared. Furthermore, the different types of sulfur doped graphene models are built, and the catalytic active sites on them are confirmed. Different electron transfer reaction processes are simulated on these ulfu dop d g p . R o f gy ΔG of ORR ub-reaction are calculated on the sulfur doped graphene. For the nitrogen, sulfur doped graphene, the electronic property of them are calculated to explain and confirm their catalytic property.

4.1 ORR mechanisms on nitrogen doped graphene as catalyst of fuel cells (With permission from (L. P. Zhang, Z. H.Xia; J. Phys. Chem. C 2011, 115, 11170). Copyright (2011) American Chemical Society)

4.1.1 Models and method

Two different nitrogen-containing graphene sheets ($C_{45}NH_{20}$ and $C_{45}NH_{18}$) were built, containing pyridinic and pyrrolic species, respectively, as shown in Figure 4-1(a-b). For comparison, graphene sheets with the same configuration but no N-doping ($C_{46}H_{20}$, $C_{46}H_{18}$) were also constructed, as shown in Figure 4-1(c-d). Carbon or nitrogen atoms on the edge of the graphene are terminated by hydrogen atoms.

(a)

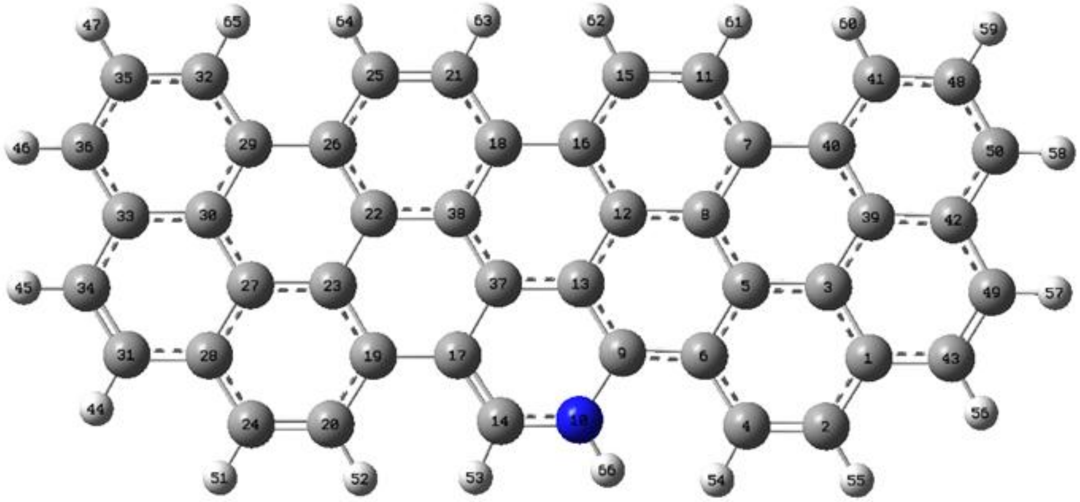
47 65 64 63 62 61 60 59
35 32 25 21 15 11 41 48
46 36 29 26 18 16 7 40 50 58
33 30 22 38 12 8 39 42
45 34 27 23 37 13 5 3 49 57
31 28 19 17 9 6 1 43
44 24 20 14 10 4 2 56
51 52 53 66 54 55

(b)

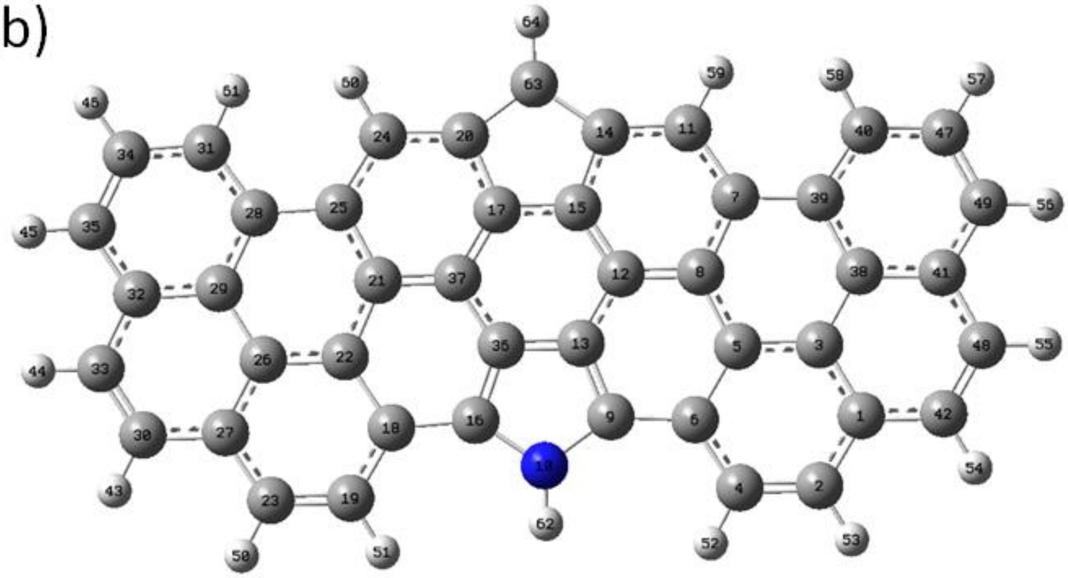
64
45 61 60 63 59 58 57
34 31 24 20 14 11 40 47
45 35 28 25 17 15 7 39 49 56
32 29 21 37 12 8 38 41
44 33 26 22 36 13 5 3 48 55
30 27 18 16 9 6 1 42
43 23 19 10 4 2 54
50 51 62 52 53

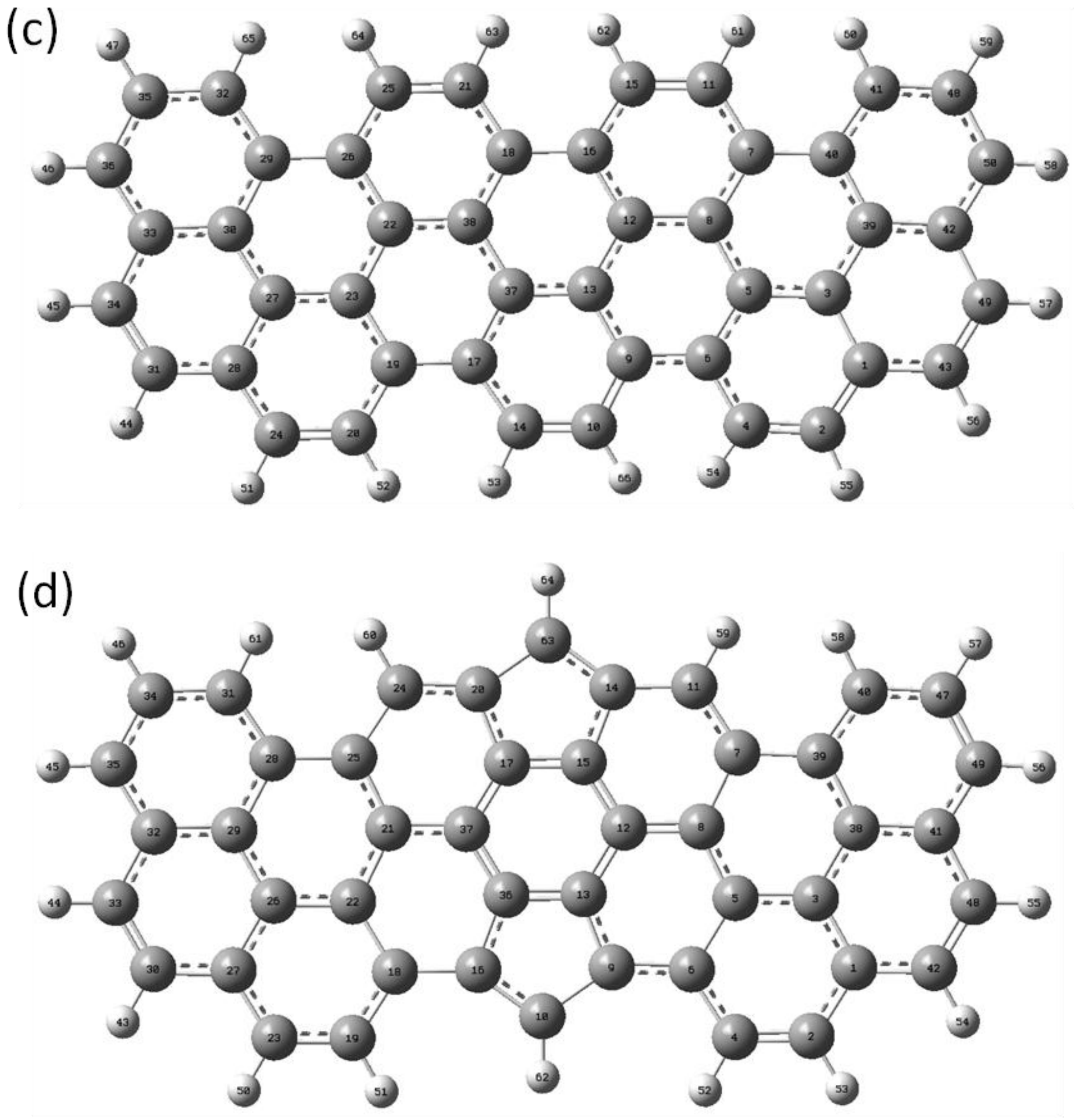

Figure 4-1 Nitrogen-containing graphene and corresponding no nitrogen-containing graphene sheets of (a) $C_{45}NH_{20}$, and $C_{45}NH_{18}$, (c) $C_{46}H_{20}$, and (d) $C_{46}H_{18,}$ the larger gray circles are carbon atoms, the larger blue circle is nitrogen atom, and the smaller light white circles are hydrogen atoms, all the atoms are numbered showing on circles.

In an acidic environment, a unified mechanism for the first reduction step, which omb D mj ov ’ p o o p p o f l o du o p d Y g ’ d o v m o p o of O_2, is summarizes as follows:

Path I:

$$O_2 + H^+ \rightarrow OOH^+ \quad (4\text{-}1)$$

$$OOH^+ + * + e^- \rightarrow *OOH \quad (4\text{-}2)$$

or Path II:

$$O_2 + * + e^- \rightarrow *O\text{-}O^- \quad (4\text{-}3)$$

$$*O\text{-}O^- + H^+ \rightarrow *OOH \quad (4\text{-}4)$$

where the asterisk represents a chemisorption site on graphene. In Path one, O_2 first reacts with a proton to form OOH^+ [169] and then adsorb on active sites of graphene after the first electron transmission was completed. In Path two, O_2 first adsorbs on the active sites of graphene with negative charge, then reaction with one H^+ forming adsorption OOH. No matter which mechanism, after the first electron transfer, the final products are both adsorption OOH on graphene. During our simulation process, the product OOH was placed near the N-graphene with OOH molecular plane parallel to the N-graphene plane, with a distance of 3.0 Å away from the graphene. The initial position of OOH was set over every carbon atom, in order to check whether it could adsorb on the nearby carbon atom or not. Four-electron transformation reactions were simulated by keeping introducing H atoms into the system. The introducing H atom was set near to the adsorbed OOH molecule from different directions, which would result in different sub-reaction path. At each step, the optimization structure was obtained, and adsorption energy for these molecules on the N-graphene was calculated. The adsorption energy is defined as the energy difference between the adsorption and the isolated systems. Here, the energy of the isolated system refers to sum of energies of fore-step adsorbed N-graphene and the individual isolated adsorbate molecules. Thus, negative adsorption energy indicates that the adsorbate molecule would be energetically favorable to be adducted to the surface of the N-garaphene.

4.1.2 Results and discussion

We first consider ORR behavior of the N-graphene with pyridinic structure (Figure 4-1a). Figure 4-2 shows the structural change of N-graphene $C_{45}NH_{20}$ and adsorbed molecules for each reaction step, at which an H atom was sequentially introduced into the system. The variation of distance between different atoms or molecules is listed in Table 4-1.

In the first step of the reaction, OOH moves from initial position (Figure 4-2 (a)) to the graphene and adsorbs to a carbon atom (C37) close to the nitrogen atom (Figure 4-2 (b)). The carbon atom (C37) moves out of the N-graphene plane to form a tetrahedral structure, suggesting that chemical bond is formed between the carbon and oxygen atoms. The distance between the carbon (C37) and oxygen (O67) atoms reduces to 1.50 Å from more than 3.0 Å, further confirming the formation of a chemical bond beween OOH and graphene. This is an important step for N-graphene to have catalytical activities since adsorption and formation of chemical bond is necessary for the following reactions.

Similar procedure was used to examine the adsorption of OOH on the graphene sheet with pyrrolic species and those with no doping. OOH molecule can also adsorb to a carbon atom (C16) close to the nitrogen atom but it cannot adsorb on the pure graphene sheet. Since the OOH adsorption is a must step for promoting ORR, pure graphene sheets do not possess catalytical capability for fuel cell.

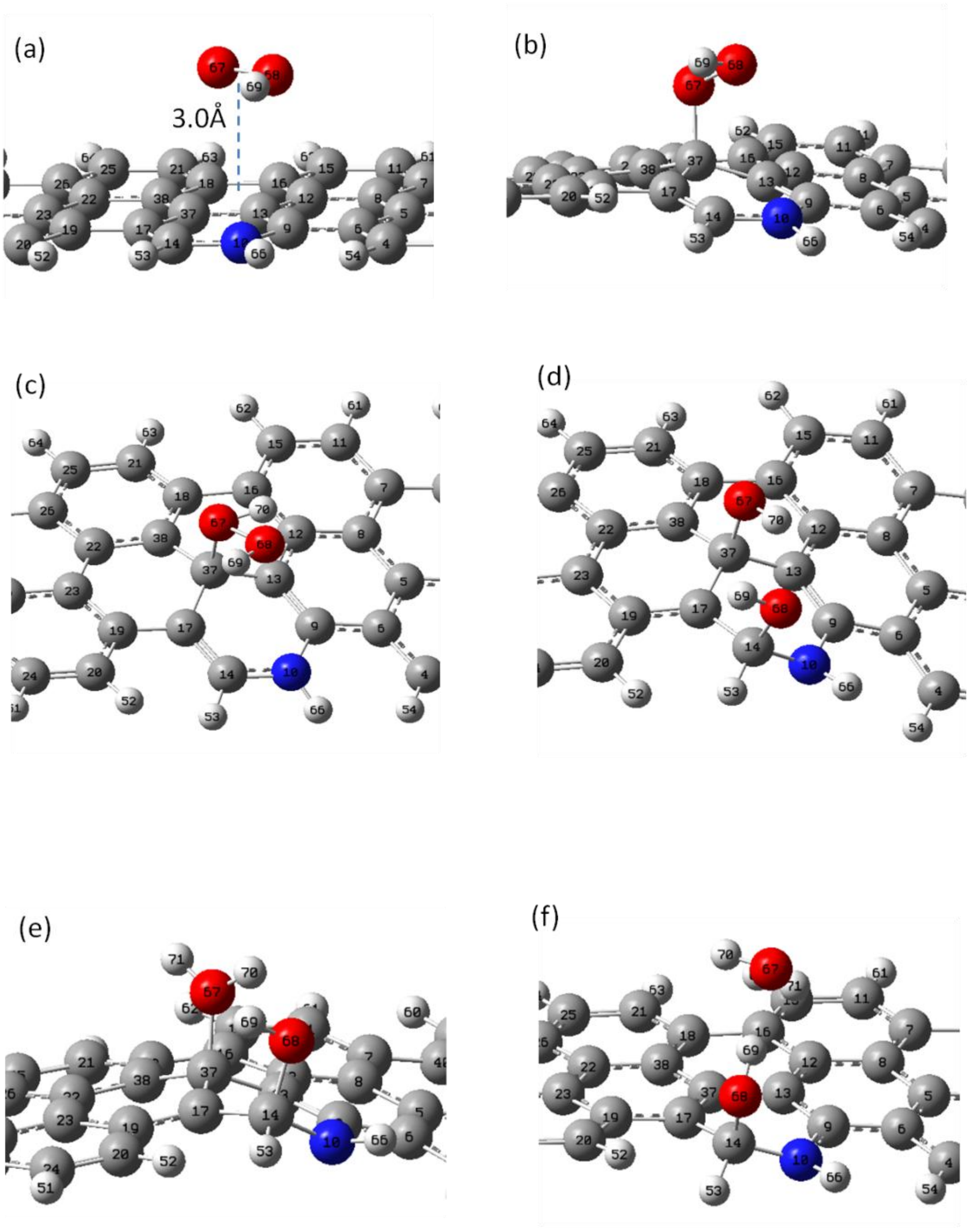
(a)
3.0Å
(b)
(c)
(d)
(e)
(f)

(g)

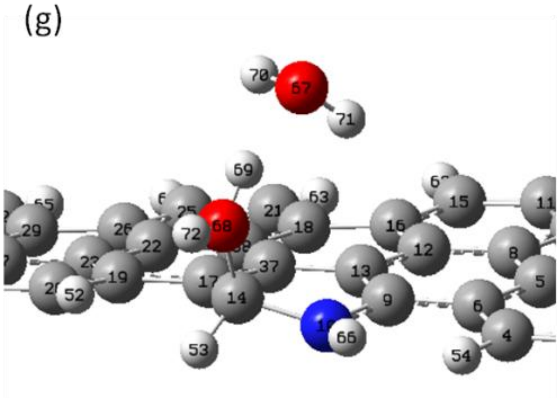

70
67
71
69
63
25
21
29
26
72
68
18
16
15
11
22
37
12
8
23
19
17
13
5
52
14
9
6
66
53
54
4

(h)

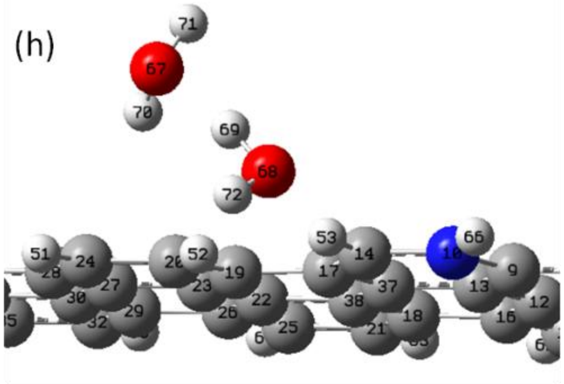

71
67
70
69
68
72
53
66
51
24
52
14
10
28
19
17
9
30
27
23
37
13
22
38
12
29
26
18
16
25
21

(c’)

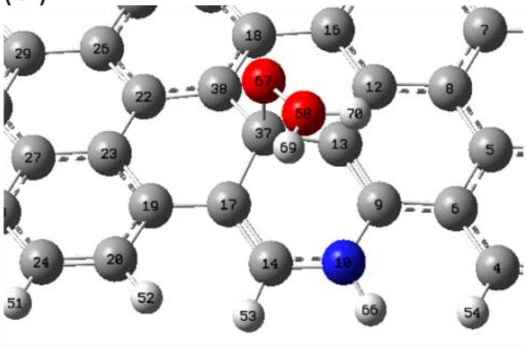

18
15
29
25
7
38
67
12
8
22
68
70
37
69
13
5
27
23
19
17
9
6
24
20
14
10
4
51
52
53
66
54

(d’)

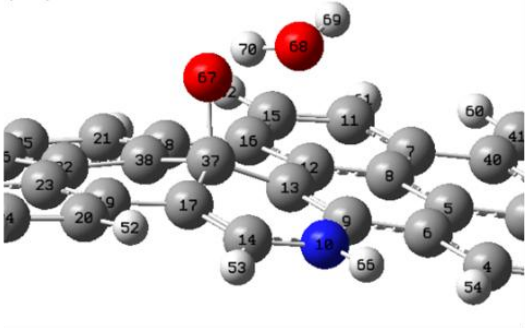

69
70
68
67
15
11
60
21
16
7
38
37
40
12
8
23
13
20
17
9
5
52
6
14
10
4
53
65
54

(e’)

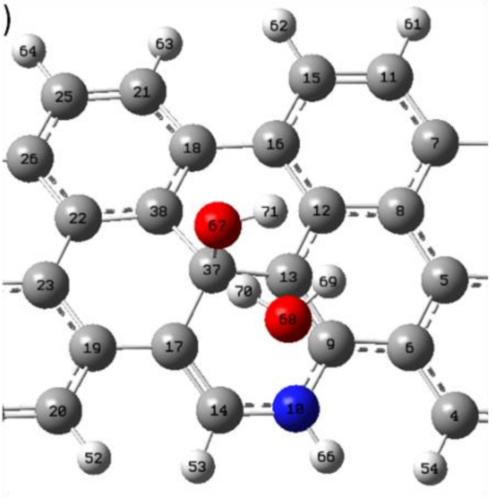

64
63
62
61
25
21
15
11
26
18
16
7
22
38
67
71
12
8
37
13
69
23
70
68
5
19
17
9
6
20
14
10
4
52
53
66
54

(f’)

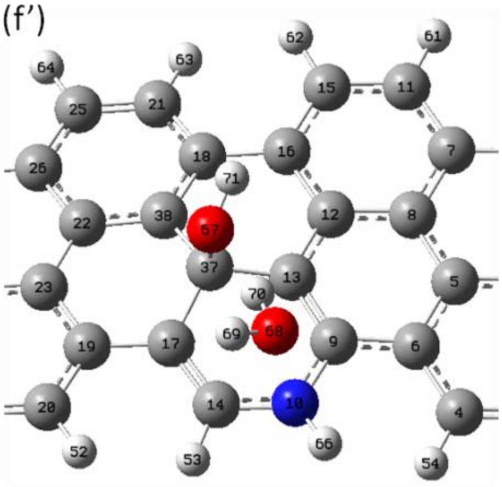

64
63
62
61
25
21
15
11
26
18
16
7
71
22
38
67
12
8
37
13
5
23
70
69
68
19
17
9
6
20
14
10
4
52
53
66
54

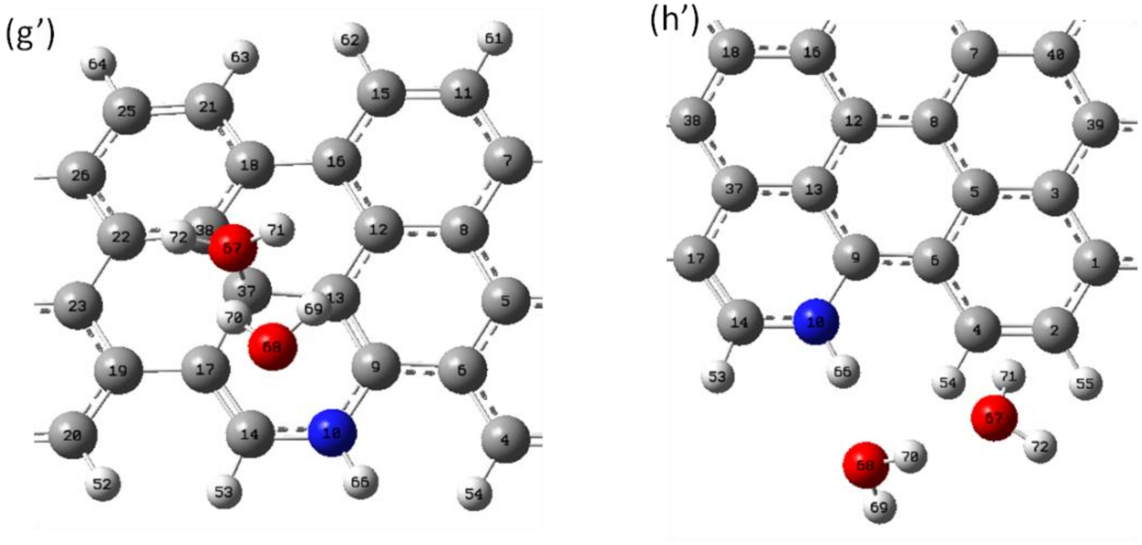

Figure 4-2 I l ( ), ( ), ( ), (g), (’), (’), d (g’) d f l op m z o u u (b), (d), (f), ( ) , (d’), (f’), d (’) of y m fo o p, showing only part of the graphene, with the larger gray circles for carbon atoms, the larger blue circles for nitrogen atoms, the larger red circles for oxygen atoms, and the smaller light gray circles for hydrogen atoms.

Table 4-1 Variation of distance between different atoms during each reaction step for two different reaction paths (Unit/Å)

		Step 1	Step 2	Step 3	Step 4
Reaction Path I	D(O-O)	1.45	2.89	2.83	2.81
	D(1-G)	1.50	1.47	>3.30	>3.30
	D(2-G)	>2.40	1.46	1.42	>3.20
Reaction Path II	D(O-O)	1.45	2.73	2.91	2.76
	D(1-G)	1.50	1.41	1.49	>3.20
	D(2-G)	>2.40	>3.30	>3.30	>2.80

Note: D(O-O), the distance between two oxygen atoms; D(1-G), the nearest distance between O67 and the graphene; D(2-G), the nearest distance between O68 and the graphene.

After the OOH adsorbs on the N-graphene, we introduce another H to the system. Because of random nature, this H atom may first move to the position near the oxygen atom (O67) that is bonded to the carbon atom, or the other one. In the former case, the subsequent reaction process is noted as Reaction Path I while in the latter case, it is Reaction Path II. We first consider the former case. In the simulation, the H atom is placed near the oxygen atom O67 within a distance of O-H bonding length, as shown in Figure 4-2 (c). In such step, HOO*H molecule is assumed to form and adsorb to the N-graphene. After optimization, we found that one of the oxygen atoms still bonds to the graphene at C37 in the form of OH while the other one with a hydrogen drifts away and adsorbs to another carbon atom (C14) adjacent to the nitrogen (Figure 4-2 (d)). The distance between two O atoms now increases to 2.89 Å, indicating that the bond of O-O is broken. Thus the HOO*H is not a stable product. When an H is introduced into the system near the OOH, it leads to the decomposition of HOO*H into two OH molecules. Similar reaction is also observed on the graphene sheet with pyrrolic species. This is an important step because the break of O-O bonds represents four-electron transformation pathway in ORR. Otherwise, it is two-electron transformation pathway. Obviously, the ORR on N-graphene is four-electron transformation pathway, which is consistent with the experimental results [170].

We further add the second H to the system near the oxygen (O67) that first bonds to the graphene (Figure 4-2 (e)). The introduction of the H atom causes the break of C-O bond (C37-O67 bond) and the formation of the first water molecule. The distance between O67 and C37 now increases from 1.47 Å to 3.30Å. At the same time, another adsorbed OH molecule is stretched by the newly formed water molecule and a hydrogen bond is formed between the hydrogen in adsorbed OH (H69) and the oxygen in the water molecule (O67). As the third H is introduced into the system, the second water molecule is formed as shown in Figure 4-2 (h). After the two water molecules drift away from the N-graphene, the N-graphene recovers to its initial state. These reactions also occur on the graphene sheet with pyrrolic species. Hereto, four-electron transformation process finishes and the N-graphene is ready for the next catalytic reaction cycle.

For the case that the first introduced H is close to the oxygen atom (O68) that is bonded to another H atom, four-electron transformation also occurs but the sub-reaction paths are different, as shown in Figure 4- (’)-(’). Instead of producing two OH molecules after the first H is introduced, one water molecule is generated while the oxygen atom (O67) alone adsorbs on the graphene. Consequently, when the next two H atoms were added near the oxygen (O67), another water molecule is generated. With the analysis above, the reactions of the electron transformation of ORR on the N-graphene are as follows:

Reaction Path I,

$$OOH \rightarrow {}^*OOH \qquad (4\text{-}5)$$

$$^*OOH + e^- + H^+ \rightarrow {}^*OH + {}^*OH \qquad (4\text{-}6)$$

$$^*OH \text{ (adsorbed 1)} + e^- + H^+ \rightarrow H_2O \qquad (4\text{-}7)$$

$$^*OH \text{ (adsorbed 2)} + e^- + H^+ \rightarrow H_2O \qquad (4\text{-}8)$$

or after Reaction (1), it changes to Path II,

$$^*OOH + e^- + H^+ \rightarrow {}^*O + H_2O \qquad (4\text{-}6a)$$

$$*O + e^- + H^+ \rightarrow OH \qquad (4\text{-}7a)$$

$$*OH + e^- + H^+ \rightarrow H_2O \qquad (4\text{-}8a)$$

where asterisk * represent the graphene. Our simulation began with the reaction (4-5). Reactions (4-7) and (4-8) are the same reaction, but *OH adsorbed to C37 on the N-graphene in reaction (4-7), and in Reaction (4-8) *OH adsorbed to C14.

Adsorption energies of the each step are calculated and the relative energy of reaction pathway is shown in Figure 4-3. In the figure, for the first step, the reference energy state is the total energy of optimized N-graphene and OOH molecules. For the other reduction steps, the reference energy states is the total energy of the products of previous reaction step and $H^+ + e^-$, based on which the relative energy of each reaction step was calculated. The solid lines show the energy variation of Reaction Path I, and the dot lines refer to that of Reaction Path II. In the first step of the reaction in this simulation, the energy decreases by 0.85eV when OOH adsorbs to the N-graphene. When H atom was subsequently introduced into the system, the adsorption energies for the following reaction steps of Reaction Path I are -4.28eV, -5.01eV and -2.48eV, respectively. For Reaction Path II, the adsorption energies for the following reaction step are -3.53eV, -4.66eV and -3.77eV. For the second reaction step, the decreasing energy of Reaction Path I is more than that of Reaction Path II, suggesting that the reaction favorites the production of two OH molecules when the bond of O-O is broken. In each step of electron transformation, the energy becomes more negative, driving the system to a more stable state. Therefore, the four-electron reaction can spontaneously take place on the nitrogen-doped graphene.

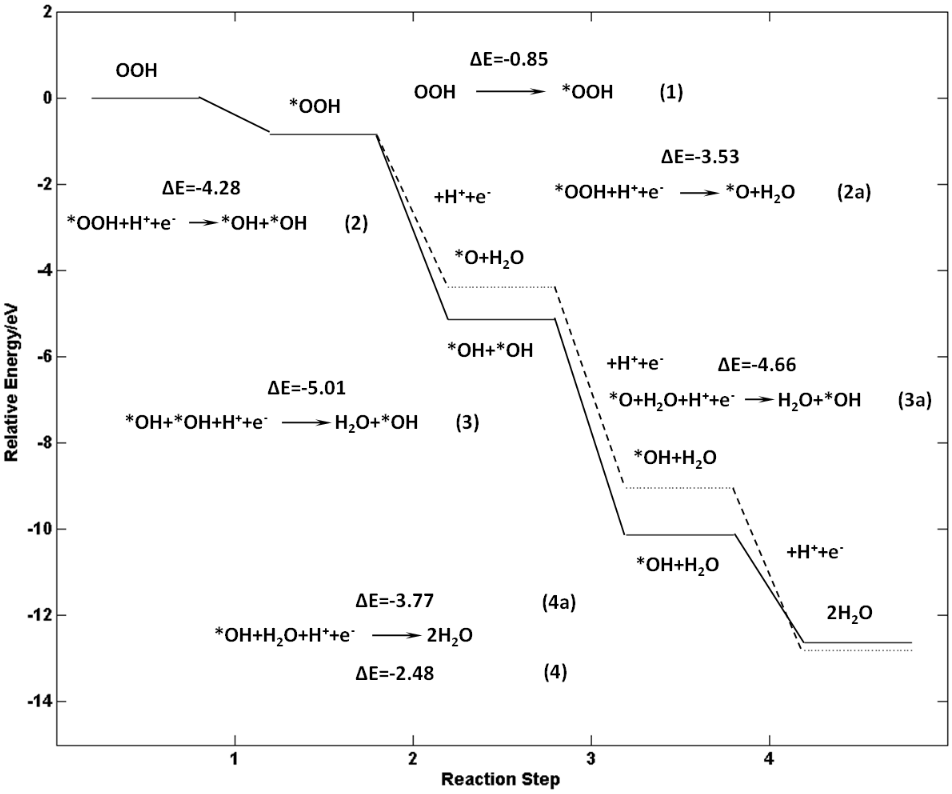

Figure 4-3 The relative energy of two different reaction pathways of the ORR on N-graphene ($C_{45}NH_{20}$). For the first step, the reference energy state is the total energy of optimized N-graphene ($C_{45}NH_{20}$) and OOH molecules, and for the other reaction steps, the reference energy states are the total energy of the product of previous reaction and H^+ + e^-.

Why does the doped graphene has catalytic capability but pure graphene not? This could be explained from the level of their chemical reactivity. The highest occupied molecular orbital (HOMO)-lowest unoccupied molecular orbital (LUMO) energy separation has been used as a simple indicator of kinetic stability. A small HOMO-LUMO gap implies low kinetic stability and high chemical reactivity, because it is energetically favorable to add electrons to a high-lying LUMO, to extract electrons from a low-lying HOMO, and so to form the activated complex of any potential reaction [171]. We have calculated the HOMO-LUMO gap for all those graphene sheets with or without nitrogen doping (Table 4-2). For pure graphene, $C_{46}H_{20}$, the gap is 2.7eV, which agrees with the results for similar size graphene, calculated by Philip Shemella [172]. The HOMO-LUMO gap reduces by two times after a nitrogen atom is substituted into $C_{46}H_{20}$ to form $C_{45}NH_{20}$, which is also consistent with results from Zheng *et al.*[169]. Hence, the chemical reactivity of the nitrogen doped graphene is significantly improved because the electrons are easier excited from valence band to conduction band. For pure graphene $C_{46}H_{18}$, the HOMO-LUMO gap is already low due to the present of defects (two pentagon carbon rings). It has been shown that defects can significantly alter the electronic properties of the graphene. Surprisingly, although $C_{46}H_{18}$ has a low HOMO-LUMO gap, our further calculations show that OOH molecule cannot adsorb to the pure graphene, indicating that it does not have catalytic capability. Obviously, there are other factors that determine the catalytic capability of the graphene, e.g. spin density and charge density of individual atoms, which will be discussed later. Although the nitrogen doping makes the HOMO-LUMO gap of $C_{45}NH_{18}$ slightly increase, the value of the gap (1.47 eV) is still comparable to that of the graphene containing pyridinic species. Thus, nitrogen doping is a key for graphene to possess high catalytic reactivity.

Table 4-2 HOMO, LUMO and HOMO-LUMO gy g p of α l o d β l o for $C_{45}NH_{20}$, $C_{45}NH_{18}$, $C_{46}H_{20}$ and $C_{46}H_{20}$ (Unit/eV)

	$C_{45}NH_{20}$		$C_{45}NH_{18}$		$C_{46}H_{20}$		$C_{46}H_{18}$	
	α electron	β electron	α electron	β electron	α electron	β electron	α electron	β electron
HOMO	-3.29	-4.87	-4.57	-4.58	-4.87	-4.87	-4.61	-4.61
LUMO	-1.89	-2.14	-1.98	-3.11	-2.10	-2.10	-3.43	-3.43
HOMO-LUMO gap	1.40	2.73	2.59	1.47	2.77	2.77	1.18	1.18

Note: HOMO-LUMO gap is the difference between LUMO and HOMO energy levels

It is of interest to determine the active sites for catalytic reaction on N-graphene. Figure 4-4 (a) and (b) show atomic charge and spin density distribution on the N-graphene ($C_{45}NH_{20}$), the atomic charge and spin density distribute non-uniformly around the nitrogen atom. The carbon atom (C6), the second neighbor of the nitrogen, has the largest atomic charge value 0.169 while the carbon atom C9 bonding to the nitrogen has the second largest value 0.150. C37 in the opposite position of the same hexagon ring as the nitrogen has the largest spin density 0.235 while C9 has the second largest spin density 0.194. Putting OOH molecule over the carbon atoms in a distance of 3.0 Å, we have examined most carbon atoms that could possibly act as active sites for catalysis, and found that OOH only adsorbs to C37 and C9, the carbon atoms with high spin density. Thus, there are two active sites near single nitrogen dopant on the N-graphene ($C_{45}NH_{20}$). The adsorption energy of OOH bonding to C37 and C9 is equal to -0.85eV and -1.04eV, respectively. Although C6 has the largest atomic charge value, OOH molecule could not adsorb to this carbon atom as its spin density is -0.045. On the other hand, C37 has the small charge density of 0.084, but its spin density is the largest. OOH molecule can adsorb to this carbon atom.

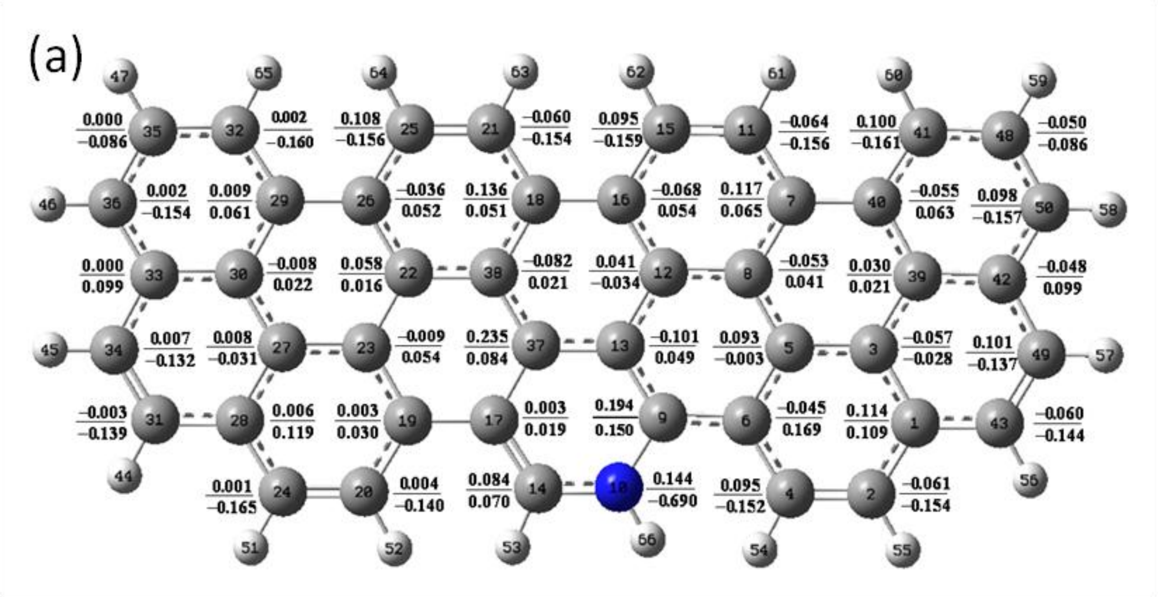
(a)
47
65
64
63
62
61
60
59
0.000 −0.086 35
32 0.002 −0.160
0.108 −0.156 25
21 −0.060 −0.154
0.095 −0.159 15
11 −0.064 −0.156
0.100 −0.161 41
48 −0.050 −0.086
46
36 0.002 −0.154
0.009 0.061 29
26 −0.036 0.052
0.136 0.051 18
16 −0.068 0.054
0.117 0.065 7
40 −0.055 0.063
0.098 −0.157 50
58
0.000 0.099 33
30 −0.008 0.022
0.058 0.016 22
38 −0.082 0.021
0.041 −0.034 12
8 −0.053 0.041
0.030 0.021 39
42 −0.048 0.099
45
34 0.007 −0.132
0.008 −0.031 27
23 −0.009 0.054
0.235 0.084 37
13 −0.101 0.049
0.093 −0.003 5
3 −0.057 −0.028
0.101 −0.137 49
57
−0.003 −0.139 31
28 0.006 0.119
0.003 0.030 19
17 0.003 0.019
0.194 0.150 9
6 −0.045 0.169
0.114 0.109 1
43 −0.060 −0.144
44
56
0.001 −0.165 24
20 0.004 −0.140
0.084 0.070 14
10 0.144 −0.690
0.095 −0.152 4
2 −0.061 −0.154
51
52
53
66
54
55

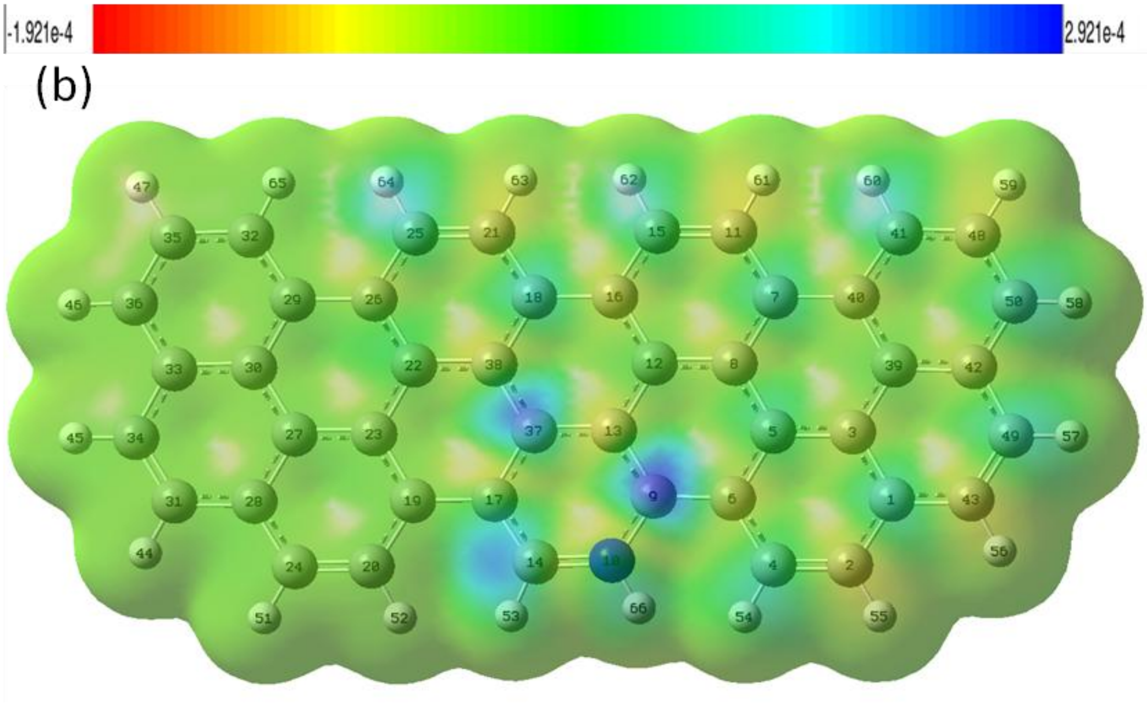
-1.921e-4
2.921e-4
(b)
47
65
64
63
62
61
60
59
35
32
25
21
15
11
41
48
46
36
29
26
18
16
7
40
50
58
33
30
22
38
12
8
39
42
45
34
27
23
37
13
5
3
49
57
31
28
19
17
9
6
1
43
44
56
24
20
14
10
4
2
51
52
53
66
54
55

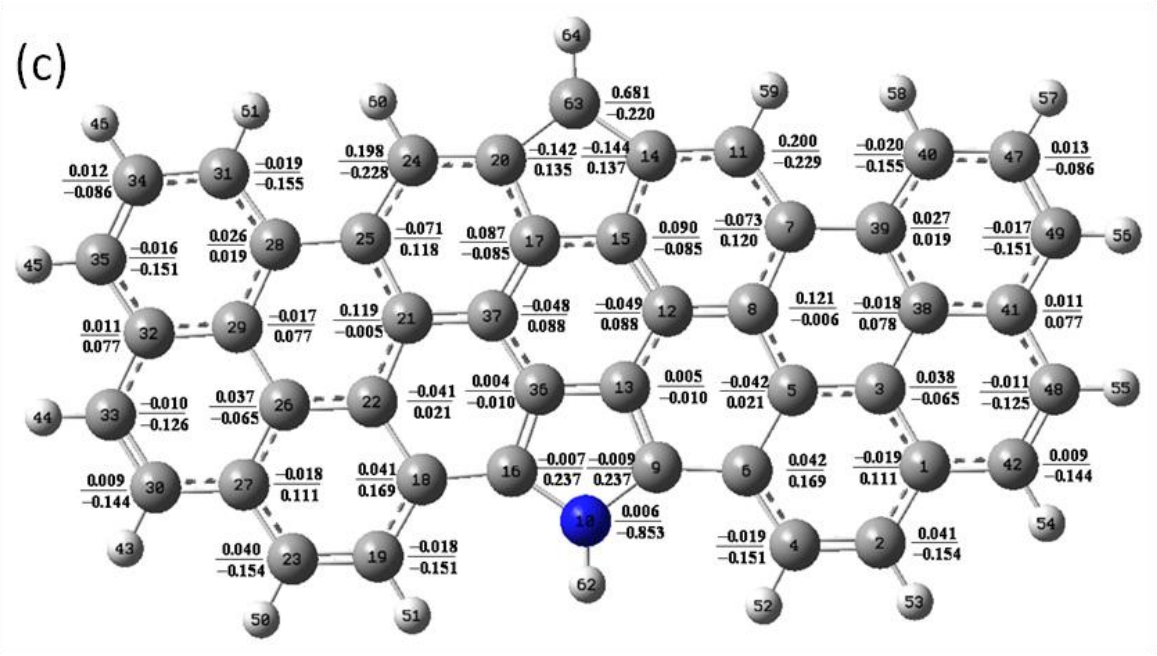
(c)

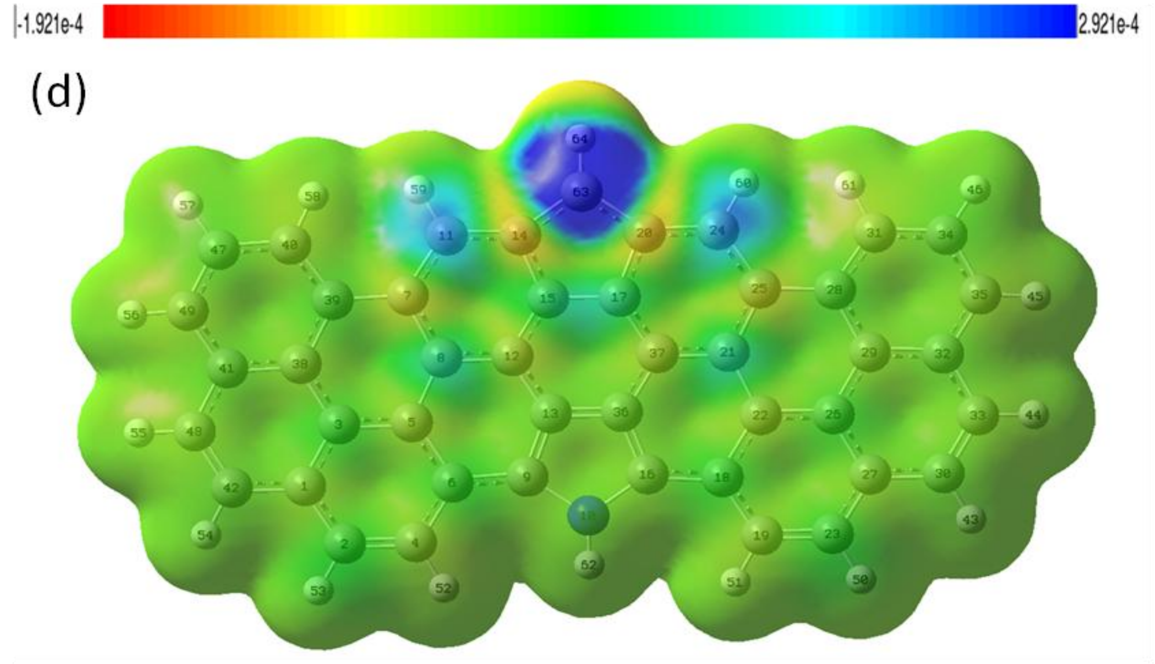
-1.921e-4
2.921e-4
(d)

Figure 4-4 (a), (c) Charge distribution, and (b), (d) spin density distribution on the N-graphene with pyridinic structure ($C_{45}NH_{20}$) and pyrrolic structure ($C_{45}NH_{18}$), respectively. The number on the circle is the number of atom. The fractions on the side of these atoms in (a), (c) are atomic charge value and spin density value on the atoms. The denominator is charge value and the numerator is spin density number. In (b), (d) spin density distributes on the electron density isovalue plane; the most negative value is red while the most positive value is blue.

Putting OOH molecule over the carbon atoms in a distance of 3.0 Å, we have examined most carbon atoms that could possibly act as active sites for catalysis. There is no active sites identified on pure graphene but we found that OOH can adsorb to C37 and C9, the carbon atoms with high spin density. Thus, there are two active sites near single nitrogen dopant on the N-graphene ($C_{45}NH_{20}$). The adsorption energy of OOH bonding to C37 and C9 is equal to -0.85eV and -1.04eV, respectively. Although C6 has the largest atomic charge value, OOH molecule could not adsorb to this carbon atom as its spin density is -0.045. On the other hand, C37 has the small charge density of 0.084, but its spin density is the largest. OOH molecule can adsorb to this carbon atom.

We also checked all of the possible active sites on the N-graphene with a pyrrolic structure ($C_{45}NH_{18}$). Its atomic charge density and spin density distribution are shown in Figure 4-4 (c) and (d), respectively. We found that OOH can adsorb to C63, C11, C24, C9 and C16 atoms. C63 has the largest spin density 0.681. C11 and C24 have the second and third largest spin density 0.200 and 0.198. Different from the $C_{45}NH_{20}$, the carbon atoms, C9 and C16, both with the largest atomic charge values 0.237 but negative spin densities of -0.009 and -0.007, respectively. OOH can be adsorbed to these two atoms, C9 and C16. This may be attributed to both facts: large charge density and relatively small absolute value of negative spin density of these two atoms. Thus, compared to atomic charge density, spin density is much more important in determining the catalytic active sites. If negative spin density on an atom is small, atomic charge density will play a key role in determining whether it is an active site or not. For N-graphene models, $C_{45}NH_{20}$ and $C_{45}NH_{18}$, containing pyridinic and pyrrolic structures, both have electrocatalytic property for ORR of four-electron transformation process, which consistent with the experimental results [170, 173]. Here, the substituting N atoms in N-graphene leads to the asymmetry spin density and atomic charge density, thus making it possible for N-graphene to show high electroncatalytic activities for the ORR.

More generally, any chemical species in the form of either substitution or attachment on graphene, which can lead to a high asymmetric spin density and atomic charge density on graphene, could promote high electroncatalytic activities for the ORR. Recently, Wang et al. demonstrated that poly (diallyldimethylammonium chloride) (PDDA) functionalized/adsorbed carbon nanotubes can act as effective catalysts for ORR in fuel cells with similar performance as Pt catalysts [174]. With a strong electron-withdrawing ability, PDDA could cause high positive spin density and atomic charge density on nanotubes, creating active sites for facilitating ORR. Thus, our results here may provide a general rule for searching for new catalysts for ORR in fuel cells.

4.2 Effect of microstructure of nitrogen-doped graphene on oxygen reduction acticity (With permission from (L. P. Zhang, J. B. Niu, L. M. Dai, Z. H. Xia; Langmuir 2012, 28, 7542) Copyring (2012) American Chemical Society).

It is believed that the superior catalytic capabilities of these N-doped carbon materials are directly related to their unique nanostructure. Among the nitrogen-doped structures, pyrrolic and pyridinic nitrogen was reported to play an important role in the enhanced ORR activity in alkaline [175-178] and acidic [179, 180] solutions. Stone-Wales defects have been predicted to alter the electronic properties (band structure and density of states) of graphene [181-183], and in so modify its chemical reactivity toward adsorbates, and likely impact upon its catalytic properties. Although some theoretical work has been done on ORR pathway on N-doped graphene [184-186], the role of materials structures, including N distribution and defects, played in ORR, remains unclear. Understanding how microstructure influences the catalytic behavior of the graphene will guide design and optimization of the electrocatalytic electrodes, and discovery of new catalysts. In this section, we demonstrate that the ORR activities are directly correlated to material microstructure. The active catalytic sites are more likely to locate at the area with higher positive charge density and/or positive spin density. The number of dopants in cluster and Stone-Wales defects strongly affects the ORR on the N-doped graphene. This work motivates a direction for design of carbon nanostructured materials to improve their catalytic efficiency, and provides a theoretical framework for analysis of catalytic properties versus material structures.

4.2.1 Methods

Nitrogen atoms were incorporated into the armchair edge of the graphene to form pyridinic or pyrronic or mixed structures. Stone-Wales dislocations were also generated on the graphene. Stone-Wales defects are one of the important topological defects in sp^2-bonded carbon materials, playing a central role in the formation, transformation of carbon nanostructures. We simulated the ORR processes starting with the first electron transformation, the method is the same as described in section 4.1.1. In this step, we set OOH or O_2 near the graphene plane at a distance of 3 Å, as schematically shown in Fig.4-5(a). The optimized structures for OOH^+ or O_2 adsorption (ads) to graphene were obtained through structural optimization calculations. It is well-known that overall ORR can proceed by a two-step two-electron pathway with the formation of hydrogen peroxide or by a more efficient four-electron process to combine oxygen with electrons and protons directly in water. Hence, the ORR on graphene could follow either two-electron pathway or four-electron process, which will be examined in the simulation of subsequent electron transforming reactions. The succeeding electron transforming reactions were simulated by keeping adding H atoms in the system. For each step, we obtained the optimized structure, and calculated the adsorption energy (bond strength) for those molecules on the nitrogen-doped graphene. The reversible potential of each reaction step on the nitrogen doped graphene was also calculated following the procedure described by Roques and Anderson [187]. For an electrochemical reaction with reactants Ox and products Red:

$$\mathrm{Ox} + e^- (U^0) \rightarrow \mathrm{Red}, \tag{4-9}$$

the relationship between the Gibbs free energy for a reduction reaction in aqueous (aq) solution and the reversible potential, U^0 is [187]

$$U^0 = \Delta G^0 / nF \tag{4-10}$$

where ΔG^0 is the Gibbs free energy change of Eq. (4-9), n is the number of electrons involved in the reaction, and F is the Faraday constant. In this work, the Gibbs energy change is replaced by the reaction energy, E_r^0, plus constants [187]. So, Eq.(4-10) becomes

$$U^0 = E_r^0 / nF + U_1 + U_2 \tag{4-11}$$

where the first constant U_1 represents $P\Delta V$ and $T\Delta S$ energy contributions, which depends on the solvation model used for the reactants and the products [187]. The second constant (U_2 = -4.6V) comes from the fact that the energy of an electron at 0 V on the electrochemical scale is -4.6 eV on the physical (vacuum) scale [187], which is the one in which the quantum calculations take place. Eq. (4-11) is the reversible potential in aqueous solution. For the reaction on a catalyst surface,

$$\text{(catalyst)-Ox} + e^- \,(U) \rightarrow (\quad \text{l y} \quad)\text{-Red} \tag{4-12}$$

the reversible potential U can be extrapolated from Eq. (4-11) assuming the constants U_1+U_2 unchanged:

$$U = U^0 + (E_r - E_r^0) / nF \tag{4-13}$$

The change in reaction energy between Eq. (4-9) and Eq. (4-12), ΔE_r, is equal to the total adsorption energy of the reactants E_{ads} (Ox), minus the total adsorption energy of the products E_{ads} (Red) [188, 189]:

$$\begin{aligned}\Delta E_r &= E_r - E_r^0 \\ &= E_{(ads)}[Ox] - E_{(ads)}[\mathrm{Re}d]\end{aligned} \tag{4-14}$$

So, the reversible potential on catalyst surface U is a function of adsorption energy and standard reversible reduction potentials U^0, for the reactions in bulk solutions [188, 175]:

$$U = U^0 + \Delta E_\mathrm{r} / n\mathrm{F} \tag{4-15}$$

where U^0 is the standard solution-phase potential. Thus, if we know the reversible potential in an aqueous solution of a redox reaction U^0 (from experimental or theoretical investigations), we will be able to calculate the reversible potential on a specific catalyst surface U just by the knowledge of the adsorption energies of each species involved in the reaction.

It should be noticed that in the ORR we study here, OOH^+ and H^+ exist in aqueous solution but the total adsorption energy of the chemical species are calculated using OOH, and H. This is reasonable because the effect of charge has been considered by using the known reversible potential in an aqueous solution of a redox reaction U^0. The predictions are very close to the experimental results [187-189]. Nevertheless, care should be taken when using this method to calculate the reversible potentials. For example, the coverage rate of OH (ads) and OOH (ads) on graphene may be considered in order to get more accurate results, in particular, when comparison is made between different pathways and concerning the existence of species like OOH in solution (and not near the surface) or OH in solution.

4.2.2 Results and discussion

We first studied catalytic pathways of graphene with two nitrogen atoms incorporated into the hexagon and the pentagon of the graphitic sheet with two combined Stone-Wales defects, as shown in Figure 4-5. Such structures are pyridinic and pyrrolic mixed type of nitrogen atoms in the nitrogen-doped graphene. As mentioned above, there are two possible reaction pathways in the first electron transfer: i) intermediate molecule OOH^+ adsorption, and ii) direct O_2 adsorption. We first simulated the ORR processes beginning with the first electron transformation in an acidic environment, in which process an intermediate molecule OOH^+ has been formed. Simulation shows that the both OOH^+ and OOH molecule far from the graphene (~3 Å) can adsorb on the graphene at carbon atom #16, as shown Figure 4-5(b). This result indicates that there is no energy b o. Af dopo, g p pl d o d o“ ddl p ” warped surface while the carbon atom attached to the oxygen raises out of the plane to form a tetrahedral structure.

The O_2 adsorption on the N-doped graphene was simulated with the same procedure as OOH adsorption. O_2 cannot adsorb on the graphene at carbon atom #16, even when O_2 molecule is put in the range of bonding formation. However, O_2 can adsorb on the same site of the negatively charged graphene. The adsorbed O_2 can further interact with an H^+ to form an adsorbed OOH. Therefore, the surface charge promotes the adsorption of O_2. However, the O_2 adsorption energy is -0.7eV, over 10 times smaller than that for OOH^+ adsorption (-11.26 eV). This implies that OOH^+ adsorption is a more favorable reaction in the first electron transfer. (//need read carefully and check the data in case questioned//) (I think this is correct. We tested on C atom #16)

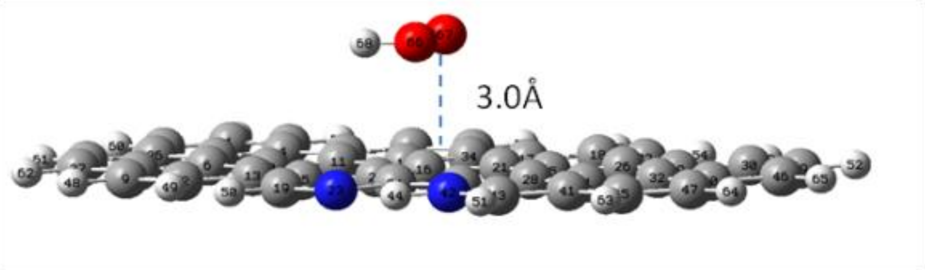
3.0Å

(a)

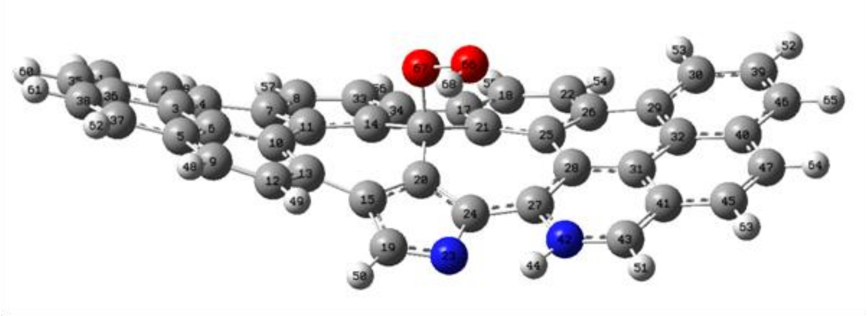
67
69
68
57
55
54
53
52
65
64
63
60
61
62
48
49
50
44
51
22
42

(b)

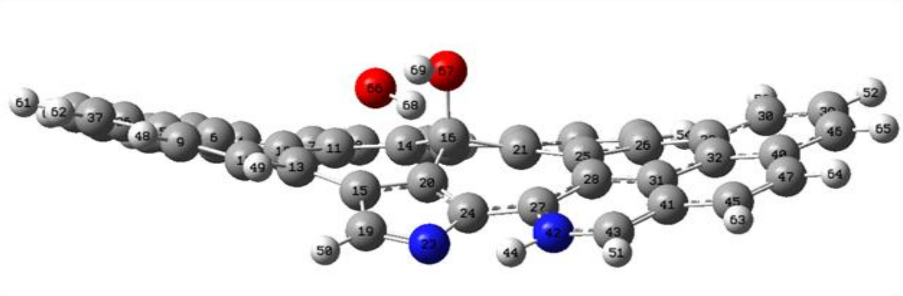
66
69
67
68
61
62
52
65
64
63
49
50
44
51
22
42

(c)

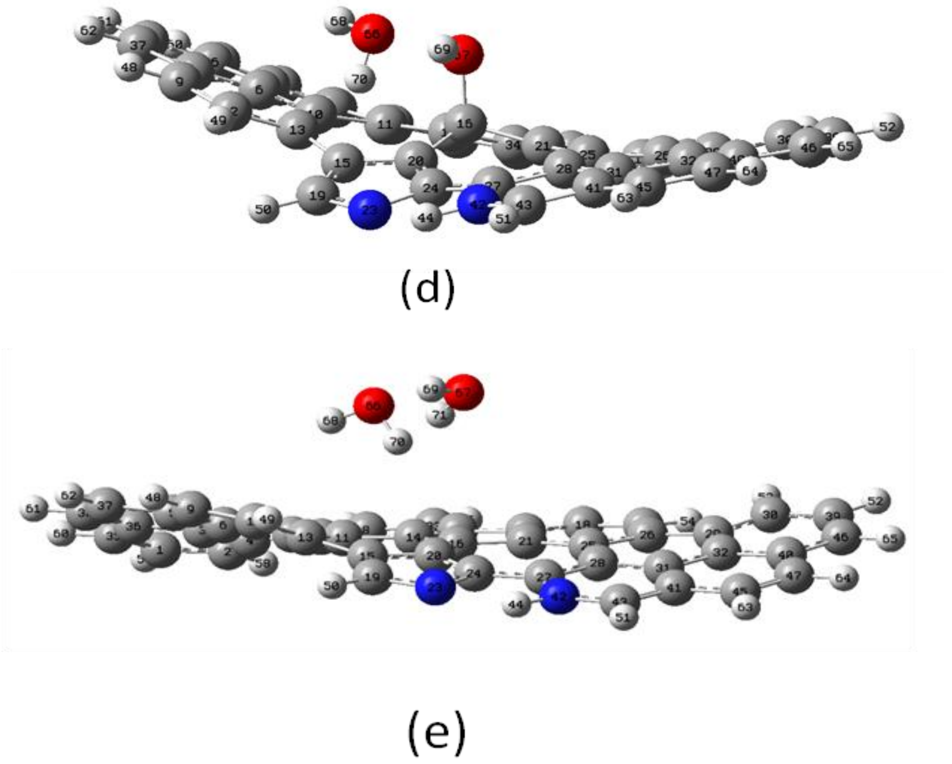

Figure 4-5 Optimized structure of each electron transformation in oxygen reduction reaction: (a) Initial position of OOH from nitrogen doped graphene, (b) OOH adsorbs on the graphene, (c) O-O bond is broken, (d) One water molecule is generated, and (e) C-O bond is broken, the second water molecule is generated. Grey, blue, red and small white balls represent carbon, nitrogen, oxygen and hydrogen atoms, respectively.

When adding an H atom near the oxygen atom that attaches to the graphene, a bond is formed between the oxygen and the hydrogen atoms. At the same time, the O-O bond is broken, resulting in the formation of a hydroxide molecule OH, as shown in Figure 4-5(c). During this process, the distance between the two O atoms changed from an initial value of 1.45 Å to a value of 2.72 Å. The dissociated OH moves away from the graphene plane, while the other dissociated OH is still bonding to the graphene. This is a typical four electron reaction because the O-O bond breaks during the reaction [190, 191]. After adding two more H atoms to the O atoms in the reaction system, two water molecules are formed and completely departed from the graphene (Figure 4-5 (d), and (e)). The third and fourth electrons were then transformed in the oxygen reduction reaction. Finally, after removal of water molecules, the "saddle-shaped" graphene recovers to its original shape and is ready for next reaction cycle.

The above chemical reactions, adsorption energy difference between reactants and products, standard reversible potential and reversible potential on the catalyst surface are listed in Table 4-3. For each step of electron transformation, the reversible potential is positive, suggesting that the system moves to a more stable state during the reactions. So, the four electron reaction can spontaneously take place on this nitrogen-doped graphene. Of all the reaction steps, OOH molecular adsorption on the graphene (Reaction 1) is one of the most important steps for the catalytic reaction of oxygen reduction because it determine whether a nitrogen-doped graphene electrode has catalytic activity or not. The O-O bond break in Reaction (2) is another key necessary step for the four electron reaction. The reversible potential for overall ORR is U_s^0 = 1.228 V(SHE), which is consistent with standard reversible potential of ORR [192, 193]. It should be noted that during the ORR process, Carbon #16 is not the only one active site for the ORR. We found that OOH molecule is also able to adsorb to Carbon #22 and #24 and the succeeding reactions can occur spontaneously.

Table 4-3 Adsorption energy difference and reversible potentials of each ORR step on the graphene with two doped nitrogen atoms and two Stone-Wales defects.

Reaction order	Chemical Reaction	Adsorption energy difference ΔE_r (eV)	Reversible potential U^0 (V/SHE) †	Reversible potential U (V/SHE)
1	$O_2+H^++e^-\rightarrow{}^*OOH$	1.170	-0.046	1.120
2	$^*OOH+H^++e^-\rightarrow{}^*OH+OH$	1.150	-0.664	0.480
3	$OH+H^++e^-\rightarrow H_2O$	0.0	2.813	2.813
4	$^*OH+H^++e^-\rightarrow H_2O$	-2.320	2.813	0.493
Overall	$O_2+4H^++4e^-\rightarrow H_2O$	0.00	1.229	1.228

† Ref.170.

From quantum mechanics, the nitrogen doping creates an electron acceptor state in the conduction band near the Fermi level [194, 195]. The electron-accepting ability of the nitrogen atom creates net positive charge on adjacent carbon atoms in the graphene plane, resulting in redistribution of spin density and charge density around the nitrogen atoms, which will influence the OOH adsorption and further O-O bond breakage. It was shown that the adsorption bond strengths of adsorbate radicals, H and OOH, exhibit a correlation with the spin density [196]. So, spin density may be regarded as a factor determining positional selectivity of radical adsorption while charge density determines the attractive force between charged atoms. It is expected that the active catalytic sites for OOH adsorption should be those atoms with high spin density and/or high positive charge. We have calculated the spin density and charge density for a given N-doped structure. Figure 4-6 shows the typical spin density and charge density distributions on the nitrogen doped graphene. For an N dopant, the atoms with high charge density are always those bonded to the nitrogen atoms while those with high spin density are the second or third neighboring carbon atoms. Most identified active sites are those carbon atoms with high charge or spin density or high value of combination of charge and spin. For example, for the graphene with two doped nitrogen atoms and Stone-Wales defects, carbon #27 and #24 possess the highest and second highest atomic charge density (Figure 4-6(a)) while Carbon #16 has the highest spin density (Figure 4-6(b)). These atoms are the catalytic active points identified for the ORR.

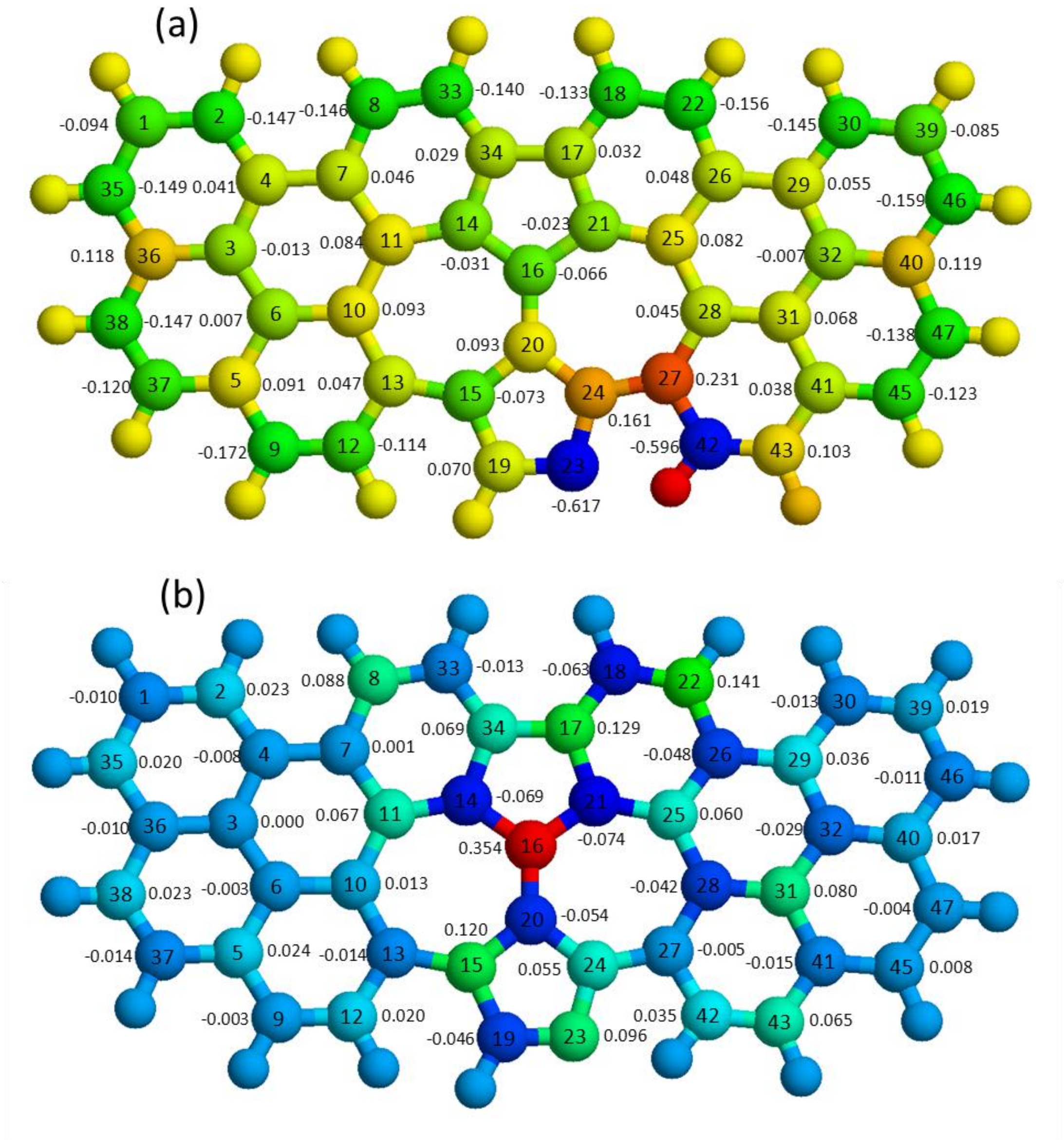

Figure 4-6 (a) Atomic charge density and (b) Spin density distribution on the nitrogen-doped graphene with Stone-Wales defects.

As mentioned above, OOH adsorption on graphene represents one of the most important steps for ORR. The adsorption energies of OOH may be sensitive to atomic charge density and spin density of the active sites. We have calculated the charge and spin densities of active sites on several kinds of nitrogen doped graphene structure, in which the number of doped nitrogen atoms increases from one to four in cluster. Figure 4-7 shows the adsorption energy as a function of atomic charge density *e* and spin density *s*. For atomic charge density *e*= -0.087 ~ +0.085, and *e* = +0.205 ~ +0.263, the adsorption energy increases nearly linearly with increasing the spin density (Figure 4-7(a)), which is consistent with the results obtained by Sidik and Anderson [196]. On the other hand, the adsorption energy also increases with increasing the atomic charge density but with large scattering (Figure 4-7(b)). It should be noted that for the case of no spin density, only those atoms with relatively high charge density can act as a catalytic site, but these sites with high charge density usually lead to much higher adsorption energy. Therefore, any approaches that increase the spin or charge density of carbon atoms will facilitate the ORR on graphene surface.

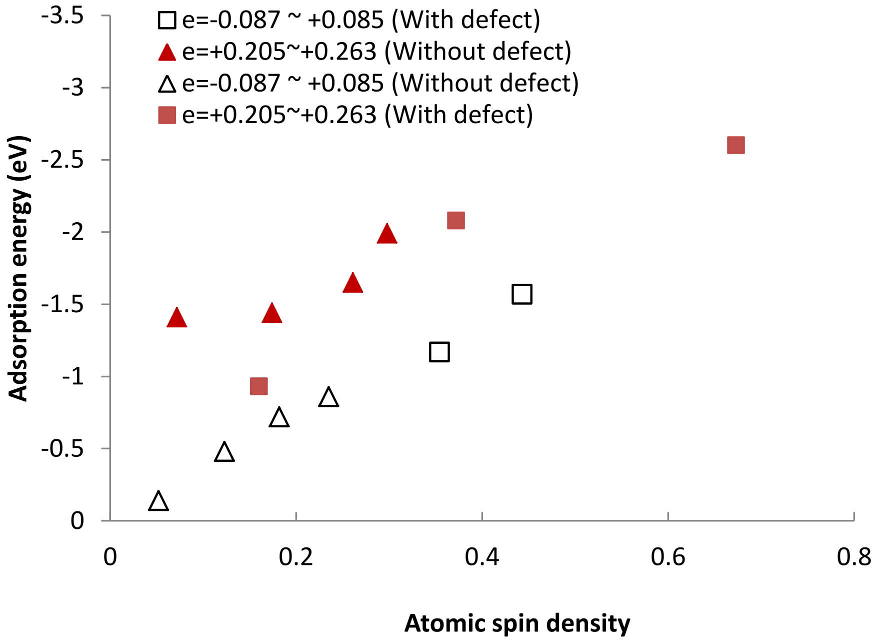
-3.5
-3
-2.5
-2
-1.5
-1
-0.5
0
Adsorption energy (eV)
0
0.2
0.4
0.6
0.8
Atomic spin density
☐ e=-0.087 ~ +0.085 (With defect)
▲ e=+0.205~+0.263 (Without defect)
△ e=-0.087 ~ +0.085 (Without defect)
■ e=+0.205~+0.263 (With defect)

(a)

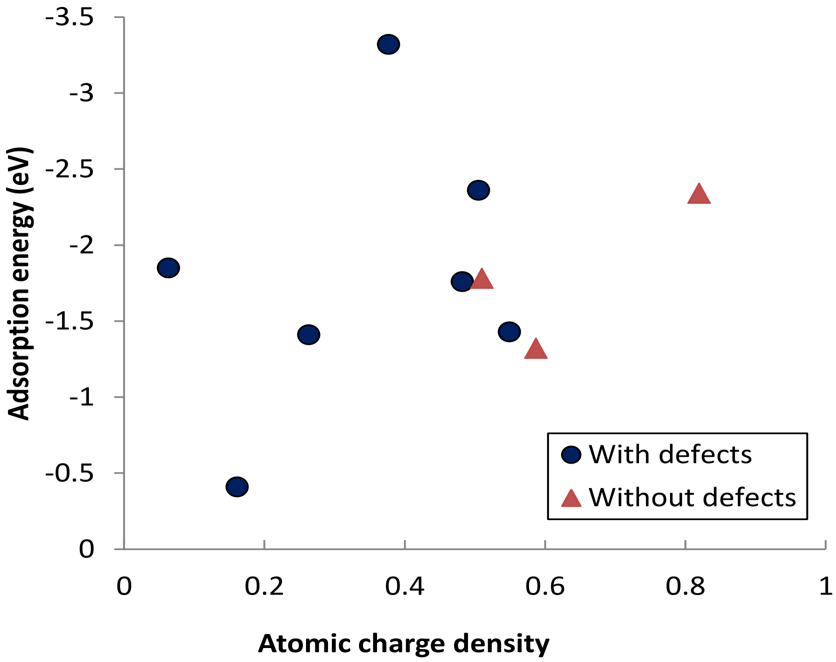
-3.5
-3
-2.5
-2
-1.5
-1
-0.5
0
Adsorption energy (eV)
0
0.2
0.4
0.6
0.8
1
Atomic charge density
● With defects
▲ Without defects

(b)

Figure 4-7 The adsorption energy of OOH on graphene as a function of (a) Spin density for atomic charge *e*= -0.087 ~ +0.085, and *e* = +0.205 ~ +0.263, and (b) Atomic charge density for *s*= -0.036 ~ +0.0072. The adsorption energy is calculated from Reaction (4-23) in the absence of charge.

The above energy calculation was performed without considering the presence of charge. We have calculated the adsorption energy of OOH^+ adsorbs on the graphene that carries a negative charge. As expected, the charge on graphene does influence adsorption; however, the reaction energy is closely correlated with that in the absence of charge. For example, for OOH^+ adsorption reaction on the graphene (G) shown in Figure 4-5(a),

$$G(e^-) + OOH^+ \rightarrow G\text{-}OOH, \qquad (4\text{-}16)$$

the reaction energy is -11.25 eV. It consists of two elementary reactions:

$$G(e^-) \rightarrow G + e^- \qquad (4\text{-}17)$$

$$OOH^+ + e^- \rightarrow OOH \qquad (4\text{-}18)$$

with the reaction energies of 1.80 eV (graphene electron affinity) and -11.89 eV (OOH ionization potential), respectively. For the same reaction without considering the charge,

$$G + OOH \rightarrow G\text{-}OOH \qquad (4\text{-}19)$$

with a reaction energy of -1.16 eV. Thus, the reaction energy of Reaction (4-16) should be the energy sum of Reactions (4-17) ~ (4-19). Since Reactions (4-17) and (4-18) is the deionization process of OOH and graphene, their reaction energy should be constant for a given graphene structure under the standard condition. Thus, the adsorption energy calculated without considering the charge E_1 is equal to that in the presence of charge E_2, plus a constant c: $E_1 = E_2 + c$.

As externally introduced charges may influence the charge and spin density on graphene and further ORR process, we have examined the charge and spin density distribution on N-doped graphene in the presence of an additional negative charge. It turns out that the additional charge does not influence the charge distribution on graphene (slight variation in magnitude). Thus, the additional charge does not affect the ORR mechanisms on the graphene. On the other hand, the spin density change is complicated in the presence of charges. When one additional negative charge is introduced onto the graphene, the spin density disappears. When two additional negative charges are introduced, the spin density redistributes, but the overall distribution is similar to those before the charge is introduced, i.e. there is always one carbon atom with a maximum spin density of ~0.35-0.4, in adjacent to the nitrogen atoms. In this case, the catalytic ability should remain similar even when additional charges are introduced. More work is needed to understand the radical reactions and the effect of spin density on graphene.

Apart from the structures with two nitrogen doping atoms, we have examined the catalytic activities of various graphene structures with a cluster of dopants and defects (Fig.4-8). Note that N atoms are separated by 2-3 crystal lattices (~2-3 Å) such that there is no N-N bond in the clusters. Recent DFT calculation showed that the formation of N-N bond in graphene is energetically unfavorable, and the probability of having two doped N atoms at neighboring sites is quite low [197]. More recently, Scanning Tunnel Microscopy (STM) direct imaging on N-doped graphene revealed that most N atoms exist either isolated or in cluster in which N atoms are separated in several lattices [198]. We also calculated the energies of all these optimization structures of nitrogen doped graphene with N-N bond and those with N atoms separated. The energy of former is higher than that of the later. So all the clusters generated in this study are energetically favorable.

The reaction energy and reversible potential for each reaction step of ORR on these nitrogen-doped graphene were calculated. Figure 4-9 shows the reversible potential for each reaction step of ORR as a function of the number of N doping atoms. OOH molecule cannot adsorb on graphene without N doping, indicating that the N doping is a key to graphene as an ORR catalyst. For the graphene without defects, with increasing the number of nitrogen atoms in the cluster, the reversible potential of O-O bond dissociation rapidly increases while the potential of water forming slightly reduces, but the potential for *OOH adsorption does not change too much. Therefore, the N clustering can significantly promote the O-O bond dissociation reaction. For the graphene with defects, the reversible potential changes quite differently compared to N doping alone. When the size of N clusters increases, the reversible potential of O-O bond dissociation quickly reduces to a value around the standard reversible potential (1.228V, dot lines in Figure 4-9), whereas the potential for water forming quickly increases to the same range. The potential for *OOH adsorption varies slightly around the standard value. So, in the presence of defects, the N clustering makes the reversible potentials of each reaction step closer to the ideal reversible potential. Relatively equal potentials in each reaction step may increase the reaction rate in ORR [196]. These results suggest that ORR occurs more easily on the nitrogen doping clustering with defects than the single nitrogen doping. Although the defects alone do not have catalytic capability, the combination of the N cluster and defects can strongly facilitate the ORR on graphene.

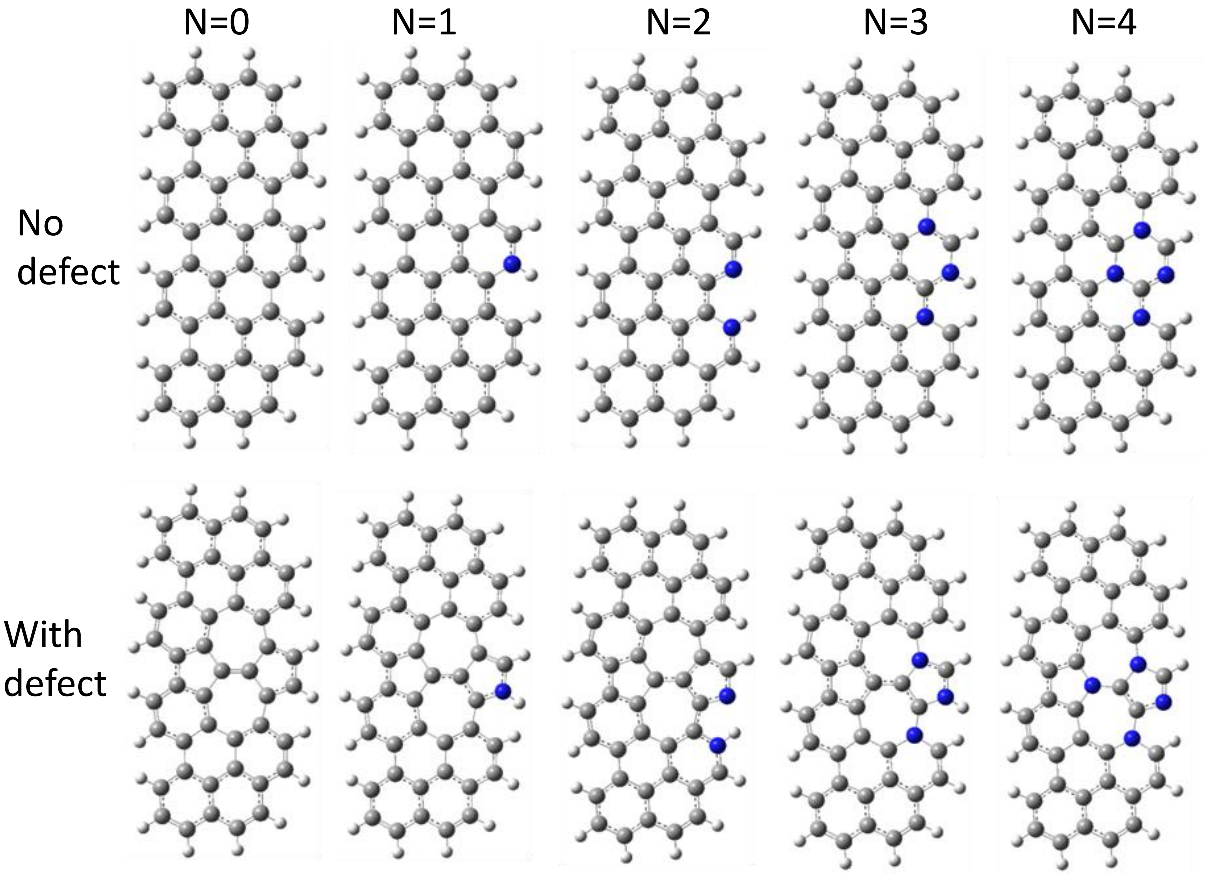

Figure 4-8 The graphene structures with a number of dopants and defects. N= the number of nitrogen dopants. Grey, blue, and small white balls represent carbon, nitrogen, and hydrogen atoms, respectively. The structures in the first row contain no defects while the structures in the second row have.

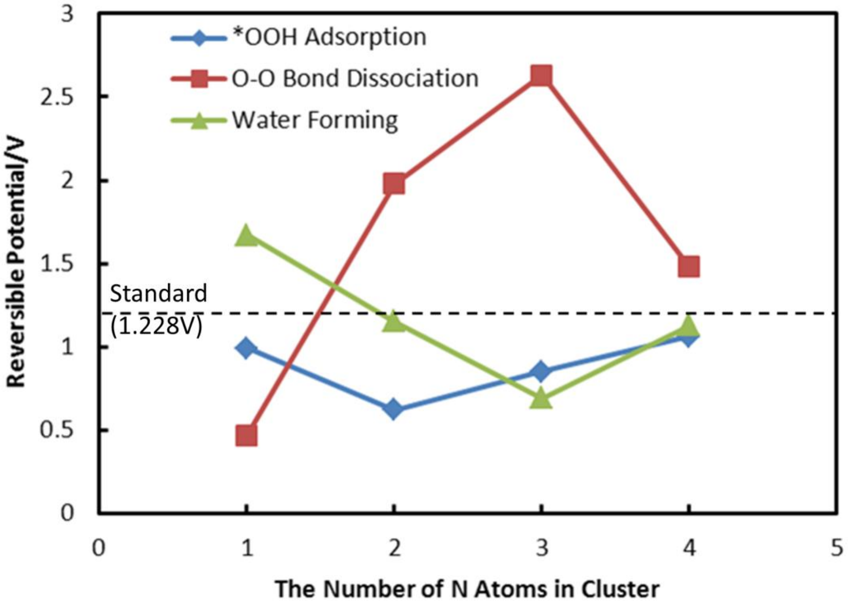
*OOH Adsorption
O-O Bond Dissociation
Water Forming
Standard
(1.228V)
Reversible Potential/V
The Number of N Atoms in Cluster
0
0.5
1
1.5
2
2.5
3
0
1
2
3
4
5

(a)

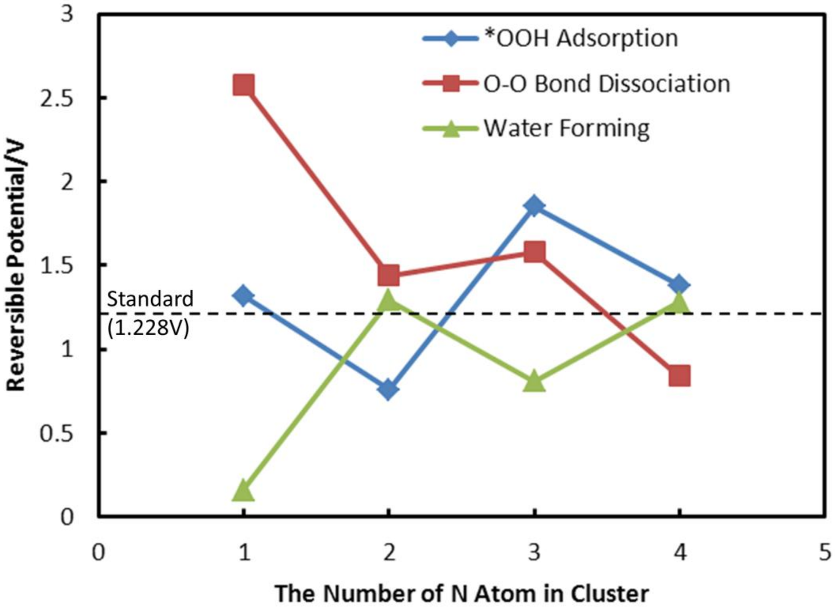
*OOH Adsorption
O-O Bond Dissociation
Water Forming
Standard
(1.228V)
Reversible Potential/V
The Number of N Atom in Cluster
0
0.5
1
1.5
2
2.5
3
0
1
2
3
4
5

(b)

Figure 4-9 The reversible potentials of ORR versus N cluster size for the graphene (a) without defects, and (b) with defects. Dot lines represent standard reversible potential (1.228 V).

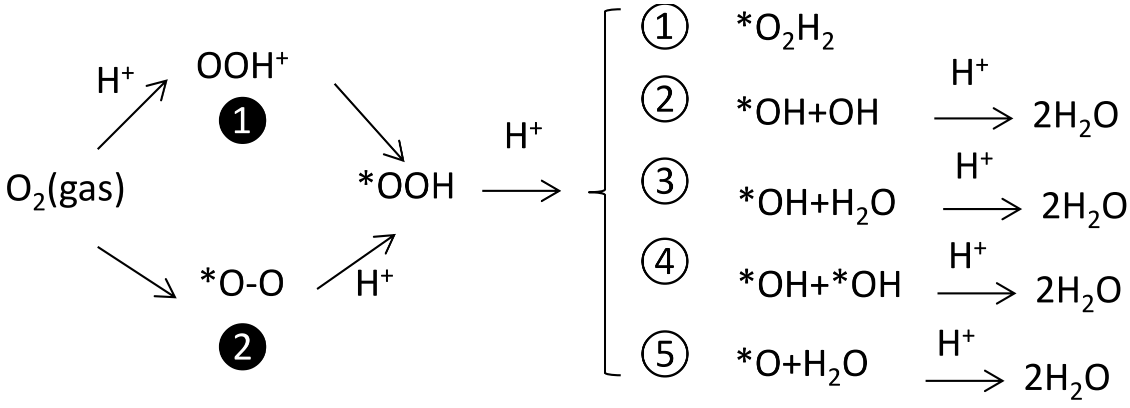

Figure 4-10 Reaction scheme of ORR on N-graphene in acidic solution, where ❶ presents an intermediate OOH adsorption mechanism and ❷ a direst O_2 adsorption mechanism, and ① ~ ⑤ represents 5 reaction pathways after OOH adsorption.

The N cluster and defects also influence the reaction pathway. In addition to the reaction path listed in Table 4-3, different reaction routes and catalytic behaviors were observed for multiple-doping graphene. The identified reaction pathways include two-electron transfer (path ① in Figure 4-10) and four-electron transfer (Paths ② -⑤). Path ① is a typical two-electron transfer reaction while all other reaction paths identified are four-electron transfer reaction. The reversible potential for Path ① is 0.685 V, which is consistent with the results from the literature [196]. The two-electron process usually is much less efficient than four-electron one [176]. For Path ③, the introduction of a hydrogen results in O-O bond breaking and formation of two OH molecules. One adsorbs on the same site as the OOH on graphene while the other combines with H that bonds to a nitrogen atom to directly form a water molecule. Finally, the adsorbed OH combines with H to form a water molecule. The overall reaction reversible potential is 1.228 V. Path ④ is similar to that listed in Table 4-3, but here both OH molecules adsorb on graphene. In the last path (Path ⑤), O-O bond breaking generates an adsorbed O and a water molecule. H further reacts with the adsorbed O to form water. The overall reversible potential is also 1.228 V, which is equal to the standard reversible potential U^0 of oxygen and hydrogen redox reaction. This value corresponds to the standard Gibbs energy of reaction, $\Delta G^0 = 4.916$ eV, and is the maximum energy available to do electrical work.

The above reversible potentials were calculated under the assumption that all the Gibbs free energy is converted into electric work. However, the experimentally observed onset potential for O_2 reduction to water over nitrogen-doped graphene and carbon nanotube is usually much smaller than the standard reversible potential 1.228 V. This overpotential is caused by the exergonicity of OOH (ads) dissociation step [192]. In principle, any exergonic reaction that does not include the transfer of an electron during the course of the overall reaction will cause the overpotential, even if all of the electron transfer steps are activationless. In this study, the OOH (ads) dissociation reaction occurs on the N-doped graphene in four electron transfer ORR. For Path ②, Reaction (2) in Table 4-3 can be separated into two sub-reactions: $*OOH \rightarrow *O + OH$ and $*O + e^- + H^+ \rightarrow *OH$. Similarly, O-O bond dissociation reaction in Path ③ contains two sub-reactions: $*OOH \rightarrow *O + OH$ and $*O + OH + e^- + 2H^+ \rightarrow *OH + H_2O$ while in Path ④ the dissociation reaction: $*OOH \rightarrow *O + OH$ and $*O + OH + e^- + H^+ \rightarrow *OH + *OH$. For Path ⑤ the dissociation reaction is: $*OOH \rightarrow *O + OH$ and $*O + OH + e^- + H^+ \rightarrow *O + H_2O$. In the ideal case, this dissociation reaction will be energonic neutral. In the nonideal case (like the reaction on catalytic surfaces), when the reaction is exergonic, free energy $\Delta G'$ is lost. Thus, $\Delta G'$ is not available for electrical work and should be subtracted from ΔG^0. The Gibbs energy available for electrical work is:

$$\Delta G_w = \Delta G^0 - \Delta G' \tag{4-20}$$

Similar to the treatment in Eq. (4-14), $\Delta G'$ is replaced by the reaction energy E_{ex} for the exergonic reaction. Thus, the effective reversible potential U_{eff} can be written as

$$U_{eff} = - \Delta G^0/(nF)+E_{ex}/(nF) \tag{4-21}$$

We calculated the lost Gibbs free energy $\Delta G'$ of exergonic reaction (*OOH → *O + OH) included in Paths ② ~ ⑤, yielding 0.56 eV, 0.63 eV, 0.30 eV and 0.74 eV, respectively. So, the effective reversible potential U_{eff} of Path ①, Path ③, Path ④ and Path ⑤ is 1.09 V, 1.07 V 1.15 V, and 1.04 V respectively.

We also found incomplete reaction paths at some active sites, mostly on the graphene with large N clusters. For example, after OOH adsorption, $O_2 + H^+ + e^- \rightarrow$ *OOH, (U=2.55 V/SHE) and O-O disassociation, $^*OOH + 2H^+ + e^- \rightarrow {}^*OH + H_2O$, ($U$=1.83 V/SHE), the reversible potential of the following steps, $^*OH + H^+ + e^- \rightarrow H_2O$ is -1.13 V/SHE, which cannot occur spontaneously. In all these incomplete paths, either OOH adsorption or O-O disassociation potential or both are too high. As a result, the next reactions are suppressed.

The number of active sites and effective reversible potential against the size of N clusters are summarized in Table 4-4. Overall, with increasing the size of N cluster, the number of active sites per nitrogen atom first increases to a maximum value at double N cluster, and then reduces linearly. In the presence of defects, more active sites are created when N dopants exist in cluster. This effect can be attributed to the interaction between the defect and dopants. Considering the fact that the defects make the reversible potentials closer to the ideal value (1.228V) (Figure 4-9(b)) if N exists in the form of clustering, a small cluster (ideally two N) combining with defects would maximize the catalytic active sites available for ORR. Interestingly, recent study shows that most N dopants exist in single N or double N cluster on single-layered graphene [198].

Table 4-4 The number of active sites and effective reversible potential for nitrogen-doped graphene.

	The number of N atoms in cluster	**0**	**1**	**2**	**3**	**4**
No defect	The number of active sites	0	1	3	2	1
	Effective Reversible potential V/SHE	-	1.04	1.07~1.15	1.07	1.15
With defect	The number of active sites	0	1	3	2	3
	Effective Reversible potential V/SHE	-	1.04	1.15	1.07~1.15	1.15

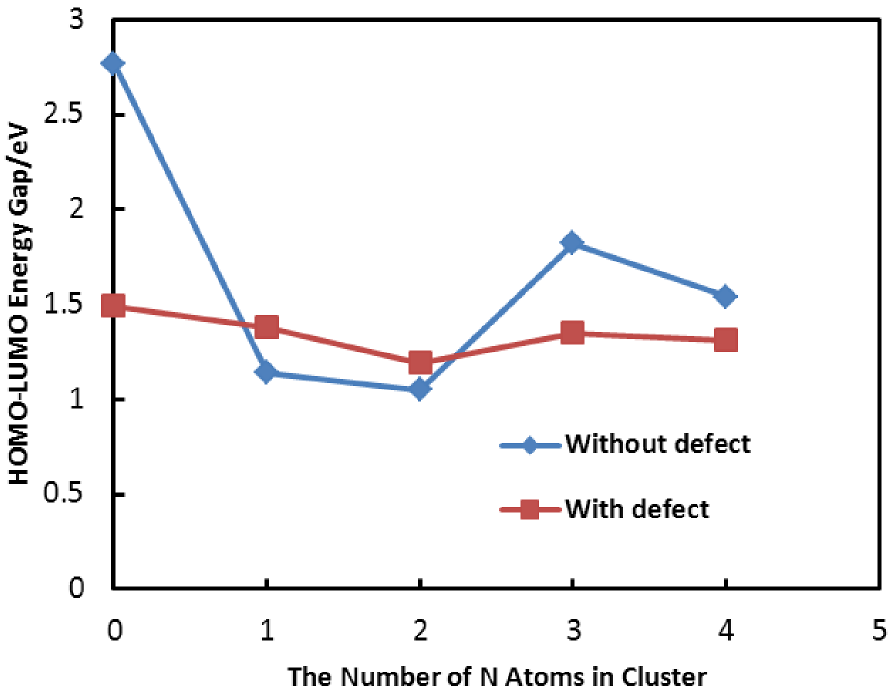

Figure 4-11 HOMO-LUMO energy gap as a function of the number of nitrogen doped atoms in cluster with and without Stone-Wales defects.

To further examine the effect of the doping and defects on the catalytic behavior of graphene, we calculated energy separation between the highest occupied molecular orbital (HOMO) and lowest unoccupied molecular orbital (LUMO), which can be used as a simple indicator of kinetic stability. The smaller energy gap means that the state of the graphene is energetically favorable to add electrons to a high-lying LUMO, to extract electrons from a low-lying HOMO, and so to form the activated complex of any potential reaction [199]. The HOMO-LUMO gaps of graphene with and without defects versus the number of nitrogen atoms in cluster are shown in Figure 4-11. In the absence of defects, the incorporation of one or two nitrogen atoms into the graphene lattice reduces HOMO-LUMO gap by a factor of 2.3 compared to perfect graphene, but with further increasing N cluster size (3~4N), the gaps increase to a level of ~1.7 eV from 1.1 eV. This trend is consistent with the results listed in Table 4-4, where the number of active sites reduces with increasing the cluster size. In the presence of Stone-Wales defects, the HOMO-LUMO energy gap is much lower than the perfect graphene. The insensitivity of the gap to the introduction of N dopants suggests that the chemical reactivity of the graphene is controlled by the defects. As a result, all the Stone-Wales defective graphene has relatively high chemical reactivity. As shown in Table 4-4, the number of active sites on graphene with defects is more than that on the graphene without the defects. In addition to increasing the number of active sites, defects can promote some catalytic reactions, i.e., the adsorption and O-O bond breaking reactions (Figure 4-9). However, in the case of large N cluster, the combination of N cluster and defects can sometimes over-promotes these reactions with a consequence of blocking the following reactions (i.e., water formation). As discussed above, the presence of N dopants generated active sites that have high adsorption energy (e.g. OH on graphene). However, the bonds may be too strong to break in the following reactions. Consequently, the following catalytic reactions cannot occur spontaneously. Thus, to optimize the catalytic performance, materials structures should be controlled to have small N doping clusters in combination with material defects.

4.3 Sulfur-doped graphene as efficient oxygen reduction reaction catalysts for fuel cells

For the new metal-free catalysts of fuel cells, including the N-doped carbon materials, such as CNTs [200, 201], graphene [202, 203], and mesoporous graphitic arrays [204], B doped [205] and N/B co-doped graphene [206] exhibit high electrocatalytic activity and CO tolerance in comparison to conventional platinum catalysts for ORR and are promising candidates for replacing Pt-based catalysts. More recently, sulfur-doped graphene has been synthesized using different methods [207, 208], which also exhibits even better catalytic activities than commercial Pt/C. Based on the study of section 4.1 and 4.2 we obtained the high acticity of nitrogen doped graphene may be attributed to the polarized distribution of spin and charge density which are caused by the introduced nitrogen atoms. What is the situation for the sulfur doped graphene? In this section, we studied the doping structure of sulfur atoms on graphene and their catalytic mechanism for ORR in acidic environment.

4.3.1 Mehods

Four possible types of sulfur doped graphene were considered as follows, as schematically shown in Figure 4-12. Type one is sulfur atoms adsorbed on the surface of graphene. Type two represents the sulfur atom substitution at the zigzag or armchair edge of the graphene. In Type three, sulfur atoms substitutes the carbon atoms at the edge (zigzag and armchair) of graphene in the form of –C-SO_2-C- . The last type is two pieces of graphene connected by sulfur cluster ring. These models of doped graphene are built based on the experimental structure analyses of sulfur doped graphene [208-210]. X-ray photoelectron spectroscopy (XPS) shown all the high resolution S2p peaks of sulfur doped graphene could resolved into three different peaks at binding energies of ~163.9, 165.1 and 168.9 eV, respectively. The former two peaks were corresponding to $2p_{3/2}$ and $2p_{1/2}$ positions of thiophene-S owing to their spin-orbit coupling. The third peak related to some oxidized sulfur. Binding energy around 162.0 eV (S-H) and higher than 165.5 eV were not found. So the sulfur are inferred mainly doped at the edges or on the surface of graphene in the form of –C-S-C- or –C-SO_2-C-. In these doped graphene, Stone-Wales defects were also introduced to study defect effects. Stone-Wales defects are one type of important topological defects in sp^2-bonded carbon materials, which could affect the electronic property of graphene. The optimization structures of all these sulfur doped graphene were calculated using the DFT. Formation energies of these sulfur doped graphene were calculated as: $E_f = \mathbf{E}_{\textbf{S-graphene}} + \boldsymbol{y\mu}_{\mathbf{C}} - (\mathbf{E}_{\textbf{graphene}} + \boldsymbol{x\mu}_{\textbf{S/S-oxide}})$, where $E_{\text{S-graphene}}$ is energy of S doped graphene, E_{grpahene} is the energy of corresponding graphene, μ_C is the chemical potential of C, and $\mu_{\text{S/S-oxide}}$ are the chemical potential of S (in the form of S_8), or sulfur oxide, respectively.

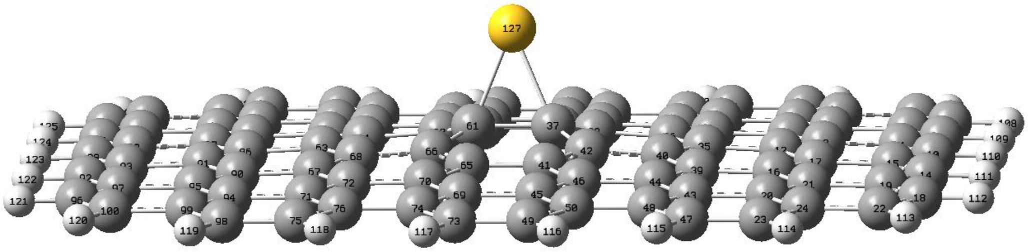

(a)

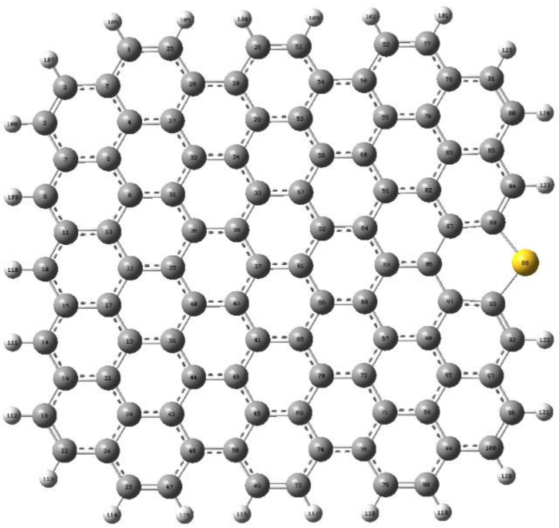

(b)

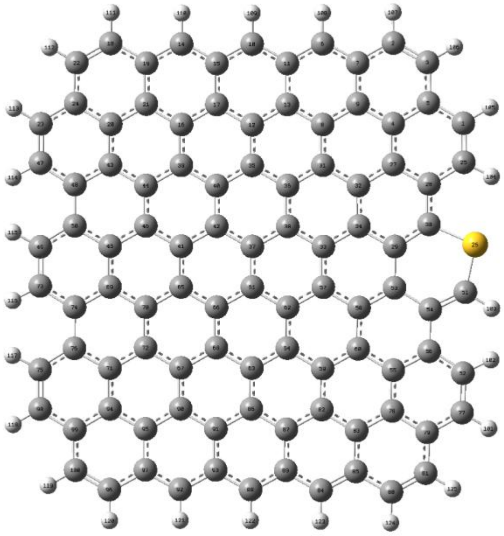

(c)

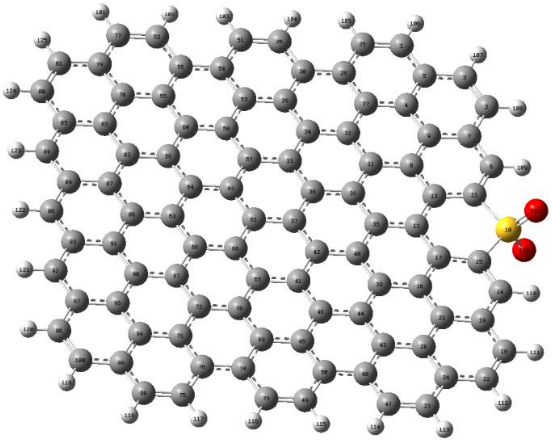

(d)

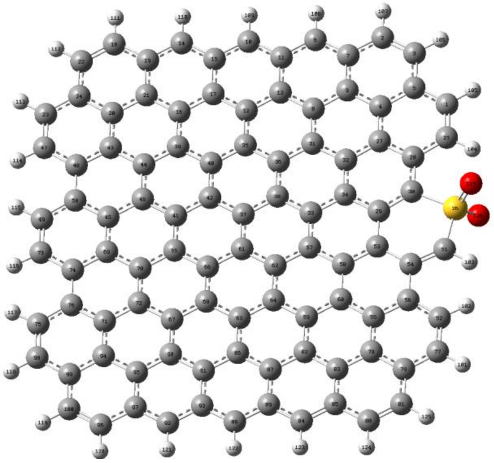

(e)

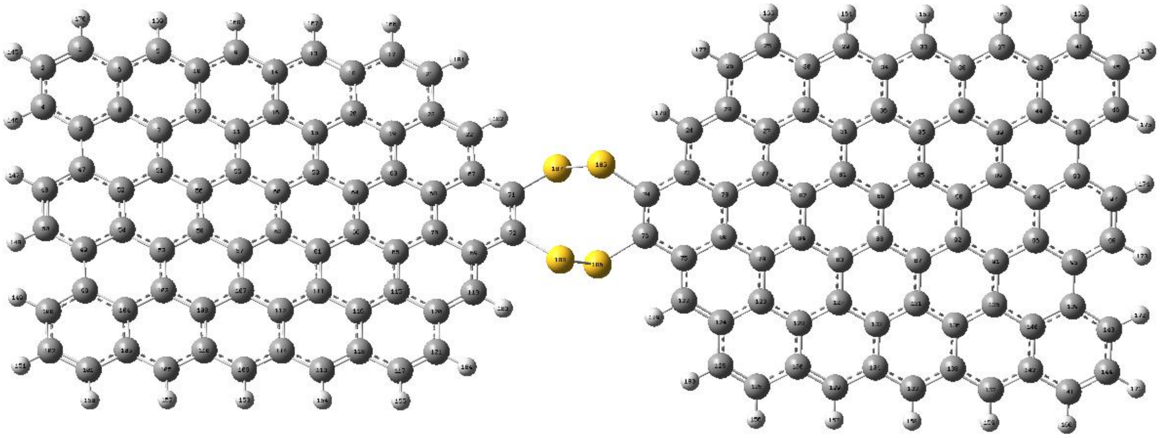

(f)

Figure 4-12 Several possible sulfur-doped graphene structures: (a) Sulfur atoms adsorbed on the surface of the graphene; Substituting sulfur atoms at (b) zigzag and (c) armchair edges; SO_2 substituted at (d) zigzag and (e) armchair edges and (f) sulfur ring cluster connecting two pieces of graphene. The structures of the graphene are shown only partially to highlight the doping structures. Small white, grey, yellow, and red balls represent hydrogen, carbon, sulfur, and oxygen atoms, respectively.

The ORR processes were simulated to explore possible reaction pathways in the presence of S-doped graphene. For the first electron transfer reaction process, it was described in the section 4.1. To examine this reaction path, we set an OOH molecule near the graphene plane at a distance of 1.5 ~ 3 Å, and then observe if it adsorbs graphene surface. We also set O_2 molecular near the graphene to check whether it could adsorb at the potential catalytic active sites or not. After the first electron transformation, the succeeding electron transforming was simulated by continuing to add H atoms in the system. For each step, we obtained the optimized structure, and calculated the reaction free energy ΔG. I d f d d ff b f g of l d final states given by the expression [211, 212]: $\Delta G = \Delta E + \Delta ZPE - T\Delta S$, ΔE

reaction energy of reactant and product molecule adsorbed on catalyst surface obtained from DFT calculations, ZPE is the zero point energy, T is the temperature and S is the entropy. For the reaction with negative reaction free energy, it would occur spontaneously.

4.3.2 Results and discussion

Figure 4-12 shows four possible sulfur-doping structures in graphene, namely, sulfur chemisorption on surface, S substitution at edge, SO_2 substitution at edge, and sulfur ring clusters, which have been described in details in method section. The formation energies of these sulfur doped graphene were calculated and are listed in Table 4-5. The formation energies for sulfur adsorbing on the graphene surface (Figure 4-12(a)) are negative, but they are positive for sulfur or sulfur oxide substitution at the edges of graphene (Figure 4-12 (b-e)), sulfur ring cluster connecting graphene (Figure 4-12(f)). Therefore, compared to the sulfur (or sulfur oxide) edge substitution (Figure 4-12(b-e)) or sulfur ring cluster connecting graphene (Figure 4-12 (f)) sulfur adsorption on graphene surface are energetically favorable. In the presence of Stone-Wales defects on graphene, the formation energies of sulfur doped graphene are lower than those of perfect graphene. So Stone-Wales defects facilitate sulfur doped on the graphene. This may be attributed to the fact that defects change the local charge distribution and crystal lattice. For the edge substitution, the difference in formation energy between perfect and defective graphene is ~0.36 eV, lower than that of the sulfur (sulfur oxide) adsorbing on graphene surface or sulfur ring cluster graphene. Thus, Stone-Wales defects at the center of graphene have a weak effect on the sulfur edge substitution. For the same graphene structure, the formation energy of sulfur atom (sulfur oxide) at zigzag edge is always lower than that of armchair one, suggesting that sulfur (sulfur oxide) is preferable to substitute the carbon atoms at the zigzag edge.

Table 4-5 Formation energy (eV) of S doped graphene

Graphenes	Surface adsorption P 1	Surface adsorption P 2	Zigzag edge substitution	Armchair edge substitution	SO_2-zigzag edge substitution	SO_2-armchair edge substitution	Ring clustering
Without defect	-1.46	-1.73	0.90	2.02	1.47	2.73	2.70
With Defect	-2.60	-2.31	0.89	1.80	1.44	2.37	2.54

We calculated spin and charge densities of each atom of the sulfur-doped graphenes and determined possible ORR catalytic active sites on these doped structures on the base of these spin and charge density distributions. It was shown in section 4.1 and 4.2 that the ORR catalytic active sites are closely related to the charge and spin density distributions. Figure 4-13 shows the atomic charge and spin density distributions on the sulfur-doped graphenes. For sulfur-adsorbed graphene surface, the sulfur atom does not introduce extra unpaired electron, therefore, the graphene does not exhibit additional spin density. The charge density, on the other hand, redistributes on perfect or defective (Stone-Wales defects) S-doped graphenes (Figure 4-13 (a) and (b)). Specifically, carbon atoms with # 11, 15, 89, and 93 at zigzag edge, possess higher positive charge density around 0.17. These carbon atoms may be the catalytic active sites for ORR. To test this hypothesis, we have calculated the adsorption of OOH or O_2 species on these sites by setting them near these potential catalytic sites. The adsorption of OOH or O_2 species on graphenes is the first step necessary for the graphene to catalyze the ORR. The results show that both OOH and O_2 can adsorb on these atoms located at zigzag edge of graphene with Stone-Wales defect but cannot on the graphene without Stone-Wales defects. Thus, those S-adsorbed graphene could have catalytic activities depending on the Stone-Wales defects. Here, the defects play an important role in facilitating the ORR. Compared to the perfect graphene structure, the sulfur adsorbed graphene surface twist a little bit when the Stone-Wales defects were introduced, which changed the crystal lattice and local charge distribution on the graphene. The effect of Stone-Wales defects will be further discussed in the following context.

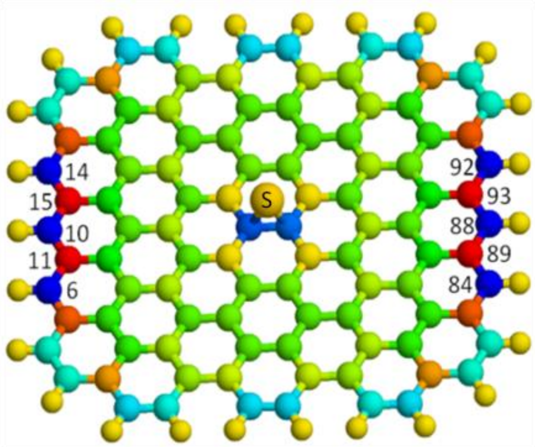
14
15
10
11
6
S
92
93
88
89
84

(a)

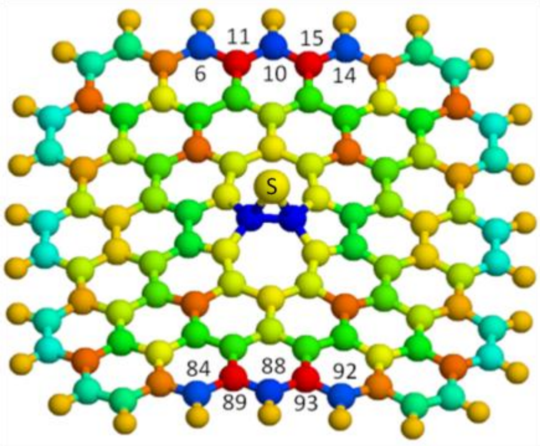
11
15
6
10
14
S
84
88
92
89
93

(b)

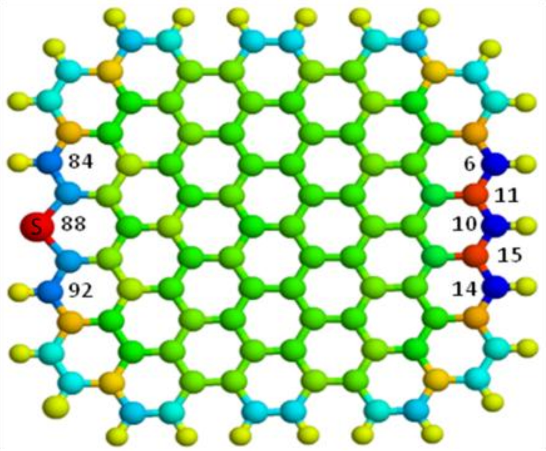
84
S
88
92
6
11
10
15
14

(c)

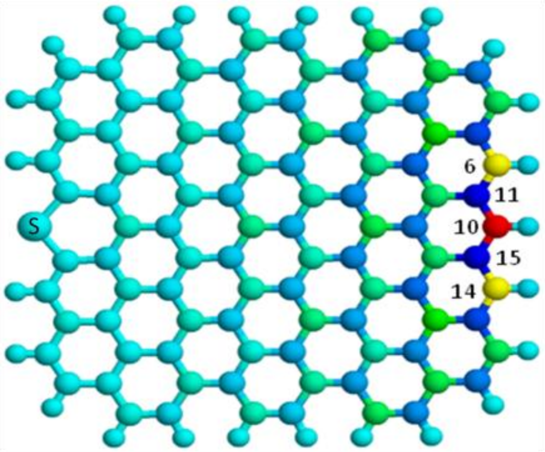
S
6
11
10
15
14

(d)

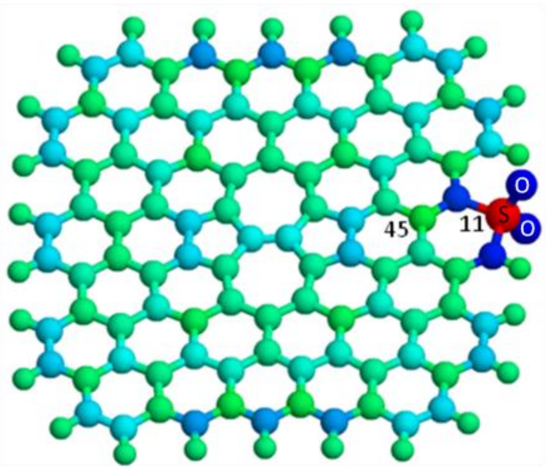
O
S
O
45
11

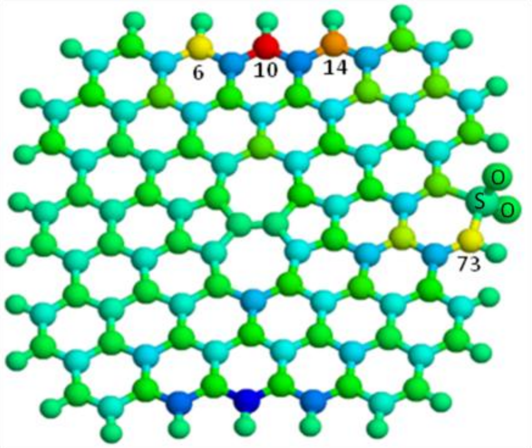
6
10
14
O
S
O
73

(e) (f)

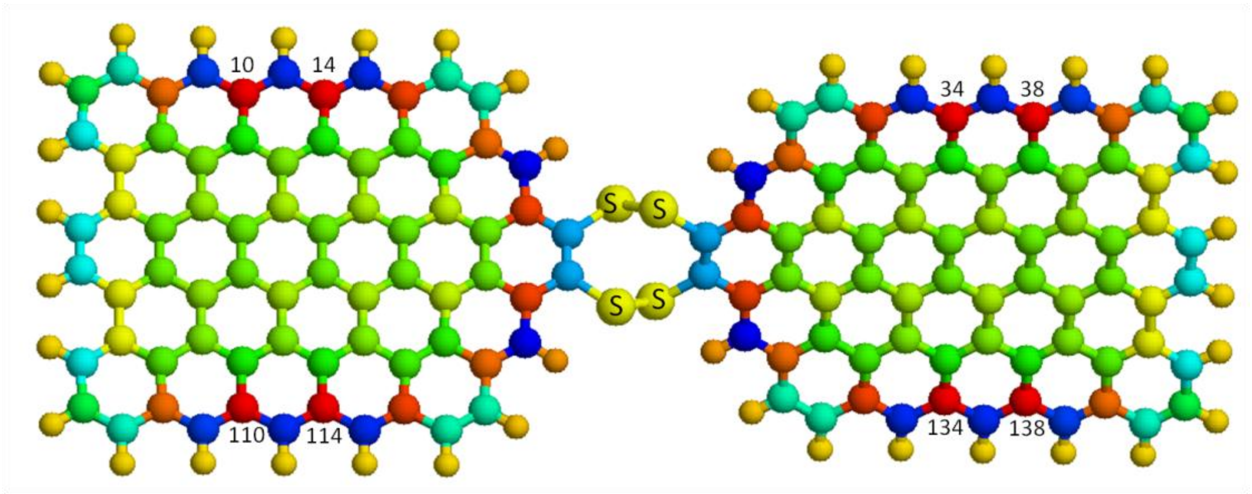

(g)

Figure 4-13 Atomic charge density and spin density distributions on the S-doped graphene. Atomic charge density distribution on S-adsorbed graphenes with (a) perfect structure and (b) one Stone-Wales defect; (c) Atomic charge density, and (d) spin density distributions on substituting S at zigzag edge of perfect graphene; (e) Atomic charge density, and (f) spin density on SO_2-doped graphene with a Stone-Wales defect; (g) Atomic charge density on sulfur ring cluster connecting two pieces of graphenes. The colors of the balls stand for relative values of charge and spin density. The density decreases linearly from positive to negative values in the color order of red, orange, yellow, green and blue. Sulfur and oxygen atoms are labeled with S and O, respectively. The unlabeled small and large balls represent H and C, respectively.

Figure 4-13 (c) and (d) shows the atomic charge and spin density distributions on the graphene with sulfur atoms located at zigzag edge, respectively. Similar to those above, the atom with high charge density is also located at the zigzag edge. Furthermore, spin density is also introduced on the atom at the edge. For example, the edge carbon atoms #11 and #15 possess the highest charge density of 0.19 among the carbon atoms. For spin density, edge atom #10 with the largest value of 0.39, and edge atoms #6 and

#14 with the second largest value of 0.27 are found on the graphene. In addition, the sulfur atom (#88) obsesses a maximum positive charge density of 0.22. Similar spin and charge density distributions can be found on the defective graphene structures with sulfur oxide atom at armchair edge (Figure 4-13 (e) and (f)). Besides, the carbons neighboring the doped sulfur oxide also have high spin and charge densities. For the sulfur ring cluster connecting two pieces of graphene, these atoms possessing higher charge density are also at the zigzag edge or neighboring the sulfur atoms on the graphene, but the value of them is less than 0.19. (Figure 4-13 (g)) We have tested these atoms with the high charge or spin density and confirmed that all these atoms with charge density larger than 0.20 and spin density larger than 0.15 can adsorbing OOH or O_2 and could be the potential catalytic active sites for ORR.

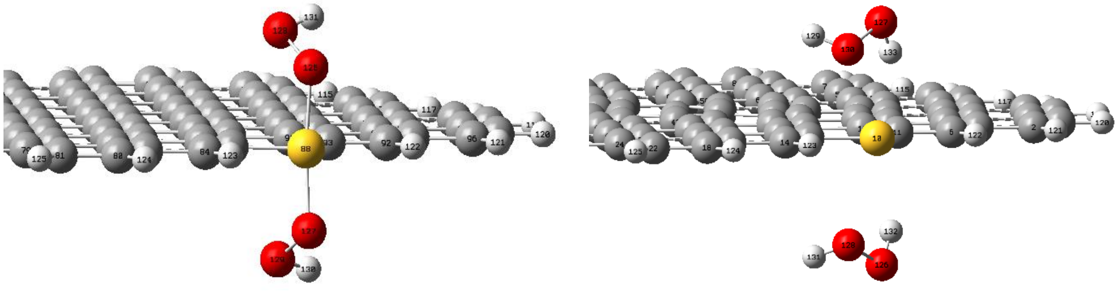

(a) (b)

Figure 4-14 ORR process on the sulfur doped graphene when the catalytic active site is sulfur atom: (a) two OOH molecules adsorbed on the sulfur atom, and (b) two H_2O_2 molecules formed and departed from the sulfur atom after the introduction of two more H atoms.

Once an OOH is adsorbed on the doped graphene surface, the next step of the ORR could be the O-O bond break, which represents four-electron transfer. Otherwise, the ORR is the lower efficiency two-electron transfer. We have examined all the possible active sites selected on the base of large positive charge density and spin density, and simulated the reaction when a proton is added to the position near adsorbed OOH. We found that the ORR is either four-electron or two-electron transfers depending on the doping structures. In the case of sulfur atom being the catalytic active site, two OOH species can adsorb on the S atom (Figure 4-14 (a)). The distance between adsorbed oxygen (OOH) and sulfur atoms decreased to 1.8 Å from the original distance 3.0 Å after structural optimized. Thus, S-O covalent bond was formed and the OOH chemically adsorbed on the S atom. As two more H atoms were set near to the oxygen atoms of two OOH species, they adsorbed to the oxygen atoms in OOH molecules that were bonded to the sulfur atom, respectively. The bonds between sulfur and oxygen atom break in the reaction, resulting in the formation of two H_2O_2 molecules. Finally, H_2O_2 molecules moved away from the graphene surface. The final distance between the H_2O_2 and graphene is 3.5 Å (Figure 4-14 (b)).

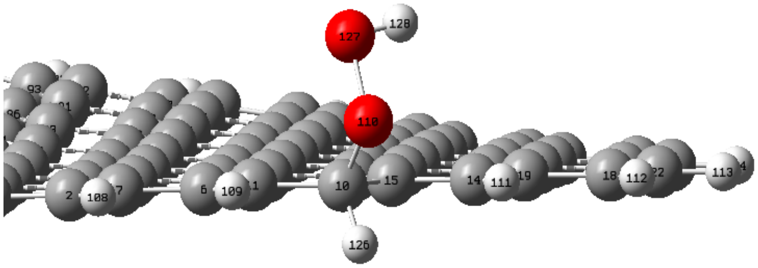

(a)

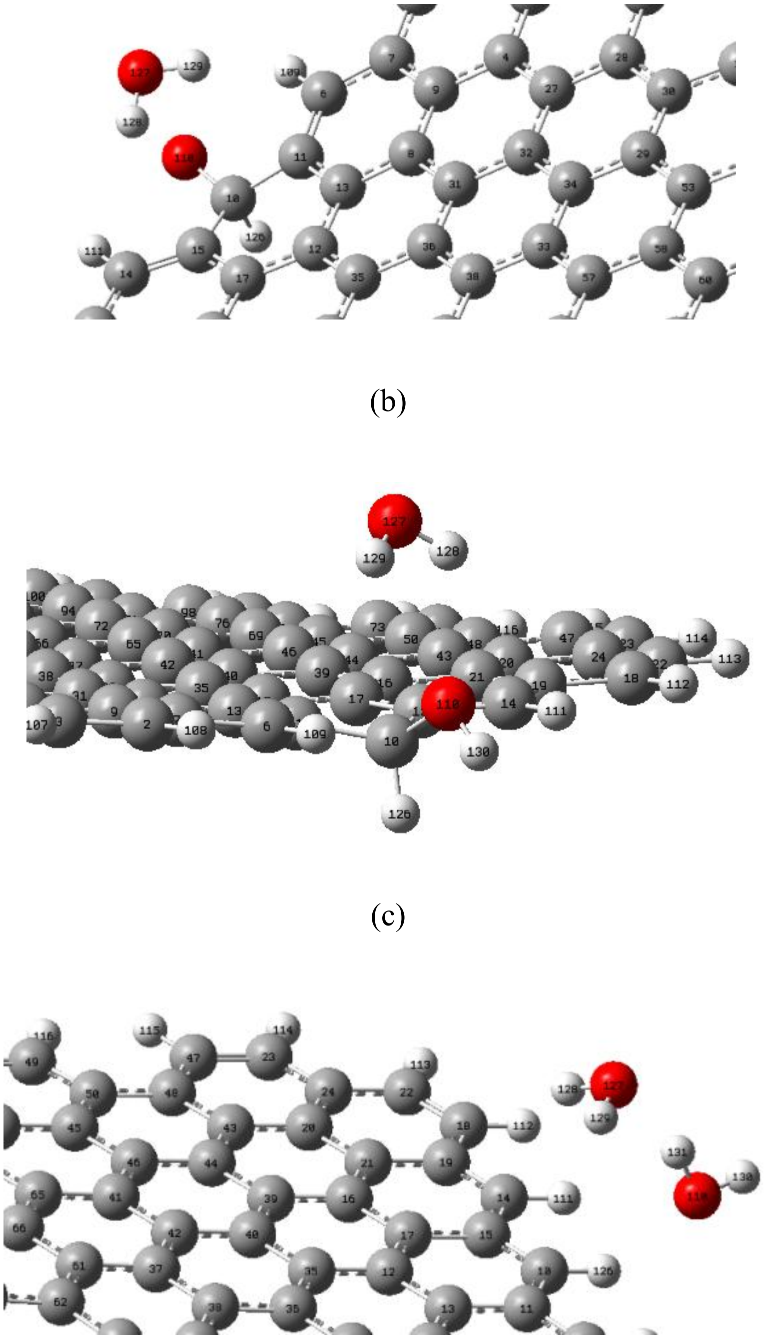

(b)

(c)

(d)

Figure 4-15 ORR processes on the sulfur-doped graphene where a carbon atom at the zigzag edge acts as the catalytic active site because of the highest spin density on it: (a) OOH adsorbed on the carbon atom, (b) rupture of O-O bond and formation of water molecule after an H atom was introduced into the system, (c) formation of an OH after the second H was introduced, and (d) formation of another water molecule after third H was introduced into the system.

For these carbon atoms with large spin or charge density as catalytic active sites, it was found that the four electron transfer usually occurs. For example, for edge S-doped graphene, OOH was able to adsorb to atom #10, the carbon with the highest spin density (Figure 4-15 (a)). When a proton was introduced near to the adsorbed OOH, it resulted in rupture of O-O bond and formation of one water molecule while one oxygen atom still adsorbed on the graphene alone (Figure 4-15 (b)). As mentioned above, the breakage of O-O bond is the key step of four electron transfer, which defines the process being four electron transfer pathway. After two protons were successively introduced into the system, as shown in Figure 4-15 (c) and (d), another water molecule were formed and departed from the graphene. The finial distance between two water molecules and graphene are ~3.4 Å.

R o f gy ΔG of above reaction steps on sulfur-doped graphenes was calculated for each sub-reaction. Fo f l o f p o , ΔG determined for two different mechanism (P o d o) D mj ov ’ p o o participation reactions and/or Y g ’ d o v m m m y o u o m graphene. Values of ΔG for two and four electron transfer pathways are listed in table 4-6. For the first electron transmission of the two electron transfer ORR on the graphene with ulfu om b g l y v , D mj ov ’ p o o p p o o 4-1 and 4-2 seem to be energetically unfavorable if these two reactions occur separately b u ΔG g v (-1.20 eV) for Reaction 4-1 but positive(1.03 ~ 1.05 eV) for Reaction 4-2. However, these two reactions could occur if one electron transfer takes place to form OOH in the solvent, followed by the adsorption of the neutral OOH on the graphene. For four-electron transfer which takes place at carbon active sites. Reactions 4-

1 and 4- ould o u u v ly ΔG fo m ll g v . Fo o - electron transfer ORR, Y g ’ d o o m g o o u b use O_2 could not adsorb on any potential catalytic active sites. For the four electron transfer, O_2 adsorption and following proton reactions (Reactions 4-3) and (Reaction 4-4)) ould o u u v ly, ΔG are all negative.

Table 4-6 R o f gy ΔG (V) of o l o d fou l o f reaction processes on sulfur doped graphene with and without Stone-Wales defects

		Sub-Reactions	No-Defects	Defects
Two-electron transfer pathway		$O_2 + H^+ + e^- \rightarrow {}^*OOH$	-0.17	-0.15
	Path I	$O_2 + H^+ + e^- \rightarrow OOH$	-1.20	-1.20
		$OOH + {}^* \rightarrow {}^*OOH$	1.03	1.05
	Path II	$O_2 + {}^* \rightarrow {}^*O_2$	CF	DA
		$^*O\text{-}O + H^+ + e^- \rightarrow {}^*O\text{-}O\text{-}H$	—	—
		$^*OOH + H^+ + e^- \rightarrow H_2O_2$	-1.33	-1.36
		$O_2 + 2H^+ + e^- \rightarrow H_2O_2$	-1.50	-1.51
Four-electron transfer pathway		$O_2 + H^+ + e^- \rightarrow {}^*OOH$	-1.21	-1.45
	Path I	$O_2 + H^+ + e^- \rightarrow OOH$	-1.20	-1.20
		$OOH + {}^* \rightarrow {}^*OOH$	-0.01	-0.25
	Path II	$O_2 + {}^* \rightarrow {}^*O_2$	-0.58	-0.88
		$^*O\text{-}O + H^+ + e^- \rightarrow {}^*O\text{-}O\text{-}H$	-0.63	-0.57
		$^*OOH + H^+ + e^- \rightarrow {}^*O + H_2O$	-0.80	-0.83
		$^*O + H_2O + H^+ + e^- \rightarrow {}^*OH + H_2O$	-1.38	-1.59
		$^*OH + H_2O + H^+ + e^- \rightarrow H_2O$	-1.60	-1.03
		$O_2 + 4H^+ + 4e^- \rightarrow H_2O$	-4.99	-4.90

No-Defects and Defects stand for these graphenes without and with Stone-Wales defects, respectively; * refers to chemi-adsorption on graphene; CF stands for calculation convergence failure; DA stands for O_2 dis-adsorption on graphene.

After the first electron transfer whatever reactions follow Path one or two, the intermediate products are the same, OOH adsorbed on the graphene. The reaction free energy of all sub-reactions for two or four electron transfer paths is negative for these sulfur doped graphene, indicating that the reaction process would be energetically favorable. In our models, the two electron transfer usually occurs at the S doped sites, which possesses the highest positive charge density, while the four electron transfer proceeds mostly on carbon atoms with the high positive spin or charge density. Thus, both sulfur and sulfur oxide doped graphene would show high catalytic activities. For the sulfur adsorbed graphene, the presence of Stone-Wales defects are critical for the graphene to catalyze ORR.

We have compared our calculations with the experimental results for sulfur-doped graphene. For two electron transfer reaction, $O_2 + 2H^+ + e^- \rightarrow H_2O_2$, our simulation predict that the free energies are -1.50 eV and -1.51 eV for those sulfur doped graphene without and with Stone-Wales defects, respectively, which are close to the experimental value ($\Delta G = 1.40$ eV) in standard states [213]. For the four electron transfer pathway on the sulfur doped graphene without and with defects, overall reaction $O_2 + 4H^+ + 4e^- \rightarrow 2H_2O$, calculated values of ΔG are -4.99 eV and -4.90 eV, which are also close to the experimental results ($\Delta G = -4.92$ eV) in standard states [211]. Thus, both two and four electron transfer processes could simultaneously occur on these sulfur doped graphene, and the number of electron transfer could be between 2 and 4. This conclusion is consistent with the experimental results that show the number of transferred electron ranging from2.51 to 3.82 for the sulfur doped graphene [207].

HOMO LUMO HOMO LUMO

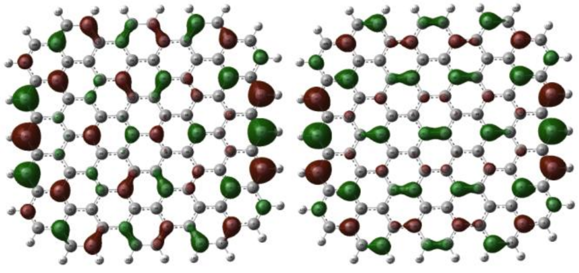

Pure GN, $C_{100}H_{26}$

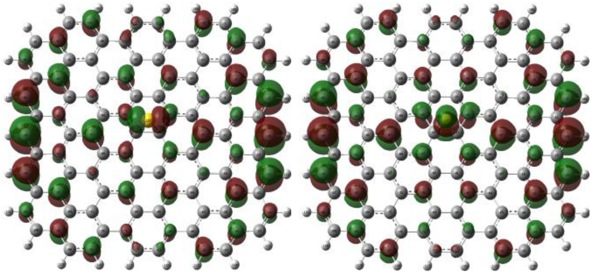

S-adsorbed GN, $C_{100}H_{26}S$

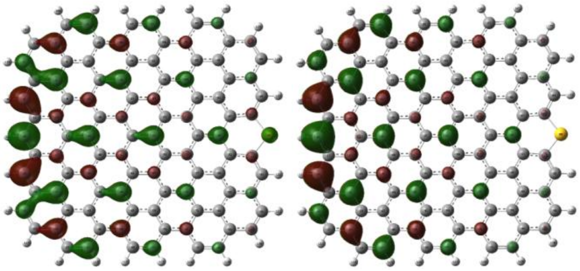

Edge S-substituted GN (zigzag), $C_{99}H_{25}S$

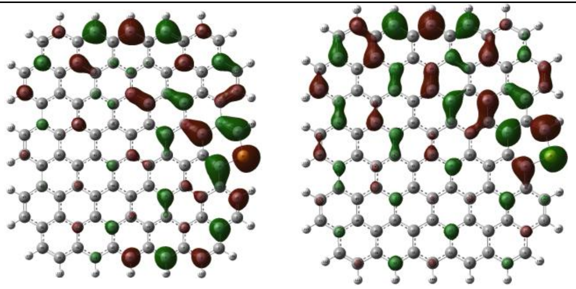

Edge S-substituted GN (armchair), $C_{99}H_{25}S$

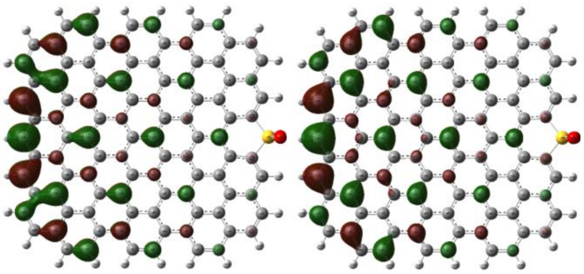

Edge SO_2-substituted GN (zigzag), $C_{99}H_{25}O_2S$

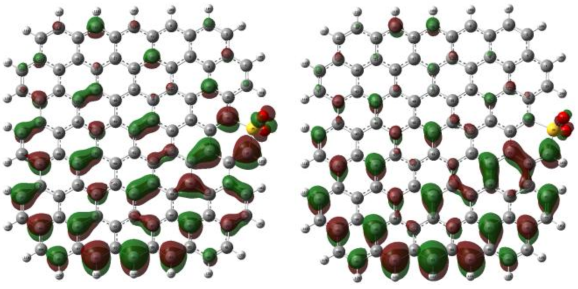

Edge SO_2-substituted GN (armchair), $C_{99}H_{25}O_2S$

HOMO LUMO

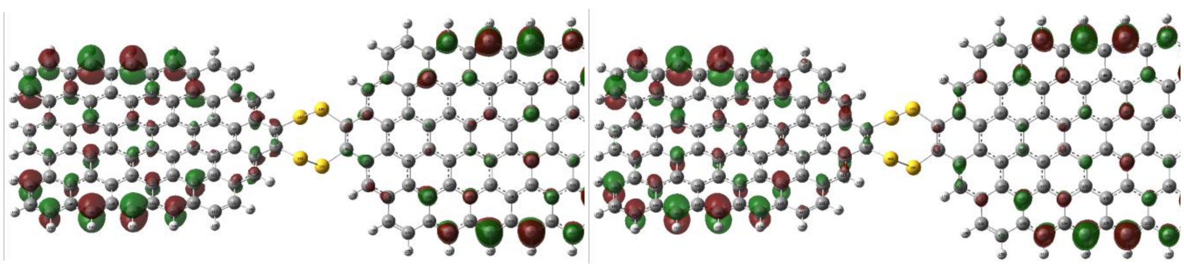

S-ring clustered GN, $C_{144}H_{40}S_4$

Figure 4-16 HOMO and LUMO distribution on graphene and sulfur doped graphene (GN)

The above results have shown that catalytic active sites usually located at the zigzag edge or neighboring carbon atoms close to the sulfur oxide. This could be explained by the highest occupied molecule orbital (HOMO), and the lowest unoccupied molecule orbital (LUMO) distributions on the graphene. Figure 4-16 shows the HOMO and LUMO distributions on these pure and sulfur doped graphene. For the pure graphene, the HOMO and LUMO distributions show little local polarization. However, for these graphenes with sulfur adsorbed on their surface, and sulfur/ sulfur oxide doped at their edge, the HOMO and LUMO distributions show relatively large local polarization in different degree. The area with large local polarization coincides with the sites with larger spin or charge density, which show four-electron catalytic activity for ORR. It is noticed that Stone-Wales defects enhance the HOMO and LUMO local polarization and therefore facilitate the ORR catalytic activation the sulfur doped graphene.

4.4 Conclusions

The DFT method was used to study the mechanism of ORR on the N-graphene, the effect of nitrogen-doping structure and Stone-Wales defects on ORR in fuel cells. The simulation results on the electron transformation process show that the ORR is four-electron pathway on the N-graphene but pure graphene does not have such catalytic activities. When H is introduced into the system, the sequential reactions can occur, including the formation of O-C chemical bond between oxygen and graphene, O-O bond break, and creation of water molecules. For each reaction step, the system energy decreases accordingly, indicating that the four-electron transformation reaction takes place spontaneously. The catalytic active sites on the N-graphene depend on spin density distribution and atomic charge distribution. The substituting nitrogen atom introduces no-pair electrons to the graphene and change the atomic charge distribution on it. Generally, the carbon atoms which possess highest spin density are the electrocatalytic active catalytic sites. If the negative value of spin density is small, the carbon atoms with large positive atomic charge density may act as the active sites. For the simulation of effect of nitrogen doping structure and Stone-Wales defect on ORR, the results revealed that dopant-induced redistribution of spin density and charge density on the graphene strongly affect the formation of the intermediate molecules in ORR, including OOH, or O_2 adsorption, O-O bond break and water formation. With increasing the number of nitrogen dopants from one to four in cluster, the number of active sites per doping atom reaches to maximum at N=2 and then reduce, indicating that catalytic ability of nitrogen in larger cluster is weaker than that of single nitrogen or small cluster in terms of the number of catalytic sites available. The defects enhance the catalytic capability of the graphene by changing the HOMO-LUMO energy gap and reaction pathways. For four-electron transfer, the predicted effective reversible potential for N-doped graphene is in the range of 1.04~1.15V/SHE with an average value of 1.10V/SHE, which is consistent with the experimental results. Engineering materials structures can promote catalytic capability of graphene by introducing small N clusters in combination with materials defects.

For the sulfur doped graphene being the catalyst of ORR of fuel cells, four types of sulfur-doping structures, surface S-adsorbed, edge S-substituted, edge SO_2-substituted, and sulfur-ring clustered graphenes, were proposed based on the experimental results [207, 208, 210]. The formation energy, electronic structures as well as ORR catalytic activities were calculated via DFT methods. Among these doping structures, surface sulfur adsorbed is more stable in terms of energy formation. The active catalytic sites on these S-doped graphene are those carbon atoms located at the zigzag edges or close to SO_2 doping structure, which possess high positive charge density or spin density. Both two-electron and four-electron transfers can occur simultaneously over the S-doped graphene structures. Two-electron transfer pathways proceed on the sulfur atom being the catalytic active sites with high charge density while four-electron transfer takes place on the carbon atoms with high positive spin or charge density. The Stone-Wales defects facilitate the formation of surface S-adsorption on graphene as well as the catalytic activities of sulfur-doped graphene, especially for those with sulfur adsorbing on the surface. Sulfur adsorbing/substituting and clustering make the graphene more locally polarized in HOMO and LUMO distribution at the zigzag edges and near the SO_2 doping sites of the graphene, which leads to enhanced catalytic activities at the edges.

CHAPTER V

ROLE OF POINT AND LINE DEFECTS IN CATALYTIC PROPERTY OF GRAPHENE FOR FUEL CELLS

In this chapter we study the effect of defects in ORR catalytic property of graphene for fuel cells. Defects include zero dimentional Stone-Wale, single vacancy, bi-vacancy, substituting pentagon carbon ring at zigzag edge defects and one dimentional, fused pentagon-pentagon-octagon chains, and pentagon-heptagon chain defects. Electronic properties of these graphenes containing defects are explored. ORR potential catalytic active sites are confirmed, and the ORR pathways are simulated.

5.1 Models and methods

Two types of graphene models with defects were built based on experimental observation. One is the graphene containing zero dimensional defects, which includes Stone-Wales defects, vacancies with one or two carbon atom missing at the center [214], pentagon carbon rings substituting hexagon carbon rings at zigzag edge. The other is the graphene with grain boundaries, which are pentagons-heptagons connecting chain [215] and composed of octagons and fused pentagons. Unlike other point defects, a Stone-Wales (SW) defect does not involve any removed or added atoms. Four hexagons are transformed into two pentagons and two heptagons (SW-5577) by rotating one of the C-C bonds by 90˚, o Figure 5-1 (b). Single vacancy (SV) by missing one carbon atom has been experimentally observed by TEM [49, 50] and STM [53], as shown in Figure 5-1 (c). Double vacancies [58, 60] (DV) can be created either by the coalescence of two SVs or by removing two neighboring atoms, so two pentagons and one octagon appear instead of four hexagons in perfect graphene, as shown in Figure 5-1(d). In addition, when one atom is missing at zigzag or armchair edges of graphene, a pentagon is formed by reconstructing these edges. Figure 5-1 (e) shows a pentagon ring at a zigzag edge. One dimensional defect, also called line defects, can be thought of as a line of reconstructed point defects. One line defect is a line of alternative pairs of pentagons separated by octagons (GLD-558), as shown in figure 5-1(f) and (g). The other 1D defect consists of pentagons and heptagons (GLD-57), shown as figure 5-1(h) and (i). There is odd number of octagon or heptagon rings on line defect for (f) and (i) but even number of octagon or heptagon rings on it for (g) and (h). These line defects have been observed in experiments [216-219] and theoretical simulation methods [220, 221].

The ORR process pathways over the perfect and defective graphene as catalysts in acidic environment were simulated using the DFT. The method is similar as described in 4.1.1 method of chapter four. OHH or O_2 molecule was set near the graphene plane at a distance of 1.5~3.0 Å, and then observe if it adsorbs at the possible catalytic active sites. After the first electron transformation, the succeeding electron transforming was simulated by continuing to add H atoms in the system. For each step, we obtained the optimized structure, and calculated the reaction free energy ΔG.

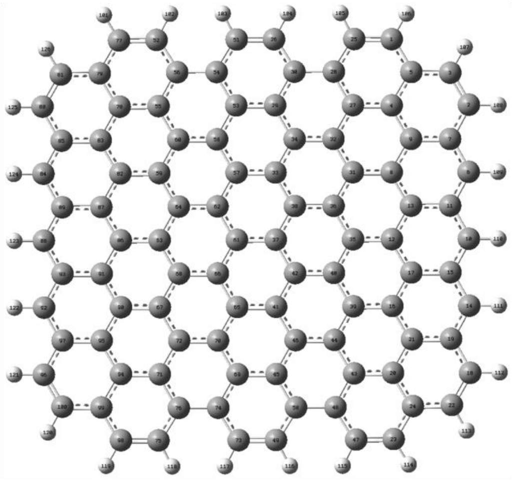

(a)

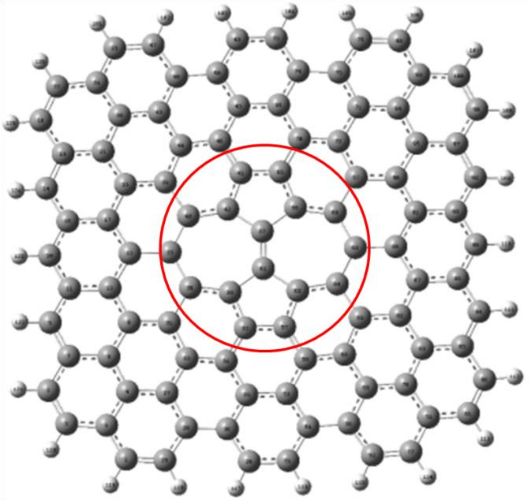

(b)

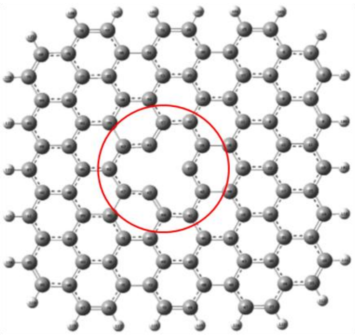

(c)

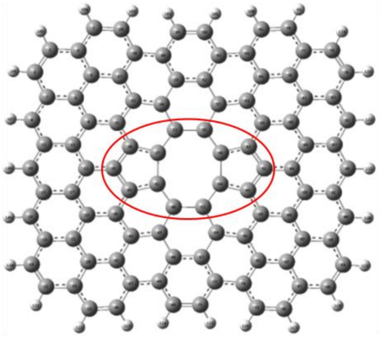

(d)

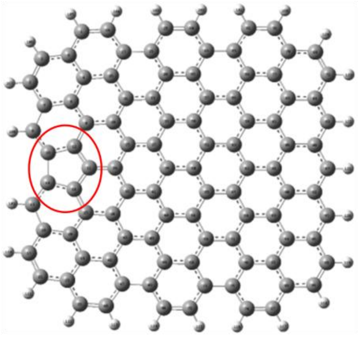

(e)

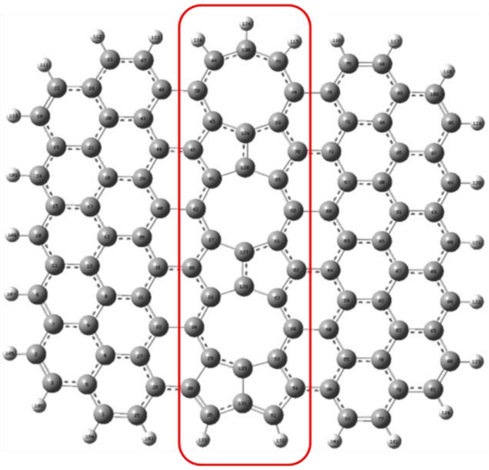

(f)

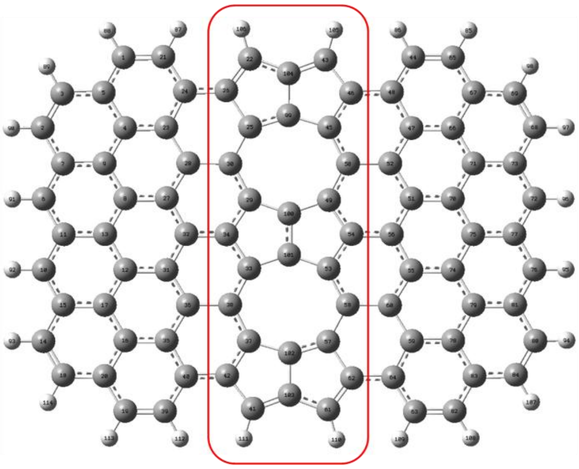

(g)

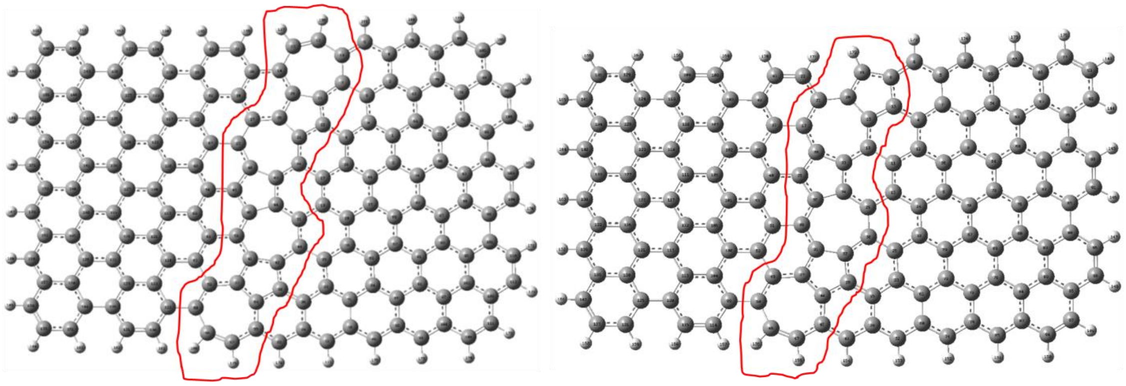

(h) (i)

Figure 5-1 Perfect and defective graphenes. (a) Perfect graphene, (b) Stone-Wales defect (SW), (c) Single vacancy (SV), (d) Double vacancies (DV), (e) Edge defect with pentagon ring at zigzag edge (PZ), Octagon and fused pentagon carbon rings line defect with (f) odd number of octagon rings (GLD-558-01) and (g) even number of octagon rings (GLD-558-02), and Pentagon-heptagon pairs line defects with (h) even number of heptagon ring (GLD-57-01) and (i) odd number of heptagon ring (GLD-57-02).

5.2 Results and discussion

5.2.1 Spin and charge distribution on graphene containing defects

The electronic structure of the perfect and defective graphene sheets was determined and its effect on catalytic property was analyzed. Since those carbon atoms with high spin or charge density are most likely to be catalytic active sites[222, 223], we have calculated spin and charge distributions on these defective graphenes, shown in figure 5-2. There is no spin density for those perfect and defective graphene with SW, SV, DV point defects and line defect structures GLD-558, GLD-57 containing even number of octagon and heptagon carbon rings. The distribution of charge density on SW, SV, DV is similar with that of perfect graphene. Atoms with higher charge density distribute at the zigzag edge, and the maximum value is less than 0.20, as shown in figure 5-2 (a) and (b). Figure 5-2 (c) - (h) show the spin and charge density on the graphene with pentagon ring at zigzag edge PZ, GLD-558-01 and GLD-57-02 line defects. For the pentagon ring, the high spin density appears at the zigzag edge opposite to the pentagon ring (e.g., C #87: 0.41, C #83: 0.27 in Figure 5-2c) while high charge density distributes at two zigzag edges. For GLD-558-01 structure, the atom obsessing the highest spin density (0.41) locates in the octagon ring at the armchair edge. The high charge density distributions are more complex with a value of about 0.20, but mainly spread along zigzag edges, and octagon rings. For GLD-57-02 structure, the atom with higher spin density locates at zigzag edge (e.g. C#138: 0.44, C#139 and 140: 0.36) and the higher charge density distributes at zigzag sections of edge, the value of them is less than 0.22.

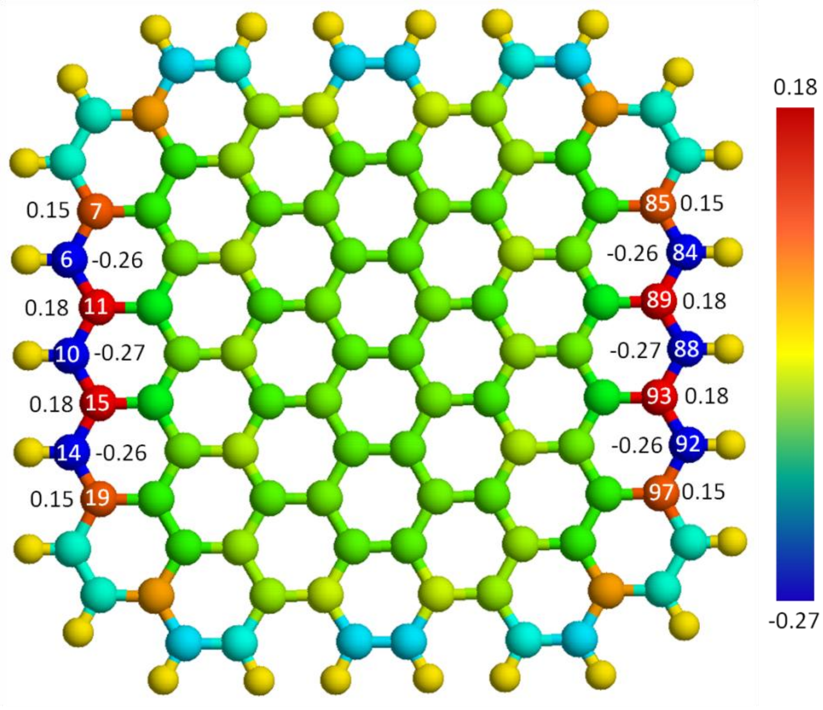

(a)

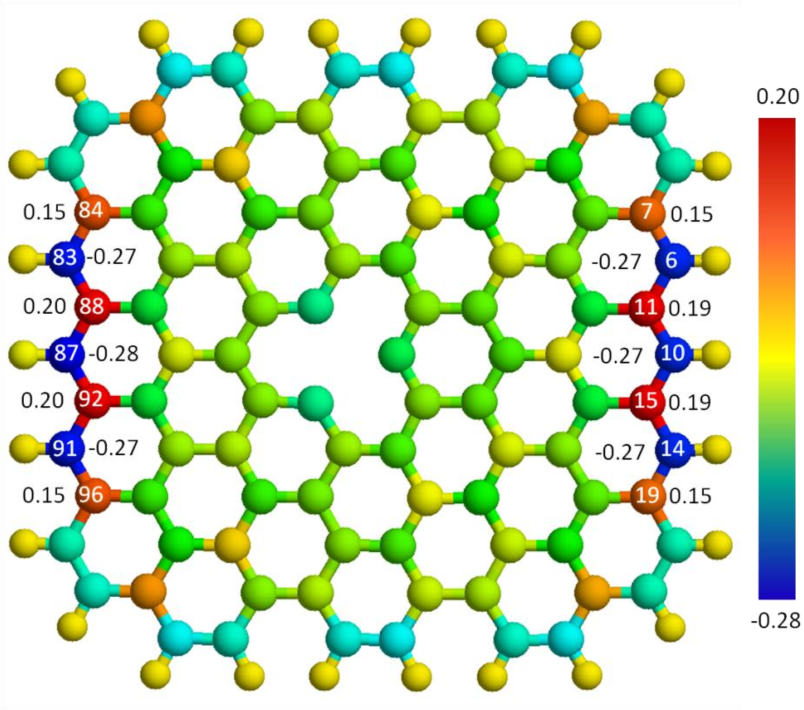
0.20
-0.28
0.15
84
83
-0.27
0.20
88
87
-0.28
0.20
92
91
-0.27
0.15
96
7
0.15
-0.27
6
11
0.19
-0.27
10
15
0.19
-0.27
14
19
0.15

(b)

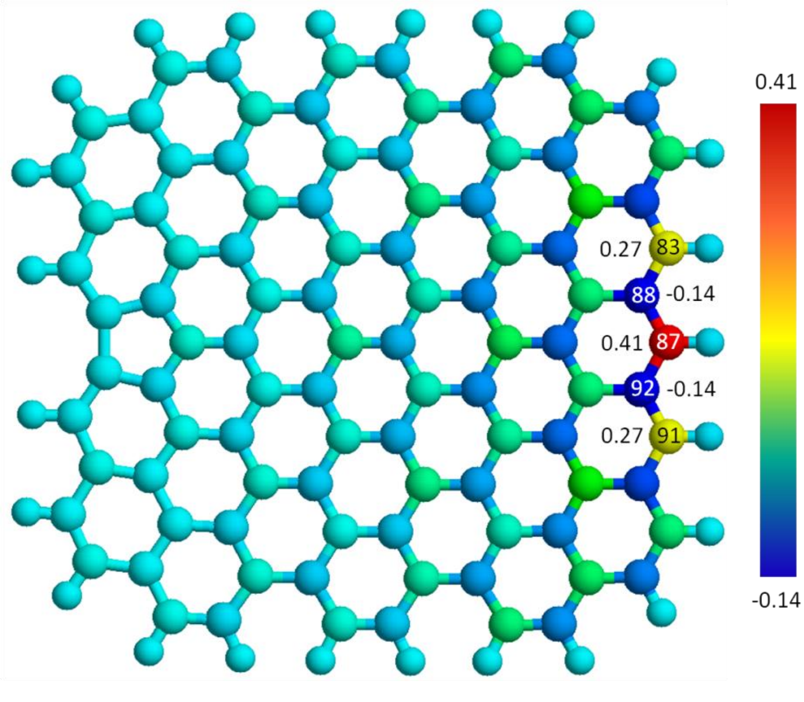
0.41
-0.14
0.27
83
88
-0.14
0.41
87
92
-0.14
0.27
91

(c)

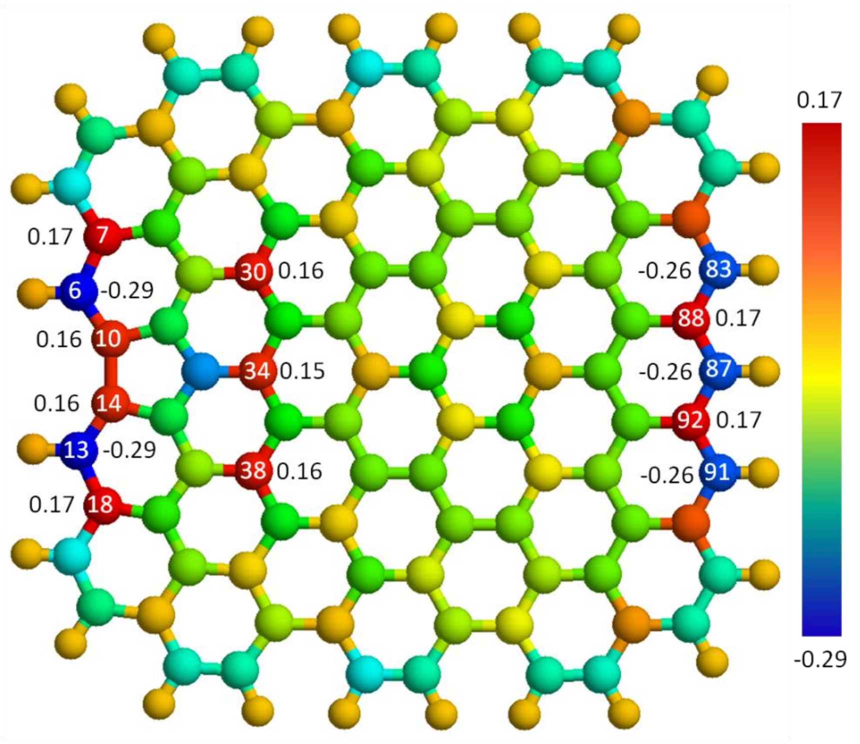
0.17
7
6
-0.29
30
0.16
0.16
10
34
0.15
0.16
14
13
-0.29
38
0.16
0.17
18
-0.26
83
88
0.17
-0.26
87
92
0.17
-0.26
91
0.17
-0.29

(d)

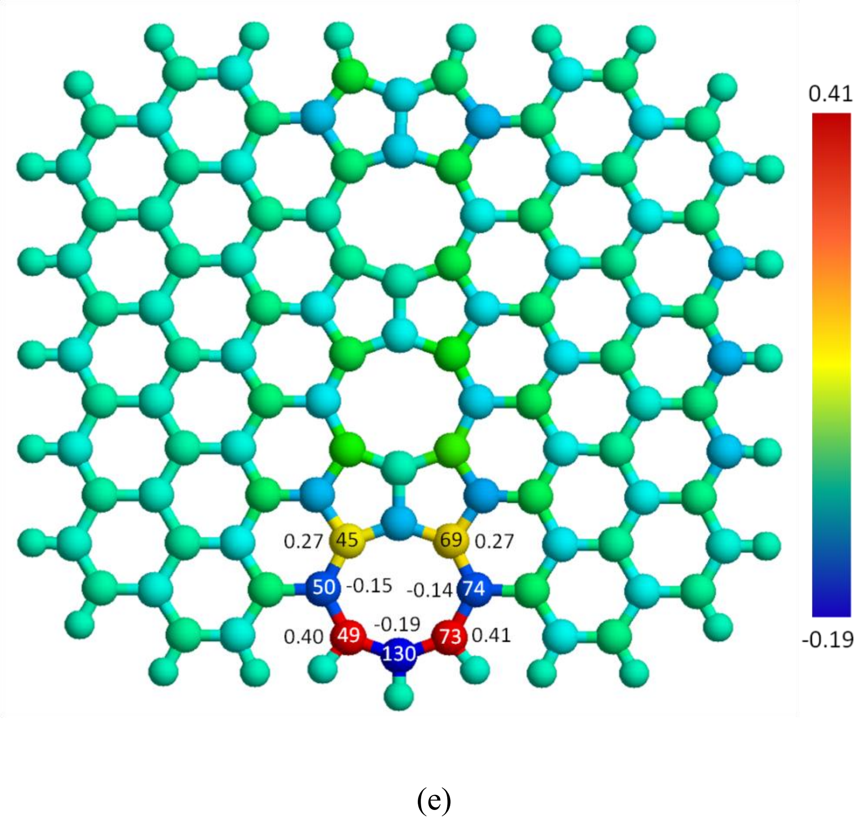
0.41
0.27
45
69
0.27
50
-0.15
-0.14
74
0.40
49
-0.19
130
73
0.41
-0.19

(e)

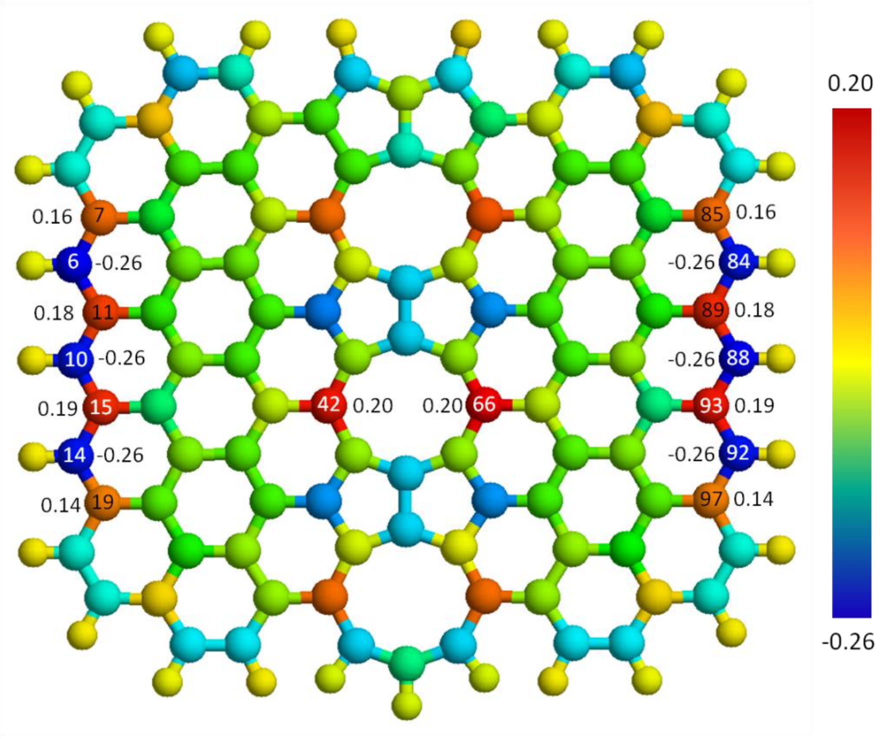
0.20
0.16
7
85
0.16
6
-0.26
-0.26
84
0.18
11
89
0.18
10
-0.26
-0.26
88
0.19
15
42
0.20
0.20
66
93
0.19
14
-0.26
-0.26
92
0.14
19
97
0.14
-0.26

(f)

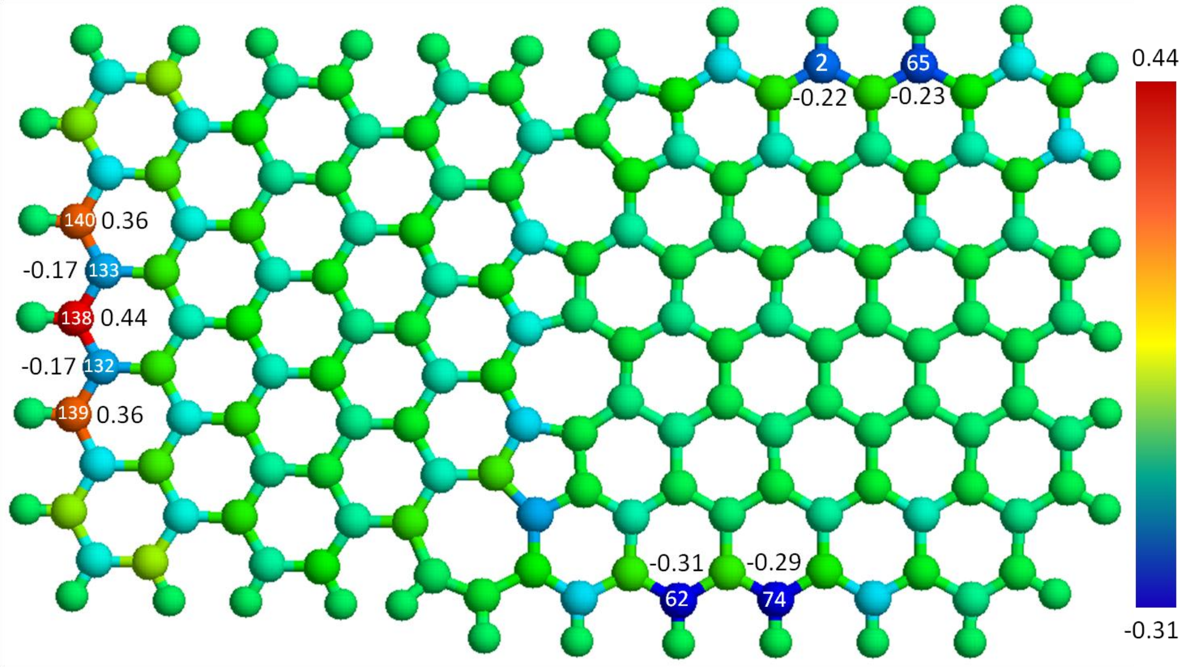
2
65
-0.22
-0.23
0.44
140
0.36
-0.17
133
138
0.44
-0.17
132
139
0.36
-0.31
-0.29
62
74
-0.31

(g)

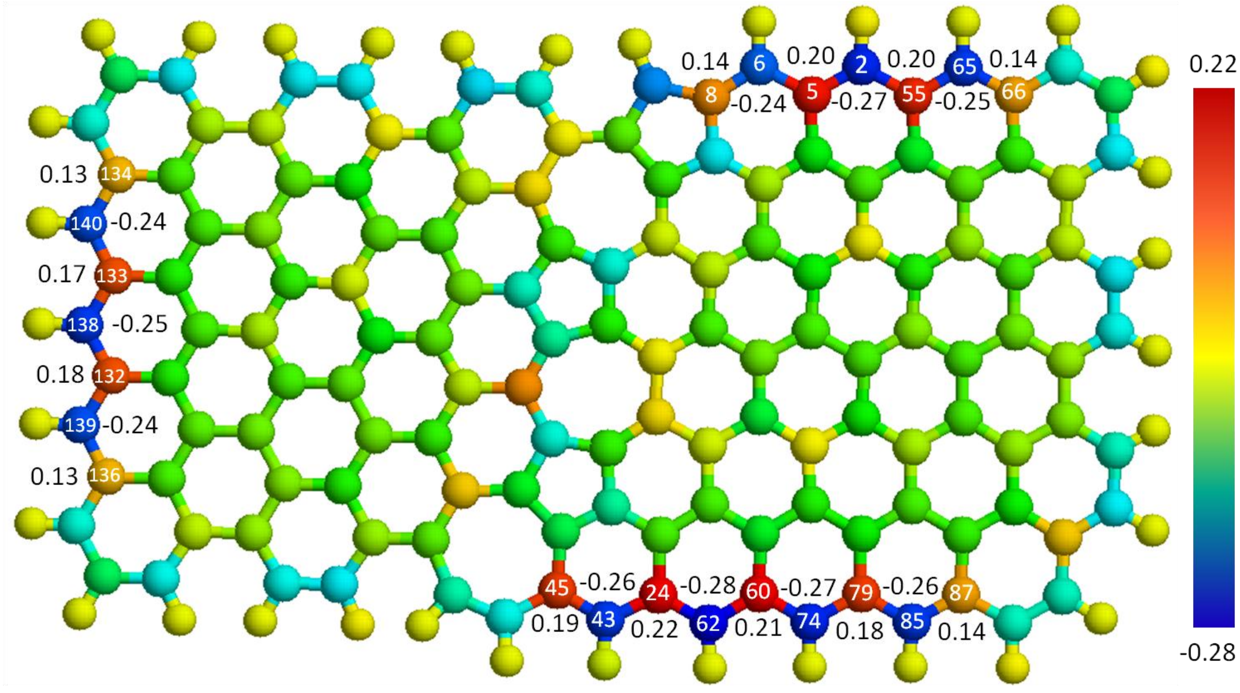

(h)

Figure 5-2 Charge and spin density distribution on perfect graphene and defective graphenes. (a), (b), (d), (f) and (h) are charge density distribution on perfect, SV, PZ, GLD-558-01 and GLD-57-02 graphenes, respectively, while (c), (e) and (g) show spin density distribution on PZ, GLD-558-01 and GLD-57-02 graphenes, respectively. The color on the circle stands for different value, which is decrease in the color order red, orange, yellow, green, and blue.

5.2.2 ORR paths on defective graphene

OOH/O_2 adsorbing on the catalytic active sites is the first electron transfer in ORR, and decisive step for a material to show catalytic capability. The catalytic capability of the defective graphene has been examined by introducing OOH or O_2 molecule over the atoms with high spin or charge density in a distance of 1.5- 3.0 Å. For the graphene structures with point defects, OOH or O_2 molecules cannot adsorb on these carbon atoms except for the pentagon ring. As shown in Figure 5-3(a), for the pentagon ring, OOH covalently bonds to the carbon atom #87 with highest spin density, with a C-O bond length of 1.45Å. Therefore, among these point defects, only pentagon structure shows the catalytic activities for ORR. For line defects, OOH/O_2 molecule can adsorb on the carbon atoms with spin density higher than 0.25 for GLD-588-01 and GLD-57-02 grain boundaries. Thus, the graphene with pentagon carbon ring at zigzag edge or GLD-558-01 and GLD-57-02 grain boundaries promote the first step of ORR and could be catalytically active.

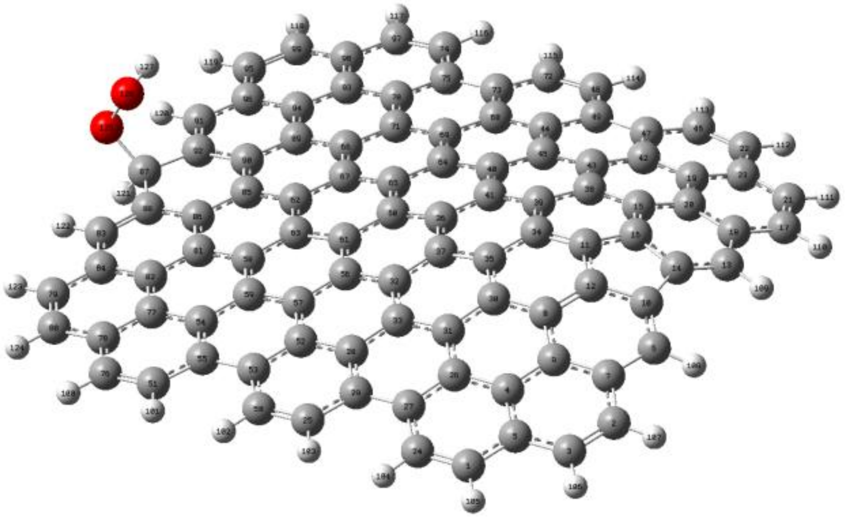

(a)

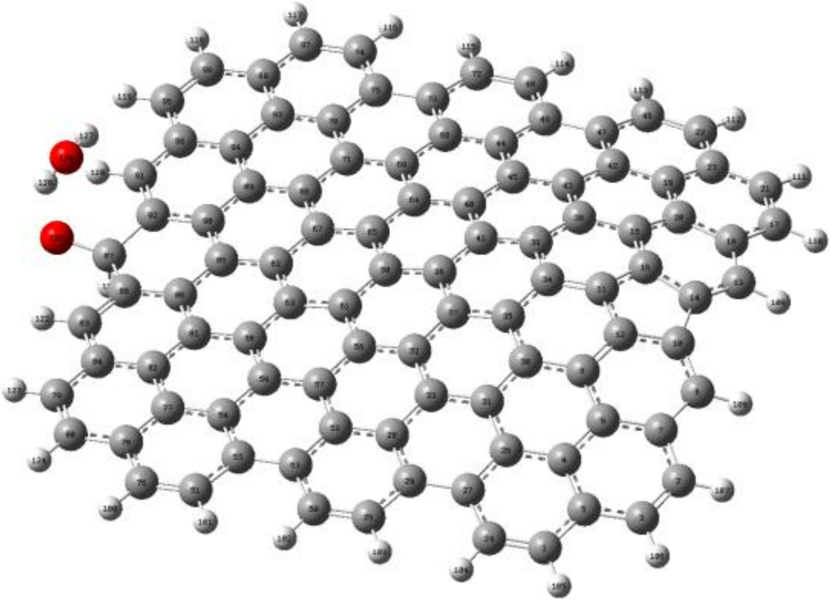

(b)

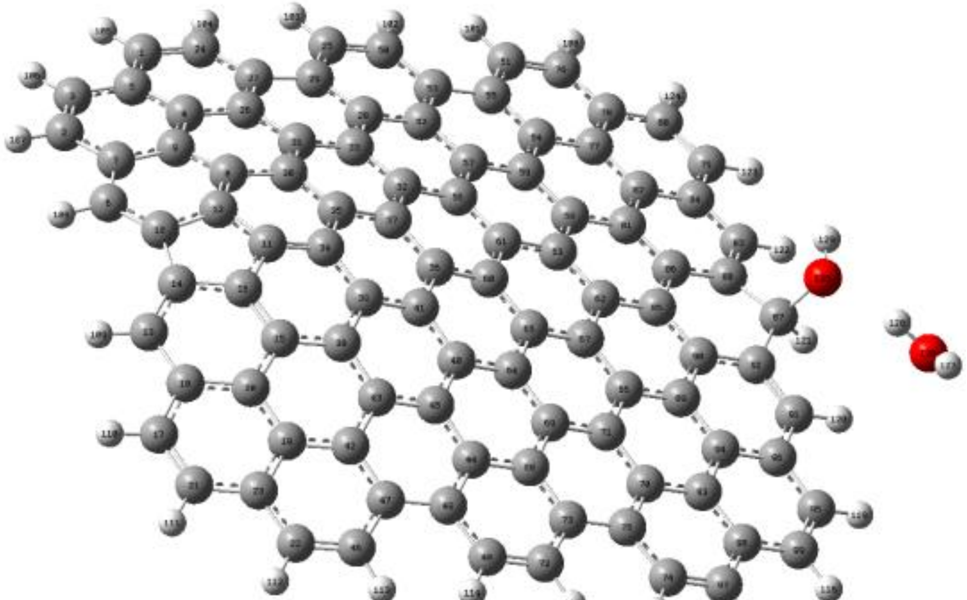

(c)

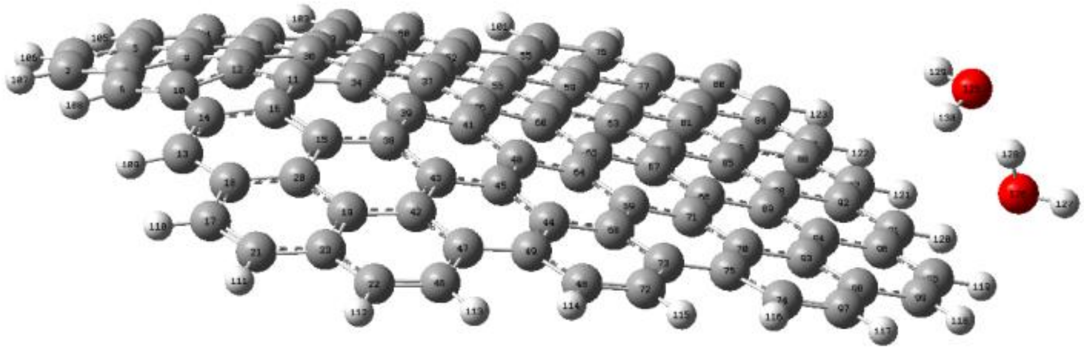

(d)

Figure 5-3 ORR processes on graphene with pentagon carbon ring at zigzag edge: (a) OOH adsorbed on carbon atom, (b) O-O bond breakage, and a water molecule formed, (c) OH molecule formed, and (d) two water molecules departing from graphene surface.

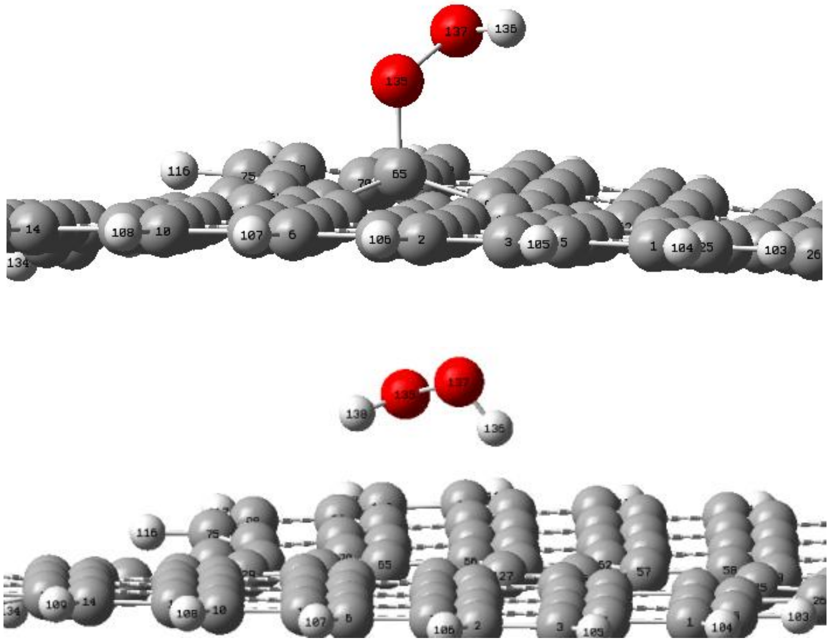

Figure 5-4 Two-electron transfer processes of ORR on graphene with pentagon-pentagon-octagon chains (GLD-558-01): (a) OOH adsorbed on carbon atom #65, and (b) H_2O_2 molecule formed and departing from the graphene surface.

After the first electron transfer, subsequent electron transfer reactions were determined by introducing protons into the system. When a H atom was introduced near to the adsorbed OOH, it bonded to an oxygen atom, resulting in rupture of O-O bond, and the formation of one water molecule while the other oxygen atom still adsorbs on the graphene, as shown in Figure 5-3(b). As mentioned above, the breakage of O-O bond is the key step of four electron transfer, which defines the process being four electron transfer pathway. When two more H atoms were sequentially introduced into the system, an OH first forms, followed by the generation of another water molecule, shown in Figure 5-3(c) and (d). These water molecules then depart from the graphene surface and the graphene recovers to its original state ready for another cycle of catalysis. The overall ORR on GLD-558-01 and GLD-57-02 structures follow the similar process as described above. In addition to the four electron transfer pathway, we also found the two electron transfer reactions on GLD-558-01. When the first electron transfer process finished, O_2 or OOH adsorbed on the carbon atoms such as #61, #65 which possess relatively lower spin density (0.10~0.13). For the two electron transfer reaction, when another H atom was introduced near to the adsorbed OOH, it bonded to the oxygen atom bonding to the carbon atom on the graphene forming a H_2O_2 molecule. The reaction processes are show in figure 5-4 (a) and (b). So for these graphene containing point and line defects showing catalytic property, four-electron transfer and two-electron transfer reactions are exist simultaneously on them.

Although the defects that facilitate the four-electron transfer are observed in graphene, the electrocatalytic activities of defective graphene measured in the experiment are still much low compared to hetero-element-doped graphene (e.g., N-doped graphene)

[7]. The number of electron transfer for graphene is around 2.-2.5 [224], indicating that two-electron transfer dominates the ORR on the undoped graphene. From the analysis above, all the structures that are active in four-electron transfer containing pentagon rings at single edge of the graphene. These structures are able to introduce both high spin density and charge density at the carbon atoms, facilitating four-electron transfer. The catalytic mechanism is the same as nitrogen doping [29]. Thus, the introduction of more pentagon rings at the edges of graphene could significantly improve the catalytic activities of the graphene.

Table 5-1 R o f gy ΔG (V) of fou d o -electron transfer pathways of ORR on graphenes containing point and line defects.

Reaction pathways		Point defect (ZP)	Line defect (GLD-558-01)
Four electron transfer	$O_2 + H^+ + e^- \rightarrow {}^*OOH$	-1.20	-1.29
	$^*OOH + H^+ + e^- \rightarrow {}^*O + H_2O$	-0.93	-1.24
	$^*O + H^+ + e^- + H_2O \rightarrow {}^*OH + H_2O$	-2.01	-1.35
	$^*OH + H^+ + e^- + H_2O \rightarrow 2H_2O$	-0.62	-1.09
	Overall: $O_2 + 4H^+ + 4e^- \rightarrow 2H_2O$	-4.76	-4.97
Two electron transfer	$O_2 + H^+ + e^- \rightarrow {}^*OOH$	—	-0.15
	$^*OOH + H^+ + e^- \rightarrow H_2O_2$	—	-1.18
	Overall: $O_2 + 2H^+ + 2e^- \rightarrow H_2O_2$	—	-1.33

R o f gy ΔG of bov l o f o p o calculated for the structures with a pentagon carbon ring at zigzag edge and a GB-558-01 grain boundary. Values of the free energy for electron transfer pathways are listed in Table 5-1. For the overall ORR: $O_2 + 4H^+ + 4e^- \rightarrow 2H_2O$, the reaction free energy for the graphene with point and line defects are -4.76 eV and -4.97 eV, respectively, comparable to -4.92 eV measured in experiments [225]. For two-electron transfer ORR: $O_2 + 2H^+ + 2e^- \rightarrow H_2O_2$, the reaction free energy is -1.33 eV, which is approximate to experimental value -1.40 V [6] . Fo l o f o, ΔG g v o d f v graphenes, indicating that these sub-reactions could occur spontaneously. Comp d ΔG of four electron transfer sub-reactions on point-defect and line-defect graphene, the v lu of ΔG fo l -defect are closer to the even value 1.23 eV [226]. Thus, the four-electron transfer process of ORR would be more efficient for the line-defect graphene.

Highest occupied molecular orbital (HOMO) and lowest unoccupied molecular orbital (LUMO), also called frontier orbitals are closely related to bond forming and breaking during chemical reaction. The shapes of the HOMO and LUMO map provide a qualitative presentation of molecular properties and reactivity. The HOMO provides the most reactive electrons part while the LUMO offers the more relevant reactivity with molecules that have negative charge. Mixing an unusually high HOMO with an unusually low LUMO can lead to bond formation between two molecules. The HOMO and LUMO distributions for perfect graphenes and the graphene with a pentagon ring at zigzag edge and a GB-558 line defect in the middle of graphene plane were calculated and the results are shown in Figure 5-5. Obviously, the HOMO or LUMO distributions are polarized on the graphene with these two kinds of defects. The HOMO of alpha electron of the two defective graphenes has the similar energy level with the LUMO of adsorbed OOH or O_2. So OOH or O_2 can easily adsorb on the area with higher polarized HOMO, which are exactly the locations of active sites. Thus, the HOMO and LUMO distribution shapes further confirm the location of catalytic active sites determined on the defective graphene on the basis of spin and charge density distributions.

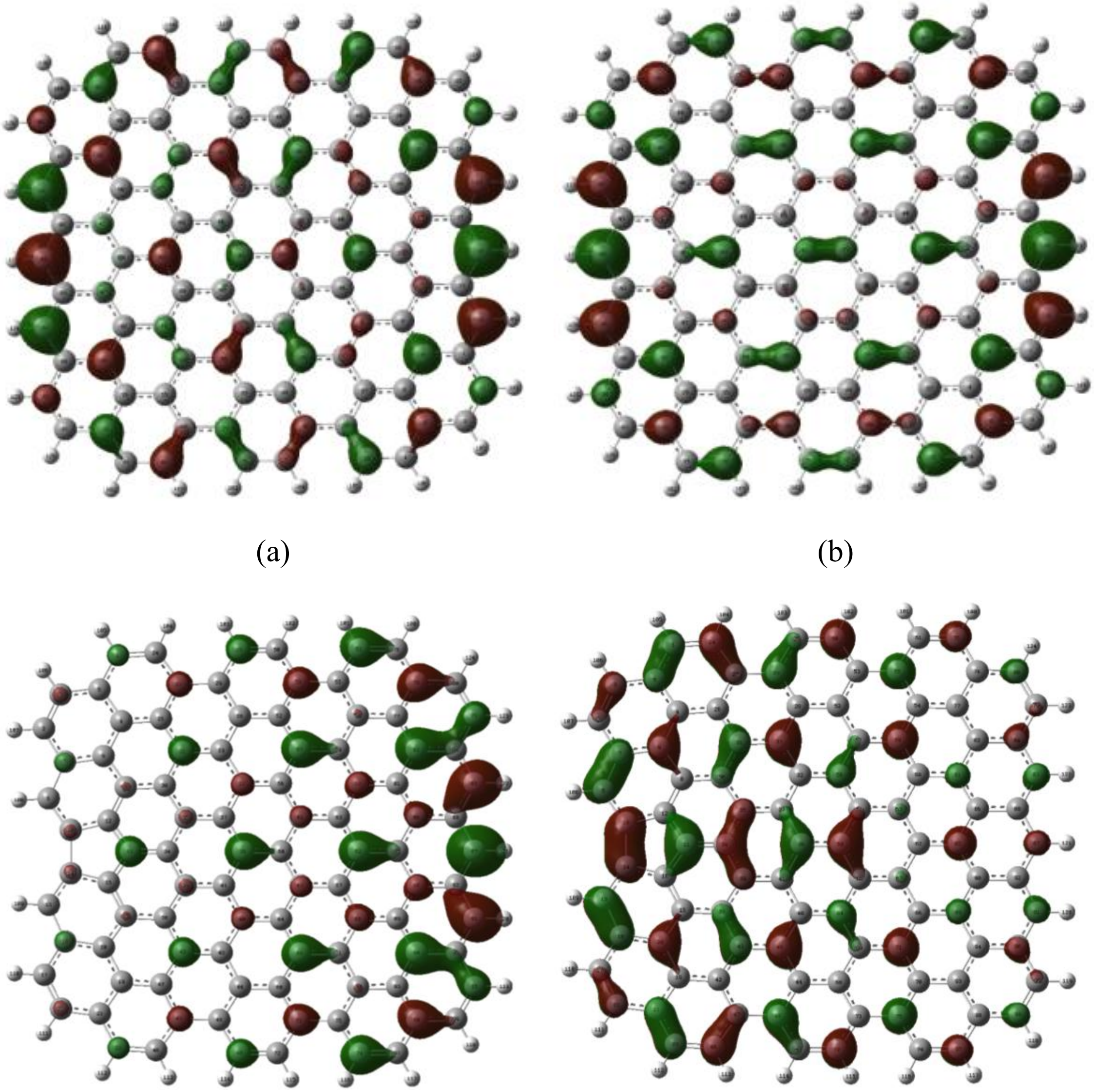

(a) (b)

(c) (d)

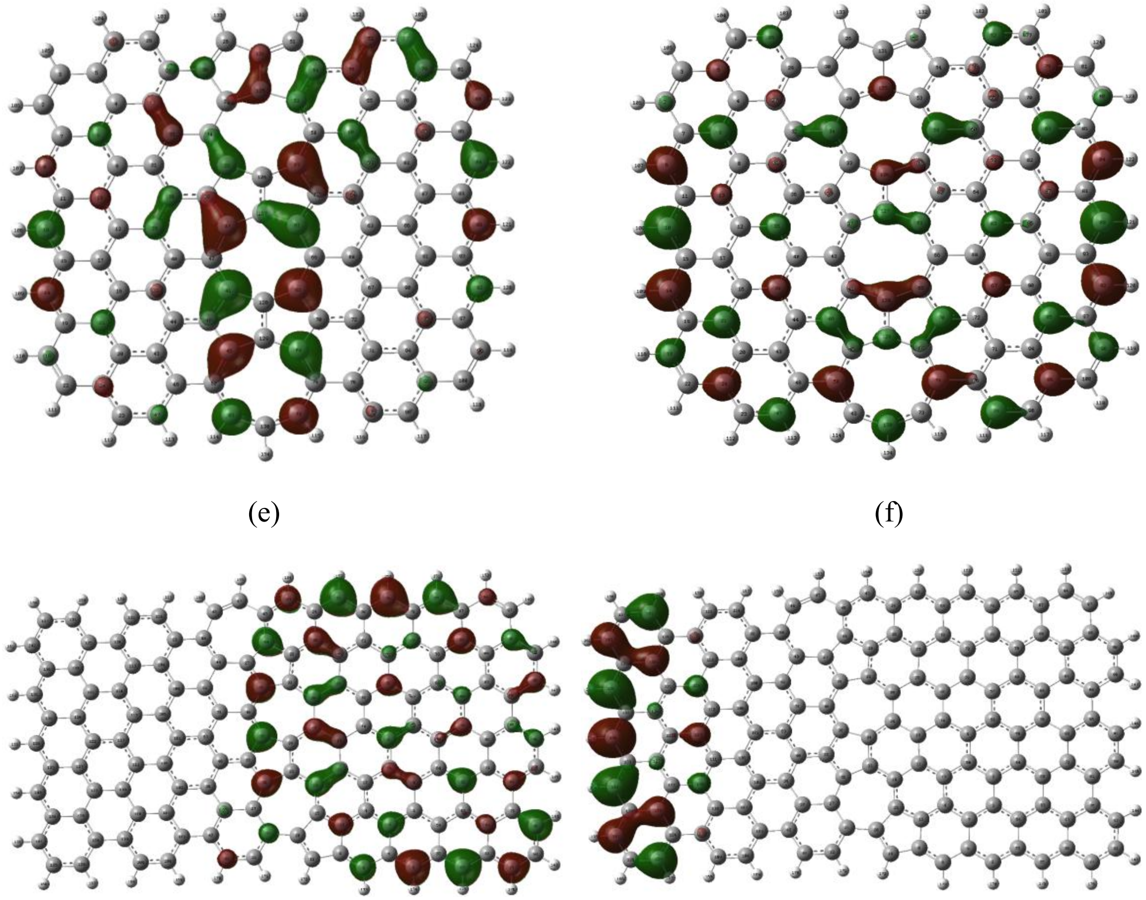

(e) (f)

(g) (h)

Figure 5-5 HOMO and LUMO distribution on perfect graphene and the graphene with point and line defects: (a) HOMO and (b) LUMO of perfect graphene, (c) HOMO and (d) LUMO of PZ, (e) HOMO and (f) LUMO of GLD-558-01, (g) HOMO and (h) LUMO of GLD-57-02.

5.3 Conclusions

The effect of point- and line-defects in graphene on the catalytic activities was studied using DFT methods. Among the point defects including Stone-Wale defect, single vacancy, double vacancies, and one substituting pentagon ring locating at zigzag edge, only pentagon ring induces high spin density and has catalytic capability. In one dimensional line defects such as pentagon-heptagon chain (GB-57) and pentagon-pentagon-octagon chain (GB-558), the structure containing odd number of heptagon or octagon carbon ring generates spin density and can catalyze ORR. For those graphenes showing catalytic activity for ORR, the catalytic active sites usually locate at zigzag edge or at end of the pentagon-pentagon-octagon chains. The four electron and two electrons ORR can occur on these defective graphenes simultaneously, and these sub-reactions are energetically favorable since the reaction free energy of sub-reaction is negative. HOMO and LUMO distributions are strongly polarized on the defective graphene and those most polarized are potentially the location of catalytic active sites.

CHAPTER VI

STRAIN EFFECT ON ORR CATALYTIC PROPERTY OF GRAPHENE IN FUEL CELLS

Strain effect on ORR catalytic properties of graphene is presented in this chapter. Strain applied on graphene can modify its electronic band structure and thus change its properties accordingly. We mainly explore the uniaxial strain effect for the catalytic properties of graphene. Strains along zigzag and armchair directions are applied on perfect graphene and nitrogen doped graphene. The electronic properties, such as HOMO-LUMO energy gap, HOMO energy level, spin and charge distributions on the graphene are studied. Based on the variation of electronic properties corresponding to strains, ORR pathways are simulated on these graphene with strains applying.

6.1 Introduction

Doping hetero atom on graphene is one of methods to modify its electronic properties. Strain effect can also modify graphene’s electronic properties. To date, strain effect on graphene has been studied both experimentally and theoretically in recent years. [227-236] Strain can be induced on graphene either intentionally or naturally. The uniaxial strain can be induced by bending the substrates on which graphene is elongated without slippage. And it can be quantitatively detected by Raman for its G band shift and splitting. [234, 236] Choi et al. [237] have carried out first principles calculations and theoretical analysis to explore the electronic structures of strained graphene and to understand its low energy electronic properties. They obtained that when a uniaxial or isotropic strain increased less than 26.2% along the zigzag direction, the semimetallicity was sustained. Beyond that, the system developed a small energy gap up to 45.5 meV at a strain of 26.5% and then closed its gap quickly. However, Gui et al. [227] using the first-principles pseudopotential plane-wave method and the tight-binding approach investigated the electronic structure of graphene under different planar strain distributions and obtained different results, which showed for the graphene with a strain along armchair direction, its band gap continuously increased to its maximum width of 0.486 eV as the strain increased up to 12.2%. For the graphene with a strain distribution along the zigzag direction, the band gap continuously increased only to its maximum width of 0.170 eV as the strain increases up to 7.3%. Wong et al. [238] using the first principle method explored strain effects on the electronic properties of single-layer graphene and they obtained that under strains (-12%~12%) its linear dispersion and gapless characters retained, but the Fermi velocity changed dramatically. Few studies based on the first-principle method have been considered for the strain effect on graphene, and the results are controversial. As far as I know, there is no study on the effect of strain applied on graphene on ORR catalytic properties for fuel cells.

6.2 Models and method

Graphene cluster $C_{100}H_{26}$ and nitrogen doped graphene $C_{99}NH_{26}$ were built, shown as Figure 6-1 (a) and (b). Uniaxial tensile or compress strain was applied along the zigzag and armchair directions on the graphene, respectively, which are shown as figure 6-1 (c-f). Uniaxial tensile strains of 1.0%, to 12.9%, compress strains of -2.0%, to -13.6% were gradually applied along zigzag direction on graphene $C_{100}H_{26}$. Along the armchair direction, tensile strains of 0.6% to 9.5%, and compressive strains of -0.6% to -16.6% were gradually applied on graphene $C_{100}H_{26}$. The same strains were also applied on nitrogen doped graphene $C_{99}NH_{26}$. T u x l d b d $\varepsilon_u = (L-L_0)/L_0$, where L and L_0 correspond to the deformed and undeformed unit lengths of graphene in zigzag and armchair directions. The highest occupied molecule orbital (HOMO) and lowest unoccupied molecule orbital (LUMO) energy gap, charge density and spin density distributions on the $C_{100}H_{26}$ and $C_{99}NH_{26}$ with different strains were calculated.

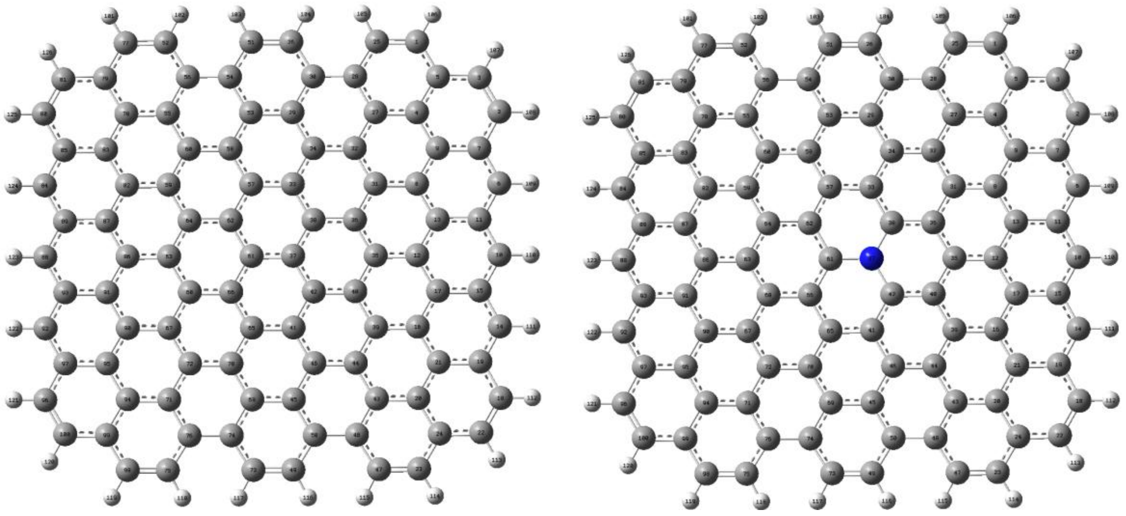

(a) (b)

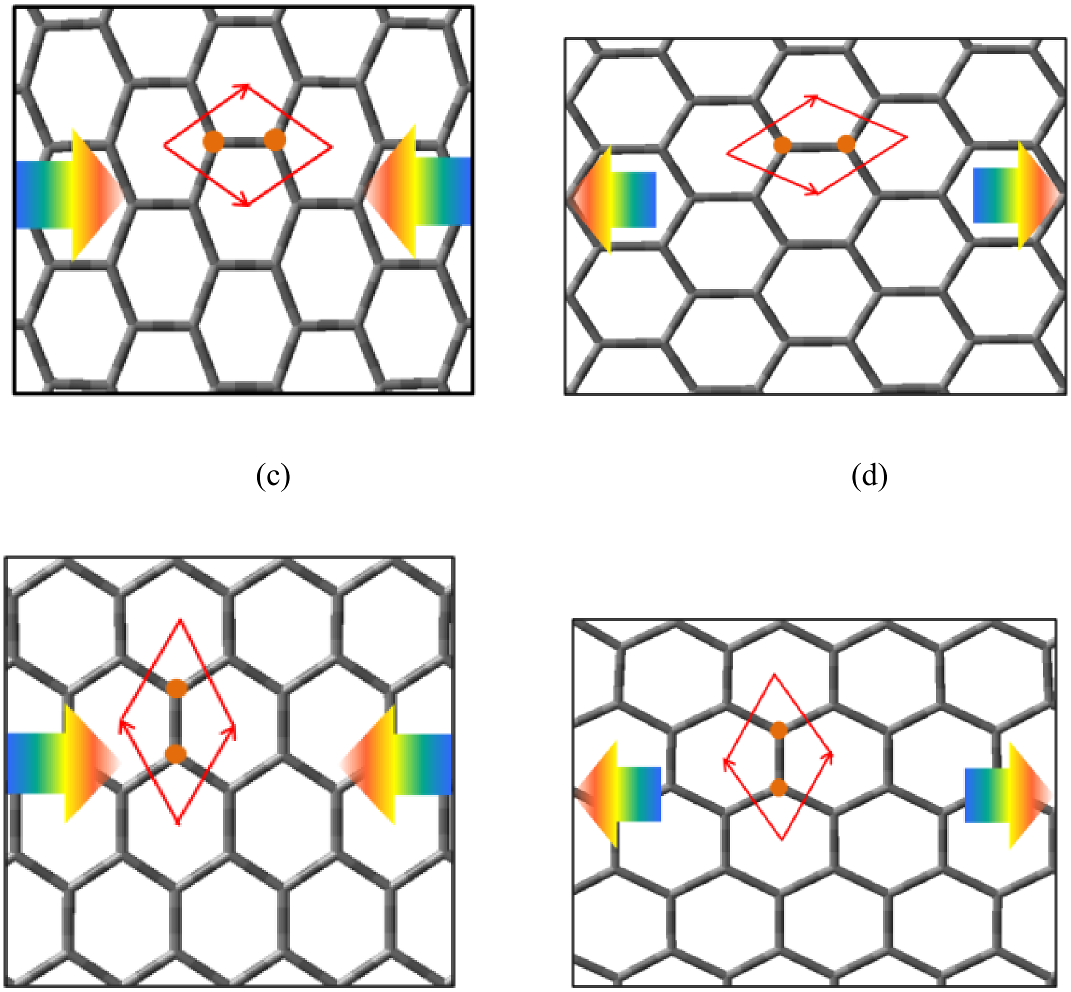

(c) (d)

(e) (f)

Figure 6-1 Graphene models and the way of applying strains: (a) graphene cluster $C_{100}H_{26}$, (b) nitrogen doped graphene $C_{99}NH_{26}$, (c) compress strain along armchair direction (CA-strain), (d) tesile strain along armchair direction (TA-strain), (e) compress strain along zigzag direction (CZ-strain), (f) tensile strain along zigzag direction (TZ-strain).

The ORR process pathways over graphene and nitrogen doped graphene with strain in acidic environment are simulated using DFT. The method is similar with that described in 4.1.1. We set OOH or O_2 molecule near the graphene plane at a distance of 1.5~3.0 Å, and then observe if it adsorbs at the possible catalytic active sites. After the first electron transformation, the succeeding electron transforming was simulated by continuing to add H atoms in the system. For each step, we optimized structure, and l ul d o f gy ΔG. Fo o g v o f energy, it would occur spontaneously.

6.3 Results and discussion

6.3.1 HOMO-LUMO energy gap and HOMO energy level

HOMO and LUMO energy gap is related to the conductivity of materials, and Fermi velocity depends on the HOMO energy level. Figure 6-2 shows the HOMO-LUMO energy gap and HOMO energy level of graphene $C_{100}H_{26}$ and nitrogen doped graphene $C_{99}NH_{26}$ with the applied strain along zigzag and armchair directions. Figure 6-2 (a) reveal the variation of HOMO-LUMO energy gap of $C_{100}H_{26}$ applying with different strains. It is obviously, the energy gap almost linearly decreases when the strain changes from the maximum uniaxial compressive strain to the maximum tensile in the zigzag direction while in armchair direction, it linearly increases. Therefore, TZ-strain improves the conductivity of graphene, but CZ-strain reduces the conductivity of graphene. Figure 6-2 (c) shows the variation of HOMO energy level of $C_{100}H_{26}$ as a function of zigzag and armchair strains. With increasing the zigzag direction strains from -15% to 5%, the HOMO energy level increase linearly while it decreases linearly with increasing the armchair direction strains from -5% to 10%. For the strain larger than 10%, whether it is tensile or compressive, with increasing the strain, the energy level decrease slightly. Thus, TZ-strain and CA-strain could make the graphene more reactive with other molecules. Considering the variation characters of HOMO-LUMO energy gap and

HOMO energy level of $C_{100}H_{26}$, we can conclude that TZ-strain and CA-strain could enhance conductivity and reactivity of mono-layer graphene, and hence are favorable to the ORR catalytic activities of graphene. Figure 6-2 (b), (d) are HOMO-LUMO energy gap and HOMO energy level versus strains applied on nitrogen doped graphene $C_{99}NH_{26}$. The armchair-direction strain applied on $C_{99}NH_{26}$ hardly affects its energy gap, so does the CZ-strain. However, with increasing the TZ-strain from 0 to 10%, the energy gap decreases linearly, suggesting that TZ-strain could improve the conductivity of nitrogen doped graphene. For the HOMO energy level, whether the strain is tensile or compressive along zigzag or armchair direction, with increasing the strains, they all make the nitrogen doped graphene more active in reactions. So for the nitrogen doped graphene, the applied TZ-strain could maximize the catalytic activity.

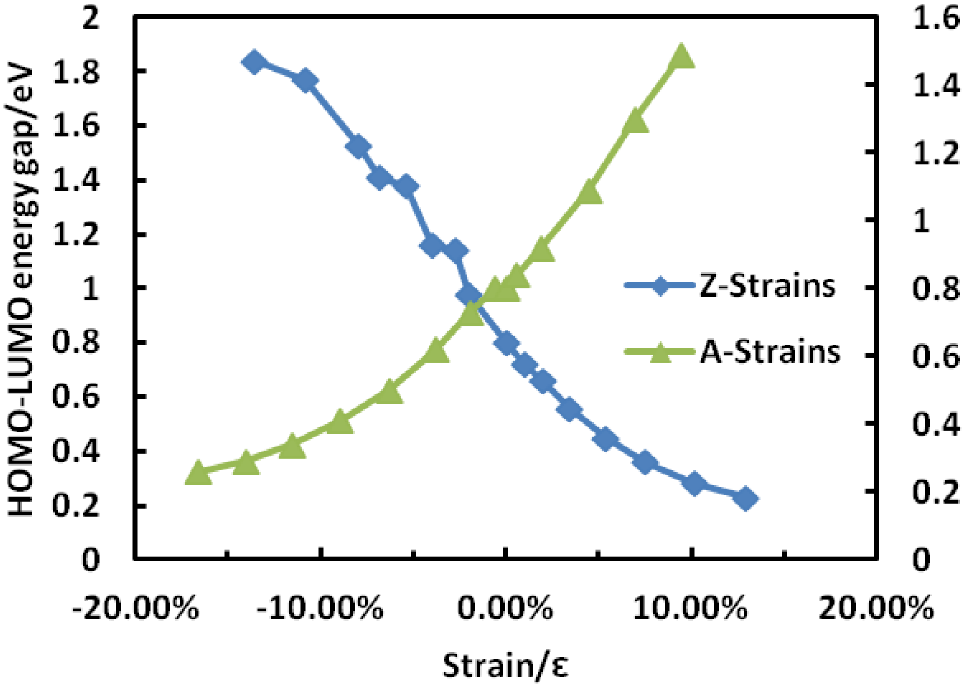

(a)

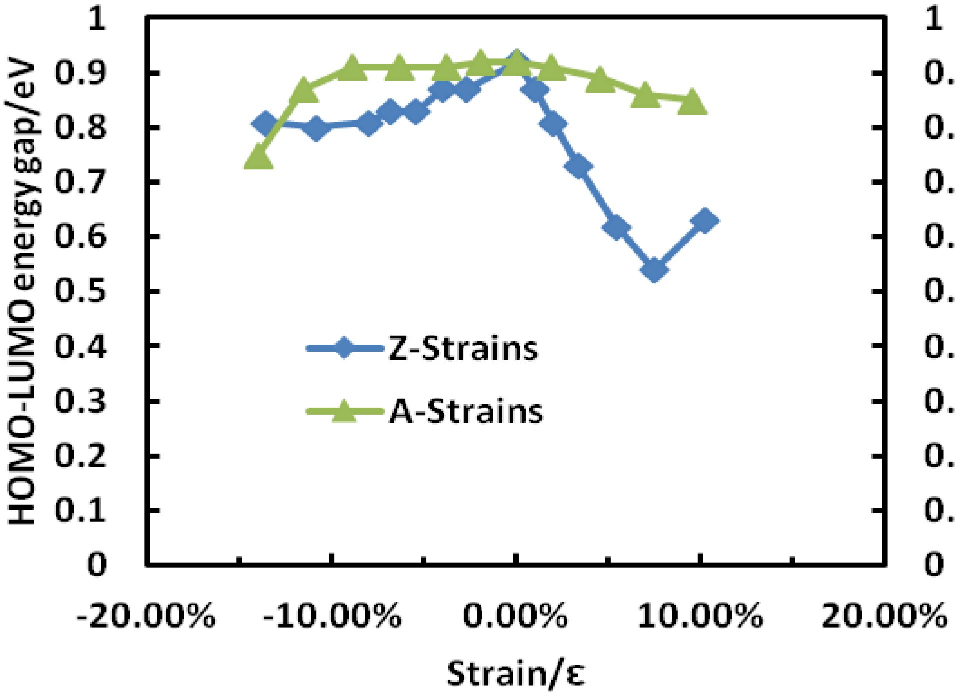

HOMO-LUMO energy gap/eV
1
0.9
0.8
0.7
0.6
0.5
0.4
0.3
0.2
0.1
0
-20.00%
-10.00%
0.00%
10.00%
20.00%
Strain/ε
Z-Strains
A-Strains

(b)

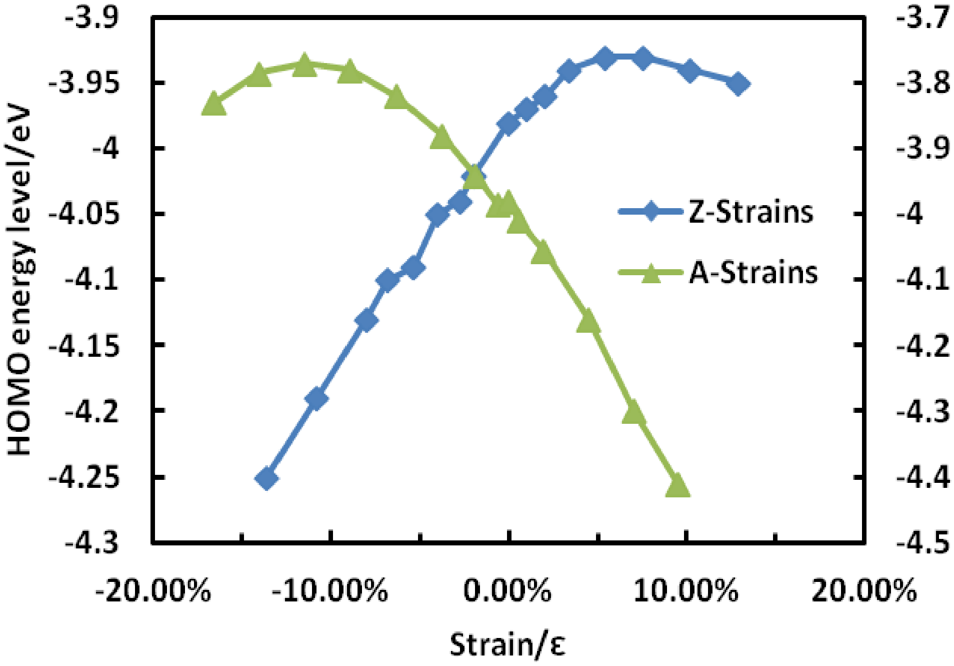

HOMO energy level/eV
-3.9
-3.95
-4
-4.05
-4.1
-4.15
-4.2
-4.25
-4.3
-3.7
-3.8
-3.9
-4
-4.1
-4.2
-4.3
-4.4
-4.5
-20.00%
-10.00%
0.00%
10.00%
20.00%
Strain/ε
Z-Strains
A-Strains

(c)

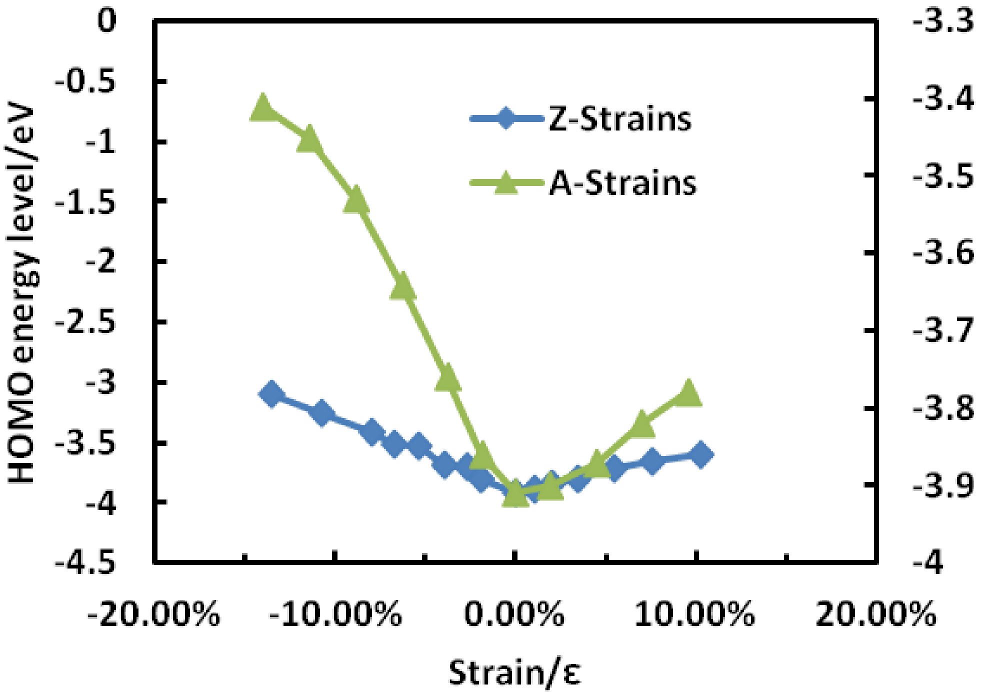

(d)

Figure 6-2 HOMO-LUMO energy gap correspond to strains along uniaxial zigzag and armchair direction on (a) $C_{100}H_{26}$, and (b) $C_{99}NH_{26}$; HOMO energy level versus strains along uniaxial zigzag and armchair directions on (c) $C_{100}H_{26}$, and (d) $C_{99}NH_{26}$.

6.3.2 Spin and Charge density

The ORR catalytic active sites on nitrogen doped graphene relate to the spin and charge density distributions on it. The active sites are these atoms possessing higher spin or charge density [239, 240]. Maximum values of spin and charge density, and percent of atoms with higher spin and charge density corresponding to strains on $C_{99}NH_{26}$ are explored, which are shown infigure 6-3. Figure 6-3 (a) shows the maximum value of charge density on nitrogen doped graphene $C_{99}NH_{26}$ versus strains. With increasing the tensile or compressive strain, the maximum value of charge density increases. Figure 6-3 (b) show the maximum value of spin density on $C_{99}NH_{26}$ versus strains. We can obtain that for the armchair direction strain, the small tensile or compress (~5.0% or ~ -10.0%) strain show slight effect of the maximum value of spin density, however the large strains make the maximum value of spin density decrease sharply. The maximum value of spin density almost keeps a constant with increasing of armchair direction strain from -10% to -5%, however when the strain lower than -10% or more than -5%, with increasing the strain, the maxium value of spin density decreas, which explains that the armchair direction strain is adverse to the atom possessing higer spin density. The maximum value of spin density increases linearly with the increasing of the zigzag direction strain, which confirmes that the tensile strain along zigzag direction is positive to the atom to obtaining higher spin density. Figure 6-3 (c) shows the percent of atoms with spin density more than 0.150 and 0.100 on $C_{99}NH_{26}$ corresponding to strains. It explains that the armchair direction strain shows light effect to the percent of atoms with high spin density. The effect of compress strain along zigzag direction is not obviously, however the tensile strain shows the strong effect to the percent of atoms possessing high spin density. With increasing the tensile strain along the zigzag direction, there are more carbon atoms obtaining higher spin density on the nitrogen doped graphene $C_{99}NH_{26}$. Therefore, we obtain that the TZ-strain is not only favorable to increasing the conductivity of nitrogen doped graphene, making it more reactive but also promoting it obtaining more catalytic active sites. It facilitates the catalytic activities of nitrogen doped graphene.

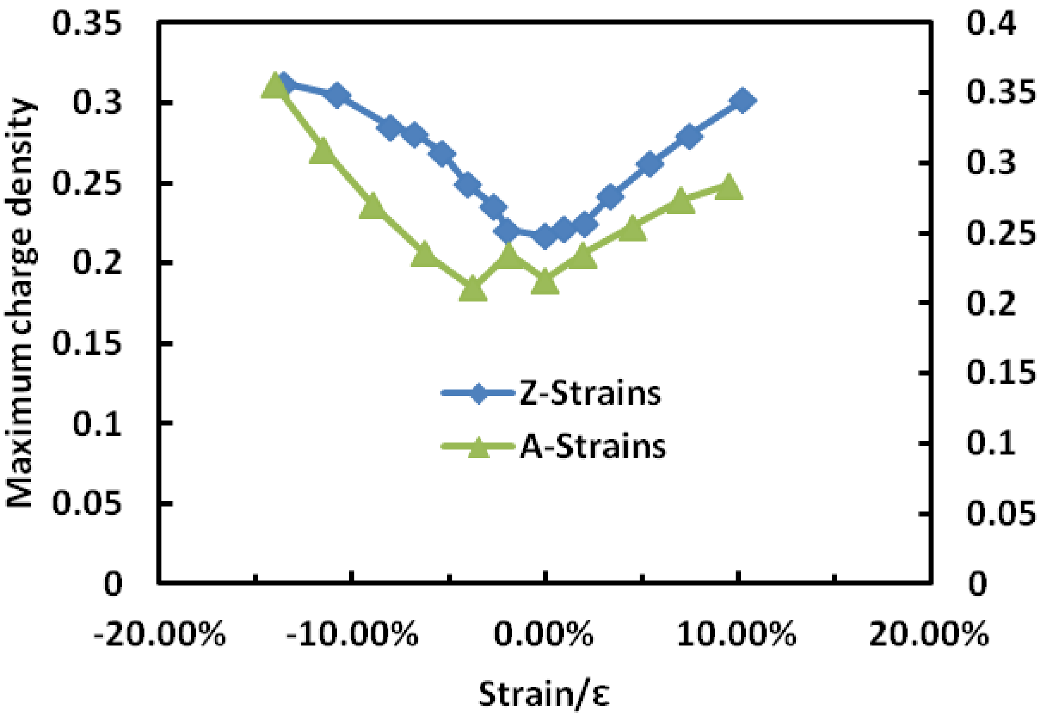
Maximum charge density
0.35
0.3
0.25
0.2
0.15
0.1
0.05
0
0.4
0.35
0.3
0.25
0.2
0.15
0.1
0.05
0
-20.00%
-10.00%
0.00%
10.00%
20.00%
Strain/ε
Z-Strains
A-Strains

(a)

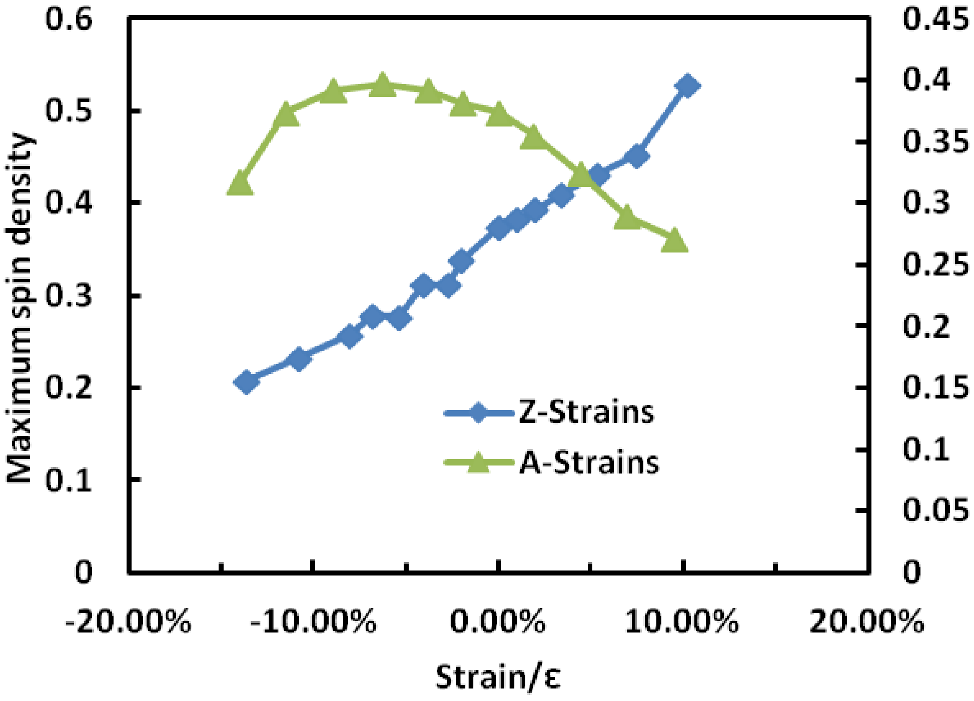
Maximum spin density
0.6
0.5
0.4
0.3
0.2
0.1
0
0.45
0.4
0.35
0.3
0.25
0.2
0.15
0.1
0.05
0
-20.00%
-10.00%
0.00%
10.00%
20.00%
Strain/ε
Z-Strains
A-Strains

(b)

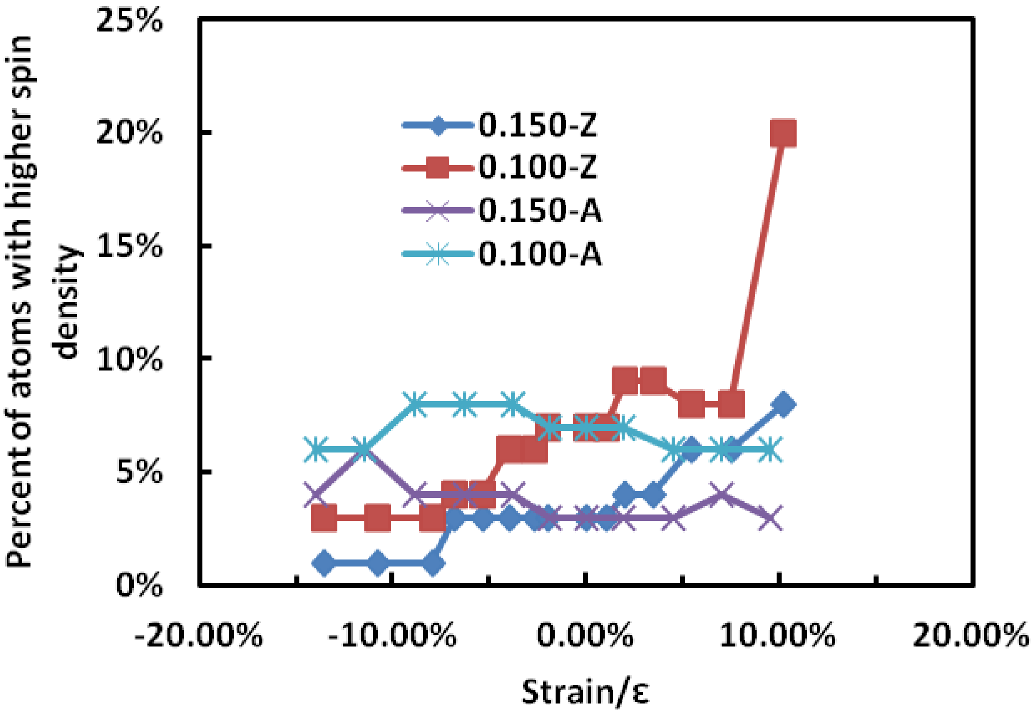

(c)

Figure 6-3 Maximum values of charge and spin densities on $C_{99}NH_{26}$ correspond to strains applied and the percent of atoms with higher charge or spin density; (a) maximum charge density on $C_{99}NH_{26}$ versus strains, (b) maximum spin density on $C_{99}NH_{26}$ versus strains, and (c) percent of atom with spin density more than 0.150 and 0.100 on $C_{99}NH_{26}$ correspond to strains.

6.4 Conclustions

It was confirmed that OOH or O_2 can not adsorb on perfect graphene in chapter IV and V. It cannot adsorb on perfect graphene applied strain either. Eventhough the zigzag tensile strain could be favorable to the catalytic properties of perfect graphene, it cannot make it show the catalytic activities to ORR. The more details of ORR on nitrogen doped graphene applied TZ-strain need to study further. This part of work we will carry on in future.

CHAPTER VII

CONLUSIONS AND FUTURE WORK

7.1 Conclusions

Using DFT method, the catalytic properties of nitrogen, sulfur doped graphene are studied. The effect of doping structure to the catalytic activities is explored. The role of other defects such as point and line defects, strain field on ORR catalytic properties on graphene is obtained.

7.1.1 ORR catalytic properties of doped graphene in fuel cells

Nitrogen, sulfur doped graphene were confirmed to show high catalytic activities for ORR in fuel cells. Generally, the atom which possesses highest spin density is the electrocatalytic active sites. If the negative value of spin density is small (less than -0.05), the atom with highest positive charge density (>0.35) may act as the active sites. In addition to the high efficient four- electron transfer reactions, there are also two-electrons transfer reactions occurred on these active sites with lower spin density or charge density.

With increasing the number of nitrogen dopants from one to four in cluster on the nitrogen doped graphene, the number of active sites per doping atom reaches to maximum at N=2 and then reduces, indicating that catalytic ability of nitrogen in larger cluster is weaker than that of single nitrogen or small cluster in terms of the number of catalytic sites available. The Stone-Wales defects enhance the catalytic capability of the nitrogen doped graphene by changing the HOMO-LUMO energy gap and reaction pathways. For four-electron transfer, the predicted effective reversible potential for N-doped graphene is in the range of 1.04~1.15 V/SHE with an average value of 1.10V/SHE, which is consistent with the experimental results. Engineering materials structures can promote catalytic capability of graphene by introducing small N cluster in combination with materials defects.

Four types structure of sulfur doped graphene were built, which are surface S-adsorbed, edge S-substituted, edge SO_2-substitued and sulfur-ring clustered graphene. Among these doping structures, surface sulfur adsorbed is more stable in terms of energy formation. The catalytic active sites on these S-doped graphene are those carbon atoms located at the zigzag edges or close to SO_2 doping structure. Two-electron transfer pathways proceed on the sulfur atom being the catalytic active sites while four-electron transfer reaction takes place on the carbon atoms. The Stone-Wales defects facilitate the formation of surface S-adsorption on graphene as well as the catalytic activities of sulfur-doped graphene, especially for those with sulfur adsorbing on the surface. Sulfur adsorbing/substituting and clustering make the graphene more locally polarized in HOMO and LUMO distribution at the zigzag edges and near the SO_2 doping sites of the graphene, which leads to enhanced catalytic activities at the edges.

7.1.2 Role of point and line defects on graphene for ORR catalytic properties in fuel cells

The point defects including Stone-Wales defects, single vacancy, double vacancies, and one substituting pentagon ring locating at zigzag edge, only pentagon ring induces high spin density and has catalytic capability for ORR. The one dimentional line defects such as pentagon-heptagon chain (GLD-57) and pentagon-pentagon-octagon chain (GLD-558), the structure containing odd number of heptagon or octagon carbon ring generates spin density and can catalyze ORR. For these graphenes showing catalytic activity for ORR, the catalytic active sites usually locate at zigzag edge or at end of the pentagon-pentagon-octagon chain. HOMO and LUMO distributions are strongly polarized on these active sites. The four-electron and two- electron ORR can occur on these defective graphenes simultaneously, and the sub-reaction is energetically favorable since the reaction free energies of them are negative.

7.1.3 Role of strains applied on graphene in ORR catalytic properties in fuel cells

Tensile and compressive strains along zigzag and armchair direction were applied on perfect and nitrogen doped graphene. TZ-strain and CA-strain could enhance the reactivity of the graphene but ORR catalytic activities cannot occur even the graphene is apllied with strain raniging from -16.6% to12.9%.

The tensile strain applied on nitrogen doped graphene along zigzag direction may potentially enhance its ORR catalytic activities. In result of increasing the strain, the HOMO-LUMO energy gap decreases, and the maximum value of spin density and the content of atoms possessing high spin density increase. These factors are favorable to the ORR catalytic properties of doped graphene.

7.2 Recommended future works

Future work includes:

1) Study the ORR catalytic properties of different hetero-atom doped graphene, such as nitrogen, boron, sulfur, chlorine doped graphene. Optimize the doping structures to obtain the higher catalytic activities materials.

2) Explore the effect of shape and the effective range of defects to the catalytic properties of graphene, the defects include hetero doped atom, point defects, line defects.

3) Investigate the axial strain effect on ORR catalytic activities of the graphene with different defects and the role of strains applying in different directions on the graphene.

4) Proble the more details of ORR on defective graphene, such as searching for the transition state structures of sub-reation, calculation the reaction path following, describing the reaction barrier of sub-reaction, and determing its reaction rate.

REFERENCES

[1] Gong, K. P.; Du, F.; Xia, Z. H.; Durstock, M.; Dai, L. M. *Science* **2009**, *323*, 760-764.

[2] Qu, L. T.; Liu, Y.; Baek, J. B.; Dai, L. M. *ACS Nano* **2010**, *4*, 1321–1326

[3] Mark K. Debe *Nature* **2012**, 486, 43-51

[4] Markovic, N. M. & Ross, P. N. *Surf. Sci. Rep.* **2002**, 45, 117–229

[5] A.K. Geim, K.S. Novoselov, *Nat. Meter.* **2007**, 6, 183

[6] C. Lee, X. D. Wei, J.W. Kysar, J. Hone, *Science* **2008**, 321, 385.

[7] K. S. Novoselov, A. K. Geim, S. V. Morozov, D. Jiang, M. I. Katsnelson, I. V. Grigorieva, S. V. Dubonos, A. A. Firsov, *Nature* **2005**, 438, 197.

[8] Y. Zhang, J. W. Tan, H. L. Stormer, P. Kim, *Nature* **2005**, 438, 201.

[9] K. S. Novoselov, Z. Jiang, Y. Zhang, S. V. Morozov, H. L. Stormer, U. Zeitler, J. C. Maan, G. S. Boebinger, P. Kim, A. K. Geim, *Science* **2007**, 315, 1379.

[10] M. Y. Han, B. Oezyilmaz, Y. Zhang, P. Kim, *Phys. Rev. Lett.* **2007**, 98, 206805.

[11] I. Meric, M. Y. Han, A. F. Young, B. Ozyilmaz, P. Kim, K. L. Shepard, *Nat. Nanotechnol.* **2008**, 3, 654.

[12] A. A. Balandin, S. Ghosh, W. Z. Bao, I. Calizo, D. Teweldebrhan, F. Miao, C. N. Lau, *Nano Lett.* **2008**, 8, 902.

[13] R. Ruoff, *Nat. Nanotechnol*. **2008**, 3, 10.

[14] K. P. Loh, Q. L. Bao, P. K. Ang, J. X. Yang, *J. Mater. Chem.* **2010**, 20, 2277.

[15] A. K. Geim, *Science* **2009**, 324, 1530.

[16] T. Enoki , K. Takai , V. Osipov , M. Baidakova , A. Vul , *Chem. Asian J.* **2009** , *4* , 796 .

[17] J. Liang , Y. Xu , Y. Huang , L. Zhang , Y. Wang , Y. Ma , F. Li , T. Guo , Y. Chen , *J. Phys. Chem. C* **2009**, *113*, 9921.

[18] X. Wang , L. Zhi , K. Mullen , *Nano Lett.* **2008** , *8* , 323 .

[19] E. J. Yoo , J. Kim , E. Hosono , H. Zhou , T. Kudo , I. Honma , *Nano Lett.* **2008** , *8* , 2277 .

[20] S. R. C. Vivekchand , C. S. Rout , K. S. Subrahmanyam , A. Ovindaraj , C. N. R. Rao , *J. Chem. Sci.* **2008** , *120*, 9.

[21] X. Wang , L. Zhi , N. Tsao , Tomovi , J. Li , K. Mullen , *Angew. Chem. Int. Ed.* **2008** , *47* , 2990 .

[22] G. Eda , G. Fanchini , M. Chhowalla , *Nat. Nanotechnol.* **2008** , *3* , 270 .

[23] W. Yang , K. R. Ratinac , S. P. Ringer , P. Thordarson , J. J. Gooding , F. Brat , *Angew. Chem. Int. Ed.* **2010** , *49* , 2114 .

[24] S. Stankovich, D. A. Dikin, G. H. B. Dommett, K. M. Kohlhaas, E. J. Zimney, E. A. Stach, R. D. Piner, S. T. Nguyen, R. S. Ruoff, *Nature* **2006**, 442, 282.

[25] L. Gong, I. A. Kinloch, R. J. Young, I. Riaz, R. Jalil, K. S. Novoselov, *Adv. Mater.* **2010**, 22, 2694.

[26] K. S. Novoselov, A. K. Geim, S. V. Morozov, D. Jiang, Y. Zhang, S. V. Dubonos, I. V. Grigorieva, A. A. Firsov, *Science*, **2004**, 306, 666.

[27] K. S. Novoselov, D. Jiang, F. Schedin, T. J. Booth, V. V. Khotkevich, S. V. Morozov, A. K. Geim, Proc. *Natl. Acad. Sci.* USA **2005**, 102, 10451.

[28] S. Park, R. S. Ruoff, *Nat. Nanotechnol.* **2009**, 4, 217.

[29] P. Sutter , *Nat.Mater.* **2009**, *8*, 171.

[30] L. W. C. Ren , L. B. Gao , L. P. Ma , H. M. Cheng , *New Carbon Mater.***2011** , *26* , 71.

[31] I. Pl ko , M. K lj , P. P v , R. B ko , J. Co ux , A. N'D y , C. Bu , T. Michely , *Phys. Rev. Lett.* **2009** , *102* , 056808 .

[32] K. S. Kim , Y. Zhao , H. Jang , S. Y. Lee , J. M. Kim , J. H. Ahn , P. Kim , J. Y. Choi , B. H. Hong , *Nature* **2009** , *457* , 706.

[33] S. Bae , H. Kim , Y. Lee , X. Xu , J. S. Park , Y. Zheng , J. Balakrishnan , T. Lei , H. R. Kim , Y. I. Song , *Nat. Nanotechnol.* **2010**, *5* ,574.

[34] X. Li , W. Cai , J. An , S. Kim , J. Nah , D. Yang , R. Piner , A. Velamakanni , I. Jung , E. Tutuc , *Science* **2009** , *324* , 1312 .

[35] D. R. Lenski , M. S. Fuhrer , *J. Appl. Phys.* **2010**, *110*, 013720 .

[36] Z. Sun , Z. Yan , J. Yao , E. Beitler , Y. Zhu , J. M. Tour , *Nature* **2011**, *471*, 124.

[37] W. S. Hummers , R. E. Offeman , *J. Am. Chem. Soc.* **1958**, *80*, 1339 .

[38] J. Shen , Y. Hu , M. Shi , X. Lu , C. Qin , C. Li , M. Ye , *Chem. Mater.* **2009**, *21*, 3514.

[39] S. Muller, K. M_llen, *Philos. Trans. R. Soc. London Ser. A* **2007**, 365, 1453.

[40] J. Wu, W. Pisula, K. M_llen *Chem. Rev.* **2007**, 107, 718.

[41] L. J. Zhi, K. M_llen, *J. Mater. Chem.* **2008**, 18, 1472.

[42] C.N.R Rao, A.K. Sood, K.S. Subrahmanyam, and A. Govindaraj; *Angew. Chem. Int. Ed.* **2009**, 48, 7752-7777.

[43] P. R. Wallace, *Phys. Rev.* **1947**, 71, 622.

[44] J. W. McClure, *Phys. Rev.* **1957**, 108, 612.

[45] J. C. Slonczewski, P. R. Weiss, *Phys. Rev.* **1958**, 109, 272.

[46] K. Novoselov, *Nat. Mater.* **2007**, 6, 720.

[47] A. C. Neto, F. Guinea, N. M. R. Peres, *Phys.World* **2006**, 19, 33.

[48] Hashimoto, A.; Suenaga, K.; Gloter, A.; Urita, K.; Iijima, S. *Nature* **2004**, *430*, 870–873.

[49] Gass, M. H.; Bangert, U.; Bleloch, A. L.; Wang, P.; Nair, R. R.; Geim, A. K. *Nat. Nanotechnol.* **2008**, *3*, 676–681.

[50] Meyer, J. C.; Kisielowski, C.; Erni, R.; Rossell, M. D.; Crommie, M. F.; Zettl, A. *Nano Lett.* **2008**, *8*, 3582–3586.

[51] Warner, J. H.; Ru¨ mmeli, M. H.; Ge, L.; Gemming, T.; Montanari, B.; Harrison, N. M.; Bu¨ chner, B.; Briggs, G. A. D. *Nat. Nanotechnol.* **2009**, *4*, 500–504.

[52] Girit, C. O.; Meyer, J. C.; Erni, R.; Rossell, M. D.; Kisielowski, C.; Yang, L.; Park, C.-H.; Crommie, M. F.; Cohen, M. L.; Louie, S. G.; *et al. Science* **2009**, *323*, 1705–1708.

[53] Ugeda, M. M.; Brihuega, I.; Guinea, F.; Go´ mez-Rod ı´gu z, J. M. *Phys. Rev. Lett.* **2010**, *104*, 096804.

[54] Tapaszto´ , L.; Dobrik, G.; Nemes-Incze, P.; Vertesy, G.; Lambin, P.; Biro´ , L. P. *Phys. Rev. B* **2008**, *78*, 233407.

[55] Lu, A. J.; Pan, B. C. *Phys. Rev. Lett.* **2004**, *92*, 105504.

[56] Kotakoski, J.; Krasheninnikov, A. V.; Nordlund, K. *Phys. Rev. B* **2006**, *74*, 245420.

[57] Miyamoto, Y.; Berber, S.; Yoon, M.; Rubio, A.; Toma´nek, D. *Chem. Phys. Lett.* **2004**, *392*, 209–213.

[58] Krasheninnikov, A. V.; Lehtinen, P. O.; Foster, A. S.; Nieminen, R. M. *Chem. Phys. Lett.* **2006**, *418*, 132–136.

[59] Rossato, J.; Baierle, R. J.; Fazzio, A.; Mota, R. *Nano Lett.* **2005**, *5*, 197–200.

[60] El-Barbary, A. A.; Telling, R. H.; Ewels, C. P.; Heggie, M. I.; Briddon, P. R. *Phys. Rev. B* **2003**, *68*, 144107.

[61] Ewels, C. P.; Telling, R. H.; El-Barbary, A. A.; Heggie, M. I.; Briddon, P. R. *Phys. Rev. Lett.* **2003**, *91*, 025505.

[62] Krasheninnikov, A. V.; Elesin, V. F. *Surf. Sci.* **2000**, *519*, 454–456.

[63] Stone, A. J.; Wales, D. J. *Chem. Phys. Lett.* **1986**, *128*, 501–503.

[64] Florian Banhart, Jani Kotakoski, and Arkady V. Krasheninnikov *ACS Nano* **2011**, 5, 26-41.

[65] Li, L.; Reich, S.; Robertson, J. *Phys. Rev. B* **2005**, *72*, 184109.

[66] Ma, J.; Alfe´ , D.; Michaelides, A.; Wang, E. *Phys. Rev. B* **2009**, *80*, 033407.

[67] Tsetseris, L.; Pantelides, S. T. *Carbon* **2009**, *47*, 901–908.

[68] Lusk, M. T.; Car, L. D. *Phys. Rev. Lett.* **2008**, *100*, 175503

[69] Banhart, F. *Nanoscale* **2009**, *1*, 201–213.

[70] Nemec, N.; Toma´nek, D.; Cuniberti, G. *Phys. Rev. Lett.* **2006**, *96*, 076802.

[71] Ci, L.; Song, L.; Jin, C.; Jariwala, D.; Wu, D.; Li, Y.; Srivastava, A.; Wang, Z. F.; Storr, K.; Balicas, L. *Nat. Mater.* **2010**, *9*, 430–435.

[72] Boukhvalov, D. W.; Katsnelson, M. I. *Nano Lett.* **2008**, *8*, 4373–4379.

[73] Nevidomskyy, A. H.; Csa´nyi, G.; Payne, M. C. *Phys. Rev. Lett.* **2003**, *91*, 105502.

[74] Co ux, J. N’D y , A. T. Bu , C. *Nano Lett.* **2008**, *8*, 565–570.

[75] Cˇ v k , J. K l o , M. I. Fl p , C. F . J. *Nat. Phys.* **2009**, *5*, 840–844.

[76] Lahiri, J.; Lin, Y.; Bozkurt, P.; Oleynik, I. I.; Batzill, M. *Nat. Nanotechnol.* **2010**, *5*, 326–329.

[77] Jeong, B. W.; Ihm, J.; Lee, G.-D. *Phys. Rev. B* **2008**, *78*, 165403.

[78] Yazyev, O. V.; Louie, S. G. *Phys. Rev. B* **2010**, *81*, 195420.

[79] Malola, S.; Ha¨kkinen, H.; Koskinen, P. *Phys. Rev. B* **2010**, *81*, 165447.

[80] D. Gunlycke and C. T. White *PRL* **2011**, 106, 136806

[81] Pinshane Y. Huang, Carlos S. Ruiz-Vargas, Arend M. van der Zande, William S. Whitney, Mark P. Levendorf, Joshua W. Kevek, Shivank Garg, Jonathan S. Alden, Caleb J. Hustedt, Ye Zhu, Jiwoong Park, Paul L. McEuen, David A. Muller; *Nature* **2011**, 469, 389-392

[82] Das A, Pisana S, Chakraborty B, Piscanec S, Saha SK, Waghmare UV, et al. *Nat Nanotechnol* **2008**, 3, 210–5.

[83] Zhang YB, Tang TT, Girit C, Hao Z, Martin MC, Zettl A, et al. *Nature* **2009**, 459, 820–3.

[84] Santos JE, Peres NMR, dos Santos J, Neto AHC. *Phys Rev B* **2011**, 84, 085430.

[85] Miwa RH, Schmidt TM, Scopel WL, Fazzio A. *Appl. Phys. Lett.* **2011**, 99, 163108.

[86] Zhao L.Y., He R, Rim KT, Schiros T, Kim KS, Zhou H, et al. *Science* **2011**. 333, 999–1003.

[87] Yu WJ, Liao L, Chae SH, Lee YH, Duan XF. *Nano Lett* **2011**, 11, 4759–63.

[88] Panchokarla LS, Subrahmanyam KS, Saha SK, Govindaraj A, Krishnamurthy HR, Waghmare UV, et al. *Adv Mater* **2009**, 21, 4726–30.

[89] Dai JY, Yuan JM, Giannozzi P. *Appl Phys Lett* **2009**, 95, 232105.

[90] I. Jeon, H. Choi, M. Choi, J. Seo, S. Jung, M. Kim, S, Zhang, L. Zhang, Zhenhia Xia, L. Dai, N. Park. J. Baek; Facile, Scalable Synthesis of Edge-halogenated Graphene Nanoplatelets as Efficient Metal-free Electrocatalysts for Oxgen Reduction Reaction; *Sci. Rep.* **2013** Doi:10.1038.

[91] Qu Liangti, LiuYong, Baek Jong-Beom, and Dai Liming *ACS NANO*, **2010**, 4, 1321-1326.

[92] Feng Leiyu, Chen Yingguang, Chen Lang *ACS NANO*, **2011**, 5, 9611-9618

[93] Luo Zhiqiang, Lim Sanhua, Tian, Zhiqun, Shang Jingzhi, Lai Linfei, MacDonald Brian, Fu Chao, Shen Zexiang, Yu Ting and Lin Jianyi *J. Mater. Chem.* **2011**, 21, 8038

[94] Deng Dehui, Pan Xiulian, Yu Liang, Gui Yi, Jiang Yeping, Qi Jing, Li WeiXue, Fu Qiang, Ma Xucun, Xue Qikun, Sun Gongquan, and Bao Xinhe *Chem. Mater.* **2011**, 23, 1188-1193.

[95] Shao Yuyan, Zhang Sheng, Engelhard Mark H. Li Guosheng, Shao Guocheng, Wang Yong, Liu Jun, Aksay Ilhan A.; and Lin Yuehe *J. Mater. Chem.* **2010**, 20, 7481-7496

[96] Geng Dongsheng, Chen Ying, Chen Yougui, Li Yongliang, Li Ruying, Sun Xueliang, Ye Siyu, and Shanna Knights *Energy Environ. Sci.* **2011**, 4, 760-764

[97] Ming-Yu Yen, Chien-Luo Hsieh, Chih-Chun Teng, Min-Chien Hsiao, Po-I Liu, Chen-Chi M. Ma, Ming-Chi Tsai, Chuen-Horng Tsai, Yan-Ru Lin and Tsung-Yu Chou; *RSC Advances*, **2012**, 2, 2725-2728

[98] Guiqiang Wang, Yanyan Fang, Yuan Lin, Wei Xing, Shuping Zhuo *Materials Research Bulletin*, **2012**, 47, 4252-4256.

[99] Yongliang Li, Jiajun Wang, Xifei Li, Dongsheng Geng, Mohammad N. Banis, Ruying Li, Xueliang Sun *Electrochemistry Communications*, **2012**, 18, 12-15

[100] Xifei Li, Dongsheng Geng, Yong Zhang, Xiangbo Meng, Ruying Li, Xueliang Sun *Electrochemistry Communications*, **2011**, 13, 822-825

[101] Reddy Arava Leela Mohana, Srivastava Anchal, Gowda Sanketh R., Gullapalli Hemtej, Dubey Madan and Ajayan Pulickel M. *ACS NANO*, **2010**, 4, 6337-6342.

[102] Haibo Wang, Chuanjian Zhang, Zhihong Liu, Li Wang, Pengxian Han, Hongxi Xu, Kejun Zhang, Shanmu Dong, Jianhua Yao and Guanglei Cui *J. Mater. Chem.* **2011**, 21, 5430

[103] Wei Dacheng, Liu Yunqi, Wang Yu, Zhang Hongliang, Huang Liping, Yu Gui *Nano Letters* **2009**, 9, 1752-1758.

[104] (a) Keskar, G.; Rao, R.; Luo, J.; Hudson, J.; Chen, J.; Rao, A. M. *Chem. Phys. Lett.* **2005**, *412*, 269–273. (b) Yang, Q. H.; Hou, P. X.; Unno, M.; Yamauchi, S.; Saito, R.; Kyotani, T. *Nano Lett.* **2005**, *5*, 2365–2469.

[105] Thomsen, C.; Reich, S. *Phys. Re*V. *Lett.* **2000**, *85*, 5214–5217.

[106] (a) Suenaga, K.; Yudasaka, M.; Colliex, C.; Iijima, S. *Chem. Phys. Lett.* **2000**, *316*, 365–372. (b) Lee, Y. T.; Kim, N. S.; Bae, S. Y.; Park, J.; Yu, S. C.; Ryu, H.; Lee, H. J. *J. Phys. Chem. B* **2003**, *107*, 12958–12963. (c) Wei, D. C.; Liu, Y. Q.; Cao, L. C.; Fu, L.; Li, X. L.; Wang, Y.; Yu, G.; Zhu, D. B. *Nano Lett.* **2006**, *6*, 186–192.

[107] (a) Das, A.; et al. *Nat. Nanotechnol.* **2008**, *3*, 210–215. (b) Pisana, S; Lazzeri, M.; Casiraghi, C.; Novoselov, K. S.; Geim, A. K.; Ferrari, A. C.; Mauri, F. *Nat. Mater.* **2007**, *6*, 198–201. (c) Das, B.; Voggu, R.; Rout, C. S.; Rao, C. N. R. *Chem. Commun.* **2008**, 5155–5157.

[108] Graf, D.; Molitor, F.; Ensslin, K.; Stampfer, C.; Jungen, A.; Hierold, C.; Wirtz, L. *Nano Lett.* **2007**, *7*, 238–242.

[109] Yan, J.; Henriksen, E. A.; Kim, P.; Pinczuk, A. *Phys. ReV. Lett.* **2008**, *101*, 136804.

[110] Das, A.; Chakraborty, B.; Sood, A. K. *Bull. Mater. Sci.* **2008**, *31*, 579–584.

[111] Duan, X. J.; Son, H.; Gao, B.; Zhang, J.; Wu, T. J.; Samsonidze, G. G.; Dresselhaus, M. S.; Liu, Z. F.; Kong, J. *Nano Lett.* **2007**, *7*, 2116–2121.

[112] Zhang, Y. Y.; Zhang, J.; Son, H.; Kong, J.; Liu, Z. F. *J. Am. Chem. Soc.* **2005**, *127*, 17156–17157.

[113] Ferrari, A. C.; et al. *Phys. Rev. Lett.* **2006**, *97*, 187401.

[114] Gupta, A.; Chen, G.; Joshi, P.; Tadigadapa, S.; Eklund, P. C. *Nano Lett.* **2006**, *6*, 2667–2673.

[115] Ni, Z. H.; Wang, H. M.; Kasim, J.; Fan, H. M.; Yu, T.; Wu, Y. H.; Feng, Y. P.; Shen, Z. X. *Nano Lett.* **2007**, *7*, 2758–27

[116] (a) Jang, J. W.; Lee, C. E.; Lyu, S. C.; Lee, T. J.; Lee, C. J. *Appl. Phys. Lett.* **2004**, *84*, 2877–2879. (b) Ronning, C.; Feldermann, H.; Merk, R.; Hofsass, H.; Reinke, P.; Thiele, J. U. *Phys. ReV. B* **1998**, *58*, 2207–2215. (c) Marton, D.; Boyd, K. J.; Al-Bayati, A. H.; Todorov, S. S.; Rabalais, J. W. *Phys. ReV. Lett.* **1994**, *73*, 118–121.

[117] Wang, X. B.; Liu, Y. Q.; Zhu, D. B.; Zhang, L.; Ma, H. Z.; Yao, N.; Zhang, B. L. *J. Phys. Chem. B* **2002**, *106*, 2186–2190.

[118] Casanovas, J.; Ricart, J. M.; Rubio, J.; Illas, F.; Jimenez-Mateos, J. M. *J. Am. Chem. Soc.* **1996**, *118*, 8071–8976.

[119] Novoselov, K. S.; Geim, A. K.; Morozov, S. V.; Jiang, D.; Zhang, Y.; Dubonos, S. V.; Grigorieva, I. V.; Firsov, A. A. *Science* **2004**, *306*, 666–669.

[120] Fu, L.; Liu, Z. M.; Liu, Y. Q.; Han, B. X.; Hu, P. A.; Cao, L. C.; Zhu, D. B. *Adv. Mater.* **2005**, *17*, 217–221.

[121] Dongsheng Geng, Ying Chen, Yougui Chen, Yongliang Li, Ruying Li, Xueliang Sun, Siyu Ye and Shanna Knights *Energy Environ. Sci.* **2011**, 4, 760

[122] Dehui Deng, Xiulian Pan, Liang Yu, Yi Cui, Yeping Jiang, Jing Qi, Weixue Li, Qiang Fu, Xucun Ma, Qikun Xue, Gongquan Sun, and Xinhe *Bao Chem. Mater.* **2011**, 23, 1188-1193.

[123] D. Usachov, O. Vilkov, A. Grüneis, D. Haberer, A. Fedorov, V. K. Adamchuk, A. B. Preobrajenski, P. Dudin, A. Barinov, M. Oehzelt, C. Laubschat, and D. V. Vyalikh *Nano Lett.* **2011**, 11, 5401-5407.

[124] Steele B. C. H., Heinzel A. *Nature* **2001**, 414, 345-352

[125] E. B. Yeager; *Electrochim. Acta* **1984** 29, 1527

[126] Tianhou Zhang, Alfred B. Anderson *Electrochimica Acta* **2007**, 53, 982-989

[127] A. B. Anderson, Y. Cai, R. A. Sidik, D. B. Kang, *J. Electroanal. Chem.* **2005**, 580, 17

[128] J. Roques, A. B. Anderson, *J. Fuel Cell Sci. Technol*. **2005**, 2, 86

[129] Reyimjan, A. Sidik, A. B. Anderson; *J. Phys. Chem. B.* **2006**, 110, 1787-1793

[130] Reyimjan, A. Sidik; Alfred B. Anderson *J. Phys. Chem. B* **2006**, 110, 1787-1793.

[131] Ellen Vayner and Alfred B. Anderson *J. Phys. Chem. C* **2007** 111, 9330-9336.

[132] Liang Yu, Xiulian Pan, Xiaoming Gao, P. Hu, Xinhe Bao *Journal of Catalysis* 2011, 282, 183-190

[133] Lherbier, A.; Blase, X.; Niquet, Y.-M.; Triozon, F.; Roche, S. *Phys. Rev. Lett.* **2008**, 101, 036808.

[134] Martins, T. B.; Miwa, R. H.; da Silva, A. J. R.; Fazzio, A. *Phys. Rev. Lett.* **2007**, 98, 196803.

[135] Marconcini P., Cresto A., Triozon F., Fiori G., Biel B., Niquet YM., Macucci M., Roche S. *ACS Nano* **2012**, 6, 7942-7

[136] Zhen Huan Sheng, Hongli Gao, Wenjing Bao, Fengbin Wang, Xinghua Xia *J. Mater. Chem.* **2012**, 22, 390;

[137] Yoong Ahm Kim, Kazunori Fujisawa, Hiroyuki Muramatsu, Takuya Hayashi, Morinobu Endo, Toshihikio Fujimori, Katsumi Kaneko, Mauricio Terrones, Jan Behrends, Axel Eckmann, Cizia Casiraghi, Kostya S. Novoselov, Riichiro Saito, and Mildred S. Dresselhaus *ACS NANO*, **2012**, 6, 6293-6300

[138] Chang Hyuck Chsi, Sung Hyeon Park, and Seong Ihl Woo; *ACS NANO*, **2012**, 6, 7084-7091.

[139] Xiao Li, Lili Fan, Zhen Li, Kunlin Wang, Minlin Zhong, Jinquan Wei, Dehai Wu, and Hongwei Zhu *Adv. Energy Mater.* **2012**, 2, 425-429.

[140] T. Lin , F. Huang , J. Liang , Y. Wang , *Energy Enviorn. Sci.* **2011**, *4*, 862.

[141] Zhongshuai Wu, Wencai Ren, Li Xu, Feng Li, and Huiming Cheng *ACS NANO*, **2011**,5, 5463-5471

[142] Xianlong Wang, Zhi Zeng, Hyojun Ahn, and Guoxiu Wang *Applied Physics Letters* **2009**, 95, 183103

[143] Shuangyin Wang, Lipeng Zhang, Zhenhai Xia, Ajit Roy, Dong Wook Chang, Jong-Beom Baek and Liming Dai *Angew. Chem. Int. Ed.* **2012**, 51, 1-5.

[144] Chang Hyuck Choi, Sung Hyeon Park, and Seong Ihi Woo *ACS NANO*, **2012**, 6, 7084-7091.

[145] Zhong-shuai Wu, Andreas Winter, Long Chen, Yi Sun, Andrey Turchanin, Xinliang Feng, and Klaus Müllen *Adv. Mater.* **2012**, 24, 5130-5135.

[146] Andrey Lyalin, Akrira nakayama, Kohei Uosaki and Tetsuya Taketrugu. *Phys. Chem. Chem. Phys.*, **2013**, 15, 2809-2820.

[147] Yang, Z.; Yao, Z.; Li, G.; Fang, G.; Nie, H.; Liu, Z.; Zhou, X.; Chen, X. a.; Huang, S. *ACS Nano* **2012**, 6, 205-211.

[148] Yang, S.; Zhi, L.; Tang, K.; Feng, X.; Maier, J.; Müllen, K. *Adv. Funct. Mater.* **2012**, 22, 3634-3640.

[149] Gao, H.; Liu, Z.; Song, L.; Guo, W.; Gao, W.; Ci, L.; Rao, A.; Quan, W.; Vajtai, R.; Ajayan, P. M. *Nanotechnology* **2012**, 23, 275605.

[150] Li Youngliang, Wang Jiajun, Li Xifei, Geng Dongsheng, Banis Mohammad N., Tang Yongji, Wang Dongniu, Li Ruying, Sham Tsun-Kong and Sun Xueliang *J. Mater. Chem.*, **2012**, 22, 20170-20174

[151] S. B. Yang , X. L. Feng , L. J. Zhi , Q. A. Cao , J. Maier , K. Müllen *Adv. Mater.* **2010**, 22, 838.

[152] Bo Li, Lin Zhou, Di Wu, Hailin Peng, Kai Yan, Yu Zhou, and Zhongfan Liu *ACS NANO*, **2011**, 5, 5957-5961.

[153] Ferrari, A. C; Meyer, J. C; Scardaci, V.; Casiraghi, C.; Lazzeri, M.; Mauri, F.; Piscanec, S.; Jiang, D.; Novoselov, K. S.; Roth, S. *Phys. Rev. Lett.* **2006**, 97, 187401.

[154] Papirer, E.; Lacroix, R.; Donnet, J. B.; Nanse, G.; Fioux, P. *Carbon* **1995**, 33, 63-72

[155] Justin Wu, Liming Xie, Yanguang Li, Hailiang Wang, Yijian Ouyang, Jing Guo, and Hongjie Dai *J. Am. Chem. Soc.* **2011**, 133, 19668-19671.

[156] Mingmei Yang, Lin Zhou, Jinying Wang, Zhongfan Liu, and Zhirong Liu *J. Phys. Chem. C* **2012**, 116, 844-850

[157] Sheng Zhang, Lipeng Zhang, Jong-beom Baek, Zhenhai Xia, Liming Dai; Facile, Scalable synthesis of chlorine doped graphite as efficient metal-free oxygen reduction electrocatalyst **2103**

[158] Zhiping Jin, Huagui Nie, Zhi Yang, Jing Zhang, Zheng Liu, Xiangju Xu and Shaoming Huang *Nanoscale*, **2012**, 4, 6455-6460

[159] Hongmei Wang, Hongxia Wang, Ying Chen, Yuejie Liu, Jingxiang Zhao, Qinghai Cai, Xuanzhang Wang *Applied Surface Science* **2013**, 18 Feb. (online)

[160] Dingshan Yu, Yuhua Xue, and Liming Dai; *J. Phys. Chem. Lett.* **2012**, 3, 2863-2870

[161] Ji Liang, Yan Jiao, Mietek Jaroniec, and Shi Zhang Qiao *Angew. Chem. Int. Ed.* **2012**, 51, 1-6

[162] K. S. Novoselov, A. K. Geim, S. V. Morozov, D. Jiang, Y. Zhang, S. V. Dubonos, I. V. Grigorieva, and A. A. Firsov *Science*, 2004, 306, 666.

[163] James B. Foresman and Eleen Frisch Exploring Chemistry with Electronic Strcutre Method, 2nd EditionGaussian, Inc. Pittsburgh, PA

[164] Hinchliffe, Alan (2000).Modelling Molecular Structures (2nd ed.). Baffins Lane, Chichester, West Sussex PO19 1UD, England: John Wiley & Sons Ltd. p. 186. ISBN 0-471-48993-X.

[165] Szabo, A.; Ostlund, N. S. (1996). Modern Quantum Chemistry. Mineola, New York: Dover Publishing. ISBN 0-486-69186-1.

[166] D. A. Armstrong, D. Yu, and A. Rauk Can. J. Chem. 1996, 74 1192

[167] G. A. DiLabio, D. A. Pratt, A. D. Loraro, and J. S. Wright J. Phys. Chem. A 1999, 103, 1653-1661

[168] Reyimjan A. Sidik, Alfred B. A. J. Phys. Chem. B 2006, 110, 1787-1793

[169] Zheng, H. X.; Duley, W.; *Phys. Rev. B* **2008**, *78*, 155118.

[170] Qu, L.T.; Liu, Y.; Baek, J.B.; Dai, L.M.; *ACS Nano*, **2010,** *4*, 1321-1326.

[171] Aihara, J-I.; *J. Phys. Chem. A* **1999,** *103*, 7487-7495.

[172] Shemella, P.; Zhang, Y. M.; Mailman, M.; *Appl. Phys. Lett.* **2007**, *91*, 042101.

[173] Frisch, M. J.; Pople, J. A.; Binkley, J. S.; *J. Chem. Phys.* **1984**, *80* ,3265-3269.

[174] Wang, S. Y.; Yu, D. S.; Dai, *L. M.; J. Am. Chem. Soc.* **2011** (online)

[175] Qu, L.; Liu,Y.; Baek, J. B.; Dai, L.; *ACS Nano*, **2010**, *4*, 1321.

[176] Gong, K.; Du, F.; Xia, Z.; Dustock, M.; Dai, L.; *Science* **2009**, 323.

[177] Luo, Z.; Lim, S.; Tian, Z.; Shang, J.; Lai, L.; MacDonald, B.; *J. Mater. Chem.* **2011**, *21,* 8038.

[178] Shao, Y. ; Zhang, S.; Engelhard, M. H.; Li, G.; Shao, G.; Wang,Y.; *J. Mater. Chem*. **2010**, *20*, 7491.

[179] Lee, K.; Lee, J.; Ahn, B.; Woo, S.; *Electrochemistry Communications* **2010**, *12,* 1052.

[180] Wang, P.; Wang, Z.; Jia, L.; Xiao, Z., *Phys. Chem. Chem. Phys.* **2009**, *11*, 2730.

[181] Meyer, J. C.; Kisielowski, C.; Erni,R.; Rossell, M. D.; Crommie, M.F.; Zettl, A.; *Nano Letters* **2008**, 8, 3582.

[182] Boukhvalov, D.W.; Katsnelson, M.I.; *Nano Letters* **2008**, 8, 4373.

[183] Banhart, F.; Kotakoski, J.; Krasheninnikov, A. V.; *ACS Nano* **2011**, 5, 26.

[184] Zhang,L.; Xia, Z.; *J. Phys. Chem. C* **2011**, *115*, 11170.

[185] Kim, H.; Lee,K; Woo,S.I.; Jung, Y; *Phys. Chem. Chem. Phys.* **2011**, 13, 17505.

[186] Yu, L.; Pan, X.; Gao, X.; Hu, P.; Bao, X.; *Journal of Catalysis* **2011**, *282*, 183

[187] Roques, J.; Anderson, A. B.; *J. Fuel Cell Sci. Tech.* **2005**, *2*, 86.

[188] Kurak, K. A.; Anderson, A. B.; *J. Phys. Chem. C* **2009**, *113*, 6730.

[189] Roques, J.; Anderson, A. B.; *J. Electrochem. Soc.* **2004**, *151*, E340.

[190] Walch, S..; Dhanda, A..; Aryanpour, M.; Pitsch, H.; *J. Phys. Chem. C* **2008**, *112*, 8464.

[191] Chen, R. R.; Li, H. X.; Chu, D.; Wang, G. F.; *J. Phys. Chem.* C **2009**, *113*, 20689.

[192] Feng, T.; Anderson, A. B.; *J. Phys. Chem. C* **2011**, *115*, 4076.

[193] Ruvinskiy, P. S.; Bonnefont, A.; Pham-Huu, C.; Savinova, E. R.; *Langmuir* **2001**, *27*, 9018.

[194] Webster, S.; Maultzsch, J.; Thomsen, C.; Liu, J.; Czerw, R.; Terrones, M.; Adar, F.; John, C.; Whitley, A.; Carroll, D. L.; *Mater. Res. Soc.* **2003,** *772*, M7.8.1.

[195] Soin, N.; Roy, S.; Hazra, K. S.; Misra, D. S.; Lim, T. H.; Hetherington, C. J.; McLaughlin, J. A.; *J. Phys. Chem. C* **2011**, *115*, 5366

[196] Sidik, R. A.; Anderson, A. B.; *J. Phys. Chem. B* **2006**, *110*, 1787.

[197] Huang, S. ; Terakura, K.; *Phys. Rev. B* **2009**, 80, 235410.

[198] Zhao, L.; He, R.; Rim, K. T.; Schiros, T.; Kim, K. S.; Zhou, H.; Gutierrez, C.; Chockalingam, S. P.; Arguello, C. J.; Palova, L.; Nordlund, D.; Hybertsen, M. S.; Reichman, D. R.; Heinz, T. F.; Kim, H. P.; Pinczuk, A.; Flynn, G. W.; Pasupathy, A. N.; *Science* **2011**, *333*, 999.

[199] Aihara, J.; *J. Phys. Chem. A* **1999**, 103, 7487

[200] K. P. Gong, F. Du, Z. H. Xia,M. Durstock, L. M. Dai, *Science* **2009**, 323,760.

[201] S. S.Yu, Q. Zhang,L. M. Dai, *J. Am. Chem. Soc.* **2010**, 132, 15127.

[202] L. T. Qu, Y. Liu,J. B. Baek,L. M. Dai, *ACS Nano* **2010**, 4, 1321.

[203] Z. H. Sheng,L. Tao, J. J. Chen, W. J. Bao,F. B. Wang,X. H. Xia, *ACS Nano* **2011**, 5, 4350

[204] R. L. Liu,D. Q. Wu,X, K, Feng, K. Mullen, *Angew. Chem., Int. Ed.* **2010**, 49, 2565.

[205] Z. Sheng,H. Gao, W. Bao,F. Wang,X. Xia, X. *J. Mater. Chem.* **2012**, 22, 390.

[206] S. Wang,L. Zhang, Z. Xia,A. Roy, D. Chang,J. Baek, L. Dai, *Angew. Chem. Int. Ed.* **2012**, 51, 1.

[207] Z. Yang,Z. Yao, G. Li,G. Fang,H. Nie,Z. Liu,X. Zhou,X. Chen,S. Huang, *ACS Nano* **2012**, 6, 205.

[208] S. Yang, L. Zhi,K. Tang,X. Feng, J. Maier,K. Müllen, *Adv. Funct. Mater.* **2012**, 22, 3634.

[209] Y. Wu,S. Fang,Y. Jiang, Rudolf, R. Holze, *Journal of Power Source* **2002**, 108, 245.

[210] H. Gao, Z. Liu, L. Song, W. Guo, W. Gao, L. Ci, A. Rao, W, Quan,R. Vajtai,P. M. Ajayan, *Nanotechnology* **2012**, 23, 275605.

[211] J. K. Nϕrskov, J. Rossmeisl,A. Logadottir,L. Lindqvist, *J. Phys. Chem. B* **2004**, 108, 17886.

[212] W. Joseph Ochtershi, *Thermochemistry in Gaussian*, **2000**, Gaussian, Inc.

[213] A. Reyimjan, Sidik,B. A. Alfred, *J. Phys. Chem. B* **2006**, 110, 1787.

[214] Florian Banhart, Jani Kotakoski, and Arkady V. Krasheninnikov *ACS Nano*, **2011**, 5, 26-41.

[215] Pinshane Y. Huang, Carlos S. Ruiz-Vargas, Arend M. van der Zande, William S. Whitney, Mark P. Levendorf, Joshua W. Kevek, Shivank Garg, Jonathan S. Alden, Caleb J. Hustedt, Ye Zhu, Jiwoong Park, Paul L. Mc Euen, David A. Muller *Nature*, **2011**, 469, 389-393.

[216] Hashimoto, A.; Suenaga, K.; Gloter, A.; Urita, K.; Iijima, S. *Nature* **2004**, *430*, 870–873.

[1] Co ux, J. N'D y , A. T. Bu , C. M ly, T *Nano Lett.* **2008**, 8, 565–570.

[18] Cˇ v k , J. K l o , M. I. Fl p , C. F . J. *Nat. Phys.* **2009**, 5, 840–844.

[219] Lahiri, J.; Lin, Y.; Bozkurt, P.; Oleynik, I. I.; Batzill, M. *Nat. Nanotechnol.* **2010**, 5, 326–329.

[220] D. Gunlycke, C. T. White; Graphene Valley Filter Using a Line Defect; *PRL* **2011**, 106, 136806

[221] Xiangqing Lin and Jun Ni *Phys. Rev. B* **2011**, 84, 075461

[222] Zhang, L.; Xia, Z. *J. Phys. Chem. C* **2011**, *115*, 11170-11176.

[223] Zhang, L.; Niu, J.; Dai, L.; Xia, Z. *Langmuir* **2012**, *28*, 7542-7550.

[224] Shuangyin Wang, Dingshan Yu, Liming Dai, Dong Wook Chang, and Jong-Beom Baek, *ACS NANO* **2011**, 5, 6202-6209

[225] J. K. Nϕrskov, J. Rossmeisl,A. Logadottir,L. Lindqvist, *J. Phys. Chem. B* **2004**, 108 17886.

[226] Reyimjan, A.; Sidik; Alfred, B. A. *J. Phys. Chem. B* **2006**, *110*, 1787–1793.

[227] G. Gui , J. Li , J. X. Zhong , *Phys. Rev. B* **2008** , *78* , 075435 .

[228] M. Farjam , H. Rafi i-Tabar , *Phys. Rev. B* **2009** , *80* , 167401 .

[229] V. M. Pereira , A. H. C. Neto , N. M. R. Peres , *Phys. Rev. B* **2009** , *80* , 045401 .

[230] T. Low , F. Guinea , M. I. Katsnelson , *Phys. Rev. B* **2011** , *83* , 195436 .

[231] M. Mucha-K u zy k , I. L. Al , V. I. F l'ko , *Phys. Rev. B* **2011** , *84* , 041404 .

[232] L. Covaci , F. M. Peeters , *Phys. Rev. B* **2011** , *84* , 241401 .

[233] L. Sun , Q. X. Li , H. Ren , H. B. Su , Q. W. Shi , J. L. Yang , *J. Chem. Phys.* **2008** , 129 .

[234] Z. H. Ni , T. Yu , Y. H. Lu , Y. Y. Wang , Y. P. Feng , Z. X. Shen , *ACS Nano* **2008** , *2* , 2301 .

[235] T. Yu , Z. H. Ni , C. L. Du , Y. M. You , Y. Y. Wang , Z. X. Shen , *J. Phys. Chem. C* **2008** , *112* , 12602 .

[236] T. M. G. Mohiuddin , A. Lombardo , R. R. Nair , A. Bonetti ,G. Savini , R. Jalil , N. Bonini , D. M. Basko , C. Galiotis , N. Marzari , K. S. Novoselov , A. K. Geim , A. C. Ferrari , *Phys. Rev. B* **2009** , *79* , 205433 .

[237] Seon_Myeong Choim Seung-Hoon Jhi, and Young-Woo Son *Phys. Rev. B* **2010**, 81, 081407

[238] Jen-Hsien Wong, Bi-Ru Wu, and Ming-Fa Lin *J. Phys. Chem. C* **2012**, 116, 8271-8277.

[239] L. P. Zhang,Z. H.Xia, *J. Phys. Chem. C* **2011**, 115, 11170.

[240] L. P. Zhang,J. N. Niu,L. M. Dai, Z. H. Xia *Langmuir* **2012**, 28, 7542.

PUBLICATIONS

1. **Lipeng Zhang**, Zhenhai Xia; Mechanisms of Oxygen Reduction Reaction on Nitrogen-Doped Graphene for Fuel Cells; *J. Phy. Chem. C* 2011, 115 (22), 11170–11176

2. **Lipeng Zhang**, Jianbing Niu, Liming Dai; Effect of Microstructure of Nitrogen-Doped Graphene on Oxygen Reduction Activity in Fuel Cells; *Langmuir* 2012, 28, 7542-7550

3. Shuangyin Wang, **Lipeng Zhang**, Zhenhai Xia, Liming Dai; BCN Graphene as Efficient Metal-free Electrocatalyst for Oxygen Reduction Reaction; *Angew. Chem. Int. Ed.* 2012, 5, 1-5

4. **Lipeng Zhang**, Zhenhai Xia; Theoretical Study of Nitrogen Boron Co-doped Graphene as Efficient Oxygen Reduction Reaction Catalysts for Fuel Cells; ACS 245th National meeting: Division of Energy and Fuels; 2013 paper ID: 25063, final number: 458

5. In-Yup Jeon$^{=}$, Sheng Zhang$^{=}$, **Lipeng Zhang**$^{=}$, Hyun-Jung Choi, Zhenhai Xia, Liming Dai, Jong-Beom Baek; Edge-Selectively Sulfurized Graphene Nanoplatelets as Efficient Metal-Free Electrocatalysts for Oxygen Reduction Reaction: The Electron Spin Effect; *Advanced materials* 2013 (Accepted, manuscript ID: 201301436)

6. **Lipeng Zhang**, Mingtao Li, Jianbin Niu, Zhenhai Xia; Theoretical Study of sulfur-doped Graphene as Efficient Oxygen Reduction Reaction Catalysts for Fuel Cells; **2013**(revising)

7. **Lipeng Zhang**, Mingtao Li, Zhenhai Xia; Effect of Defect on Graphene to Catalytic Property of Oxygen Reduction Reaction in Fuel Cells; **2013** (revising)

8. **Lipeng Zhang**, Zhenhai Xia; Effect of Strain Field on Graphene and Doped graphene to Catalytic Property of Oxygen Reduction Reaction in Fuel Cells; **2013** (revising)

9. In-Yup Jeon, Hyun-Jung Choi, Jeong-Min Seo, Sun-Min Jung, Min-Jung Kim, Sheng Zhang, **Lipeng Zhang**, Zhenhia Xia, Liming Dai, Noejung Park, Jong-Beom Baek; Facile, Scalable Synthesis of Edge-halogenated Graphene

Nanoplatelets as Efficient Metal-free Electrocatalyst for Oxygen Reduction Reaction; Scientific Reports 2013, 1810

HONOURS AND AWARDS

Golden Key International Honour Society invited membership 2012

013 N o l T bl T C (NTTC) No O o R g o M ’ d v du l **3rd place**

2012 College Table Tennis Championships-Association College Union of International (ACUI) M ’ I d v du l **4th Place** Jun. 2012. Indiana University, Bloomington, Indiana

2012 Erie Table Tennis Championship Under Rating 2000 Team **1st Place** Erie, Pennsylvania

01 ACU I T bl T R g o M ’ I d v du l **1st Place**

2012 Table Tennis of University of Akron **1st Place**

2011 ACUI Region 7 Table Tennis- Team Match **2nd Place**, Dec. 2011

ACUI Region7 Table Tennis- M ’ g l , **3rd Place**, Feb. 2011 University of Michigan